DEFORMATION AND METASOMATISM OF THE QOMOLANGMA FORMATION: A GEOCHEMICAL AND MICROSTRUCTURAL ANALYSIS OF THE SUMMIT LIMESTONE, MOUNT EVEREST, NEPAL

By

Travis Leo Corthouts

A thesis submitted in partial fulfillment
of the requirements for the degree

of

Master of Science

in

Earth Sciences

MONTANA STATE UNIVERSITY
Bozeman, Montana

January 2015

©COPYRIGHT

By

Travis Leo Corthouts

2015

All Rights Reserved

~ In memory of Ankaji Sherpa ~

1978-2014



And to all other Sherpa climbers who sacrificed so much for our gain,
thank you!

ACKNOWLEDGEMENTS

I would like to extend my most sincere gratitude to my advisor Dr. David R. Lageson, whose passion for geology inspired me to switch my major to geology when I was a freshman at MSU. I thank him for his support prior to, during, and after the Everest Education Expedition (EEE), and for facilitating every stage of this project. Thank you to Dr. Colin Shaw for teaching me the ways of electron backscattered diffraction analysis, and to Dr. David Mogk for his help with the metamorphic and geochemical aspects of my research. I would also like to acknowledge the following for their help, including Darrell Henry at Louisiana State University, Michael Cosca at the USGS, Minnesota State University's Dept. of Earth Sciences, as well as Dr. Micah Jessup and his graduate student Cameron Hughes at the University of Tennessee.

Thanks to the EEE leader, Conrad Anker, for bringing MSU into the historic 2012 Everest expedition, and to Conrad's assistant Pamela Hainsworth, and Jiban Ghimire, our expedition coordinator in Nepal. Thank you to Suzie Taylor and Jamie Cornish for making me feel right at home when I joined the pre-expedition chaos. Special thanks to Sherpa climbers Danuru and Jangbu for their courageous efforts in collecting the suite of samples used in this study. Also, my deepest gratitude and respect goes out to all the Sherpa climbers and porters that supported our expedition.

This project would not have been possible without support from the MSU Dept. of Earth Sciences, MSU Alumni Foundation, MSU Extended University, Geological Society of America, and Mazamas Foundation. And thank you to The North Face, Black Diamond, Smart Wool, and Hyalite Equipment for supplying me with the gear I needed!

TABLE OF CONTENTS

1. INTRODUCTION. 1

2. GEOLOGIC SETTING... 5

Himalayan Orogeny Overview... 5
Evolution of the Himalaya... 8

3. LITHOLOGY AND STRUCTURES OF THE EVEREST REGION....10

Regional Overview 10
The Greater Himalayan Sequence... 12
Leucogranites of the Greater Himalayan Sequence....14
North Col Formation 20
Everest Series Schist... 21
Yellow Band... 22
South Tibetan Detachment System 23
Lhotse Detachment (Lhotse Shear Zone)... 25
Qomolangma Detachment 26

4. THE QOMOLANGMA FORMATION 30

Qomolangma Formation....30
Previous Characterizations....30
Age... 33
Depositional Setting 34

5. METHODS... 37

Sampling Strategy and Sample Processing... 37
Cathodoluminescence....39
Calcite Twin Morphology Analysis... 39
Electron Backscattered Diffraction Analysis (EBSD)... 40
Grain Size Measurements and Paleostress Calculations... 43
Electron Microprobe Analysis....45
Geochemical Analysis of Tourmaline... 46
Titanium-in-Biotite Geothermometry 48
Titanium-in-Quartz Geothermometry (TitaniQ)... 49
$^{40}Ar/^{39}Ar$ Geochronology... 50

6. RESULTS... 53

TABLE OF CONTENTS – CONTINUED

Stratigraphic Thickness Calculations... 53
Qomolangma Formation Samples 55
Summit Samples 55
Petrographic Observations... 56
EBSD Analysis 65
Paleostress Calculation... 70
Significance 71
Busher Rock Samples. 71
Petrographic Observations... 72
Hillary Step Samples 74
Petrographic Observations... 75
EBSD Analysis 80
Significance 82
South Summit Samples. 83
Petrographic Observations... 84
Primary Mineral Assemblage. 86
Secondary Mineral Assemblage 88
EBSD Analysis 92
Paleostress Calculations 95
Geochemical Analysis of Tourmaline 97
Metasomatism and the Significance Dravitic Tourmaline 99
Boron Sequestration and the Formation of Tourmaline 100
Origin: Detrital. 101
Origin: Intrinsic Boron Source 102
Origin: Extrinsic Boron Source 103
Titanium-in-Biotite Geothermometry 107
Titanium-in-Quartz Geothermometry (TitaniQ)... 110
$^{40}Ar/^{39}Ar$ Geochronology 112
Temporal Relationship Between
Metasomatism and Fabric Development 115
Significance... 119

7. ENVIRONMENT OF DEPOSITION 120

8. DISCUSSION. 124

Interpretation 124
Relationship Between Normal Faulting and Leucogranite Emplacement... 126

9. CONCLUSIONS 131

TABLE OF CONTENTS – CONTINUED

REFERENCES CITED.....133

APPENDICES. 156

APPENDIX A: Analytical Conditions and Instrumentation for Methods.....157
APPENDIX B: Electron Microprobe Data for Metasomatic Phases.....161
APPENDIX C: Electron Microprobe Data for Deformed Quartz Veins.....166

LIST OF TABLES

Table Page

1. Important sample information.....56

2. Electron microprobe data used for Ti-in-biotite geothermometry.....109

3. Electron microprobe data used for TitaniQ geothermometry…. 111

LIST OF FIGURES

Figure Page

1. Everest summit pyramid and sample locations....1
2. Sherpa climbers who collected samples for this study. 4
3. Generalized cross-section of the Central Himalaya.....7
4. Cross-section through the Everest region... 11
5. Map of the Everest region...15
6. Images of leucogranites in the Everest region 19
7. Qomolangma detachment on Everest and Changtse.....28
8. Paleogeographic map of the Early Ordovician 36
9. Chart of calcite twin morphologies....40
10. Diagram of pole figure LPO patterns….....43
11. General chemical formula for the tourmaline supergroup.....46
12. Backscattered image of a tourmaline grain….....47
13. Geologic map of the Everest summit area. 54
14. Photomicrographs of Summit samples… 58
15. Photomicrographs of Summit samples… 62
16. EBSD analysis orientation data for Summit samples.. 67
17. Photomicrographs of Busher Rock samples 73
18. Photomicrographs of Hillary Step samples....77
19. EBSD analysis orientation data for Hillary Step samples… 81
20. Photomicrographs of South Summit samples... 87

LIST OF FIGURES – CONTINUED

Figure Page

21. Photomicrographs of South Summit samples 89

22. Photomicrographs of South Summit samples 91

23. EBSD analysis orientation data for South Summit samples…. 93

24. EBSD analysis orientation data for South Summit samples..... 95

25. Tourmaline composition graph 99

26. Photo of leucogranites on Everest's southwest face 105

27. $^{40}Ar/^{39}Ar$ geochronology…. 114

28. Photomicrographs from South Summit sample... 118

29. Photomicrograph and photograph of a crinoid... 122

ABSTRACT

This study is based on a suite of new samples that represent a structural transect across the Qomolangma Formation, an Ordovician limestone that comprises the uppermost ~125 meters of Mount Everest. Past studies posit Everest's summit limestone to be mildly sheared and unmetamorphosed; however, this study shows that the Qomolangma Formation has endured more strain and metamorphism than previously thought. Ti-in-biotite and Ti-in-quartz geothermometry, electron backscattered diffraction analysis, and geochemical analysis of tourmaline has been used to infer the metamorphic and deformational history of this formation. Results show that the Qomolangma Formation has experienced significant ductile shear throughout, though samples preserve a stronger shear fabric toward the top of the formation. Furthermore, our data show a gradation in the degree of metamorphism across the Qomolangma Formation, increasing toward the base of the unit. Samples collected from the structural top of the formation (Summit samples) have a penetrative foliation with significant grain size reduction of calcite (~8 μm) and yield temperature estimates of $\geq 250^0$C. In contrast, samples from the base (South Summit samples) are distinguished by an increase in recrystallized grain size of calcite (~66 μm) and yield temperatures estimates of 500-600^{0}C. Another important difference between Summit and South Summit samples is aggregates of the coexisting minerals muscovite, chlorite, tourmaline, rutile and biotite found throughout South Summit samples. Geochemical analysis of tourmaline suggests these minerals crystallized from metasomatic fluids (hydrothermal fluids) released from leucogranite bodies emplaced into rocks structurally subjacent to the summit limestone. As a result, metasomatic fluids caused localized metamorphism at the base of the Qomolangma Formation, producing the significant increase in metamorphic grade observed in South Summit samples.

It is interpreted that the fabric preserved in Summit samples was ingrained during initial thrust faulting in the Eocene to Oligocene, whereas the fabric and metamorphic grade observed in South Summit samples is the result of detachment faulting and leucogranite emplacement in the Early Miocene. Lastly, microstructural observations suggest that metasomatic fluids may have promoted faulting on the Qomolangma detachment, a splay of the South Tibetan Detachment believed to be at the base of the Qomolangma Formation.

CHAPTER 1

INTRODUCTION

The Qomolangma Formation is an Ordovician carbonate rock that was deposited along the passive northern margin of India (Gondwana), and it now comprises the uppermost ~125 meters of Mount Everest (Figure 1). Everest has long been referred to by Tibetans as Qomolangma, and the rock formation which caps this natural pyramid preserves this name. Much has been studied and published about the structural, metamorphic and magmatic evolution of Mount Everest (Searle, 1999*a*; Searle et al.,

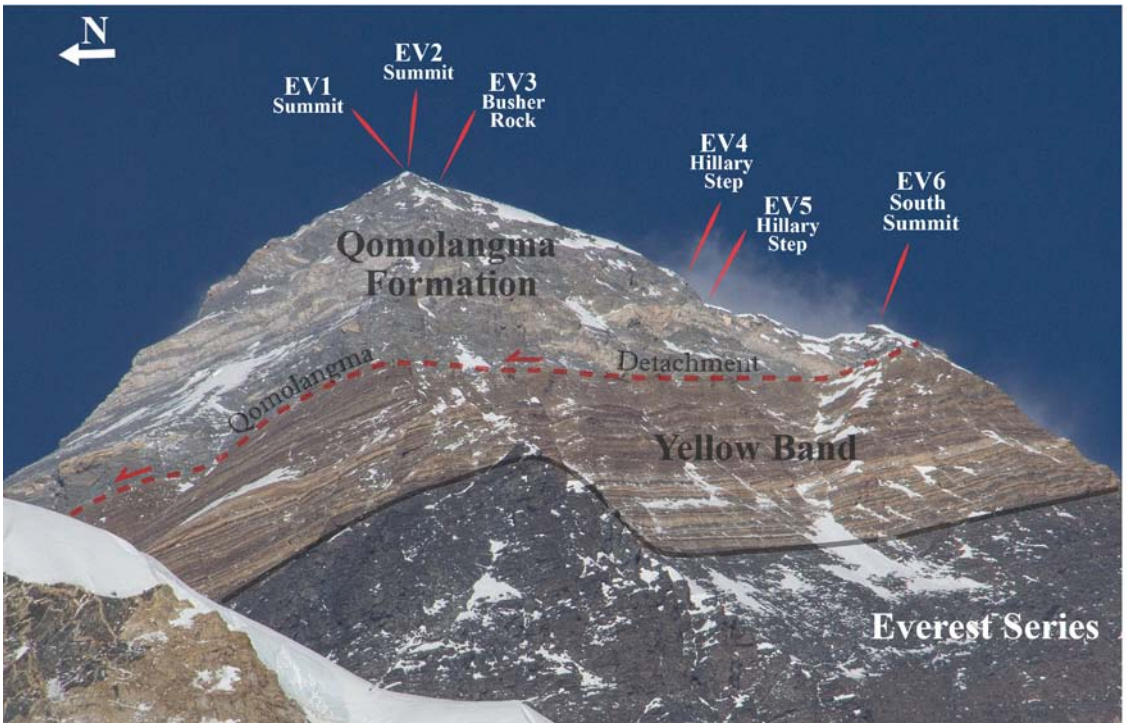


Figure 1. Southwest face of Mount Everest viewed from Pumori Camp 1, showing sample locations, the Qomolangma detachment, and the prominent lithologic units; together, the Yellow Band and Everest Series comprise the North Col Formation. Notice the white-weathering beds that occur throughout the Qomolangma Formation, these have been interpreted as thrombolites (Myrow et al., 2009).

2003; Law et al., 2004; Sakai et al., 2005; Jessup et al., 2006, 2008; Myrow et al., 2009; Cottle et al., 2011). These studies have revealed a complex geologic history involving contemporaneous thrusting and normal faulting (Burchfiel and Royden, 1985; Burchfiel et al., 1992; Hodges et al., 1992), polyphase metamorphism (Hodges et al., 1988; Pecher, 1989; Simpson et al., 2000; Viskupic et al., 2005; Jessup et al., 2008), injection of leucogranite sills and dikes (Wager, 1965; Pognante and Benna, 1993; Searle, 1999*b*; Weinberg and Searle, 1999; Carosi et al., 1999; Searle et al., 2003), and the exhumation of a ductile, mid-crustal channel (Hodges et al., 2001; Beaumont et al., 2001; Searle et al., 2003, 2006; Godin et al., 2006*a*; Jessup and Cottle, 2010). These investigations have provided a firm understanding of the geologic evolution for the High Himalaya in the Everest region, but they have not told the complete geologic story of the Qomolangma Formation.

Located on the border of Tibet and Nepal, the Qomolangma Formation is best exposed on the summit of Changtse and, immediately north of Changtse, in the Rongbuk Valley, Tibet. The extreme terrain and high altitude exposure of the Qomolangma Formation has hindered geologists from directly studying or sampling this formation (Searle 1999*a*), and most characterizations have been based on a few samples collected from Everest (e.g., Searle et al., 2003; Sakai et al., 2005; Jessup et al., 2006). However, in 2012 during an expedition led by Conrad Anker and sponsored by The North Face, National Geographic Society and Montana State University, a suite of samples were collected along the upper portion of the southeast ridge of Everest, including six locations across the Qomolangma Formation (Figure 1). Sampling of the southeast ridge was only possible with the dedicated help of trained Sherpa climbers Danuru Sherpa of Phortse and

Jangbu Sherpa of Makalu (Figure 2). These samples represent outcrops that heretofore have not been sampled or studied, and they are the first suite of samples that constitute a full structural transect of the Qomolangma Formation on the southeast ridge of Mount Everest. The aim of this investigation has been to gain a better geologic understanding of the Qomolangma Formation by addressing the following research questions:

(1) what is the lithology of the Qomolangma Formation?

(2) to what degree has the Qomolangma Formation undergone metamorphism and deformation?

(3) are there fabrics within the Qomolangma Formation that can be related to movement on the Qomolangma detachment?

(4) is there evidence that fluids promoted faulting on the Qomolangma detachment by increasing fluid pressure and weakening rocks near the fault zone?

Past publications characterize the Qomolangma Formation as a mildly sheared, unmetamorphosed limestone (Wager, 1934; Gysin and Lombardo, 1959, 1960; Gansser, 1964; Searle et al., 2003; Sakai et al., 2005; Jessup et al., 2006) that is separated from higher-grade rocks below by a brittle splay of the South Tibetan Detachment system (Figure 3), known as the Qomolangma detachment (Figure 1 and 4; Burg et al., 1983; Burchfiel et al., 1992; Searle, 1999*a*). However, this study shows that the Qomolangma Formation has a more complex geologic history and has sustained more deformation and metamorphism than previously thought.

Faults like the Qomolangma detachment are somewhat enigmatic due to the improbability of overcoming shear stress and friction along a fault plane. Hubbert and Rubey (1959) designed an investigation to test their hypothesis that the development of

low-angle thrust faults is due to pressurized fluid in the fault zone. Their hypothesis suggests that increased fluid pressure can reduce the normal stress in a rock body, thus reducing the shear stress needed to initiate shear rupture on a preexisting surface. This concept applies to low-angle normal faults like the Qomolangma detachment as well, in that gravity alone cannot provide enough force to initiate faulting. In this study, samples collected near the base of the Qomolangma Formation, ~25 meters above the Qomolangma detachment on Everest, have been analyzed to assess whether fluids promoted faulting on the Qomolangma detachment.



Figure 2. The Sherpa climbers who worked with Travis Corthouts and David Lageson to collect an extensive suite of samples from the southeast ridge of Everest in spring 2012. Danuru Sherpa of Phortse (left) and Jangbu Sherpa of Makalu (right).

CHAPTER 2

GEOLOGIC SETTING

Himalayan Orogeny Overview

Since the initial collision of India and Asia at *c*. 54-50 Ma (Molnar, 1988; Searle et al., 1987; Rowley, 1996, 1998) the Himalaya have been under continuous north-south compression, resulting in ~1,800 km of total shortening in the western portion of the orogen to ~2,750 km in the east (Dewey et al., 1989). The suture between India and Asia is known as the Indus Tsangpo suture (also called the Indus Yarlung suture), and it marks the limit of Indian crust south of the suture and Tibetan crust largely composed of pre-collision accreted terranes to the north (Gansser, 1964, 1977; Le Fort, 1975; Searle, 1986; Searle et al., 1987). South of the Indus Tsangpo suture, the Himalayan orogenic belt can be split into four major lithotectonic units (Figure 3; Gansser, 1964; Le Fort, 1975) which, from north to south are: (1) the Tethyan Himalayan Sequence comprised of pre-collision marine sedimentary rocks of the northern Indian continental shelf, which are largely unmetamorphosed and are locally interlayered with volcanic flows (Garzanti, 1999; DiPietro and Pogue, 2004; Yin, 2006); (2) the Greater Himalayan Sequence comprised of a mid-crustal layer that was metamorphosed at amphibolite to granulite facies conditions from the Oligocene to the Middle Miocene, with migmatites and anatectic leucogranites prevalent at upper structural levels (Searle et al., 2006); (3) the Lesser Himalayan Sequence composed of unmetamorphosed to low-grade metasedimentary and metavolcanic strata (Le Fort, 1975; Yin, 2006); (4) and the Sub-

Himalayan Sequence composed of unmetamorphosed Neogene molasse and, to the west, Permian Gondwana beds and Mesozoic Tethyan rocks (DiPietro and Pogue, 2004).

Dividing these tectonic packages are major faults that have played a significant role in the tectonic and geomorphic evolution of the Himalaya. Separating the Tethyan Himalaya from the Greater Himalaya is the South Tibetan Detachment system (STDS or STD depending on reference frame), a network of north-dipping normal faults and shear zones that extends for over 2,000 km along the topographic crest of the orogen (Burchfiel et al., 1992). This structure has played a major role in the orogenic collapse and tectonic unroofing of the Himalaya (Hodges et al, 1998), resulting in the exhumation of the Greater Himalayan Sequence throughout the Miocene (Burchfiel and Royden, 1985; Hodges et al., 1992). Separating rocks of the Greater Himalaya from those of the Lesser Himalaya is the south-directed Main Central Thrust (MCT; Figures 3 and 4; Gansser, 1964; Hubbard, 1989; Hodges et al., 1992, 1993; Searle et al., 2008), which is characterized by a 3-5 km thick high-strain ductile shear zone with inverted metamorphic isograds from biotite to sillimanite grade (Figure 4; Hubbard, 1996; Harrison et al., 1999*b*; Stephenson et al., 2000, 2001; Searle et al., 2008), a phenomenon that has received considerable study. In the Central Himalaya between *c*. 21 Ma and *c*. 14 Ma (Hubbard and Harrison, 1989; Johnson and Rodgers, 1997; Arita et al., 1997; Johnson et al., 2001; Catlos et al., 2002), the MCT effectively transported Greater Himalayan metamorphic rocks ~200 km southward (Schelling and Arita, 1991; Searle et al., 2002, 2003), placing them over relatively unmetamorphosed rocks of the Lesser Himalaya, as first recognized and described by Heim and Gansser (1939) and Gansser (1964). An important aspect of the MCT is that it is marked by a break in metamorphic grade, rather

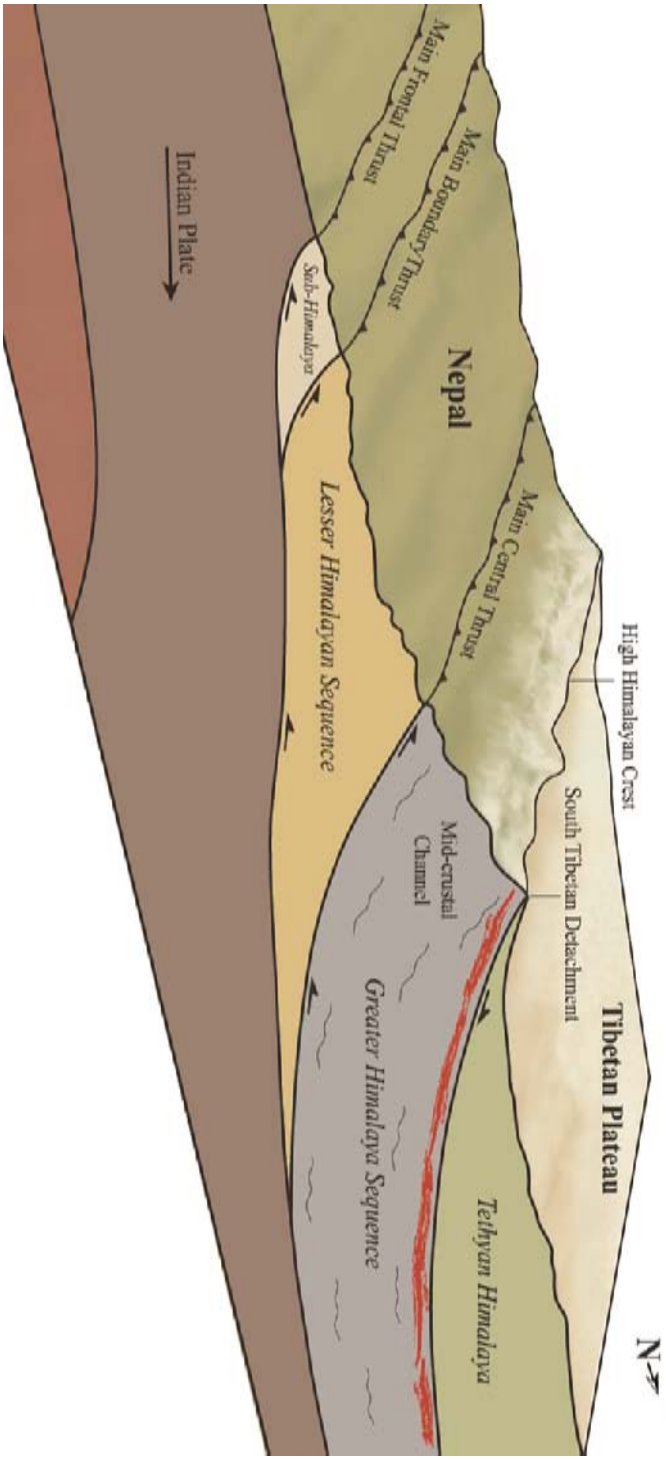


Figure 3. Schematic north-south cross-section through the Central Himalaya showing the major lithotectonic units and their bounding structures. The red package of rock at the very top of the Greater Himalayan Sequence is crustal melt leucogranites. Modified from Owen, (2010).

than age or strain. This has caused much confusion because the high-strain zone, which is considered by some to be the true location of the MCT (e.g., Searle et al., 2008), does not always occur at the base of the Greater Himalaya, which is where this structure has been placed. As such, some geologists have mapped the contact between the Greater and Lesser Himalayan Sequence as an unconformity (e.g., Gascombe et al., 2006), placing the MCT at the base of the high-strain zone, which for example in the eastern Himalaya and Bhutan, occurs at a much higher structural level within the Greater Himalaya. Furthermore, coeval thrusting and normal faulting on the MCT and STDS, respectively, is believed by many geologists to have been the primary cause for exhumation of the Greater Himalayan Sequence throughout the Miocene (Law et al., 2006 and papers therein). The INDEPTH seismic reflection profiling project across southern Tibet has matched these major structures to prominent reflectors, confirming that these faults continue down-dip under southern Tibet (Zhao and Nelson, 1993; Nelson et al., 1996). At *c*. 11 Ma, thrusting in the Himalaya propagated southwards to the Main Boundary Thrust (Meigs et al., 1995), which has carried rocks of the Lesser Himalaya over those of the Sub-Himalaya. Subsequently, the Main Frontal Thrust has recently been activated along the base of the Sub-Himalayan Sequence, marking the southern limit of thrusting in the Himalayan orogen (DiPietro and Pogue, 2004; Yin, 2006).

Evolution of the Himalaya

Following collision, India was thrust under Asia and in essence, the Indian upper-crust was peeled back and thrust southward over India, resulting in considerable crustal thickening of the Tethyan Sequence by *c*. 30 Ma (Vannay and Hodges, 1996; Seale et al.,

2007). Thickening of Tethyan sedimentary rocks led to burial and Barrovian series metamorphism of the Indian middle-crust during the Late Eocene and Early Oligocene (Vannay and Hodges, 1996; Coleman and Hodges, 1998; Godin et al., 2001), which consequently produced the high-grade metamorphic core of the Himalaya known as the Greater Himalayan Sequence. By the Late Oligocene (*c*. 25 Ma), thrusting had propagated forelandward to the MCT, which carried high-grade rocks of the Greater Himalayan Sequence southward over relatively unmetamorphosed rocks of the Lesser Himalayan Sequence (Gansser, 1964; Hubbard and Harrison, 1989). At the same time throughout the Early and Middle Miocene, the STDS episodically reactivated along preexisting thrust faults which had originally thickened the Tethyan Sequence immediately following collision. Normal faulting on the STDS, coupled with erosion, has effectively "un-roofed" the Greater Himalayan Sequence, exposing it along the axis of highest topography throughout the orogen (e.g., Law et al., 2006).

CHAPTER 3

LITHOLOGY AND STRUCTURES OF THE EVEREST REGION

Regional Overview

In the Everest region the Greater Himalayan Sequence is a 15-20 km thick, north-dipping lithotectonic unit (Figure 4; Searle et al., 2006) that is bounded at its top by the lower of two strands of the STD, known as the Lhotse detachment (Figure 4). The Lhotse detachment was first described by Searle (1999*a*) and it is a low-angle normal fault that separates Greater Himalayan rocks in the footwall from those of the North Col Formation in the hanging wall above (Figure 4; Searle et al., 2003; Jessup et al., 2008). Well-exposed on the southwest face of Mount Everest, the North Col Formation constitutes the bulk of the Everest pyramid, extending from just above the Western Cwm to within ~200 meters of the summit of Everest (Figures 1 and 4). The North Col Formation is a thick package of pelitic schist and calc-silicate metasedimentary rocks (Lombardo et al., 1993; Carosi et al., 1999; Jessup et al., 2008) which grades from amphibolite facies immediately above the Lhotse detachment, to greenschist facies at the structural top of the formation (Jessup et al., 2008). Overlying the North Col Formation, and comprising the uppermost ~125 meters of Mount Everest, is the Qomolangma Formation (also referred to as the 'summit limestone'), a package of gray-green marine limestone belonging to the Tethyan Himalayan Sequence (Gansser, 1964, p. 158-164). Marking the contact between these formations is the Qomolangma detachment (Sakai,

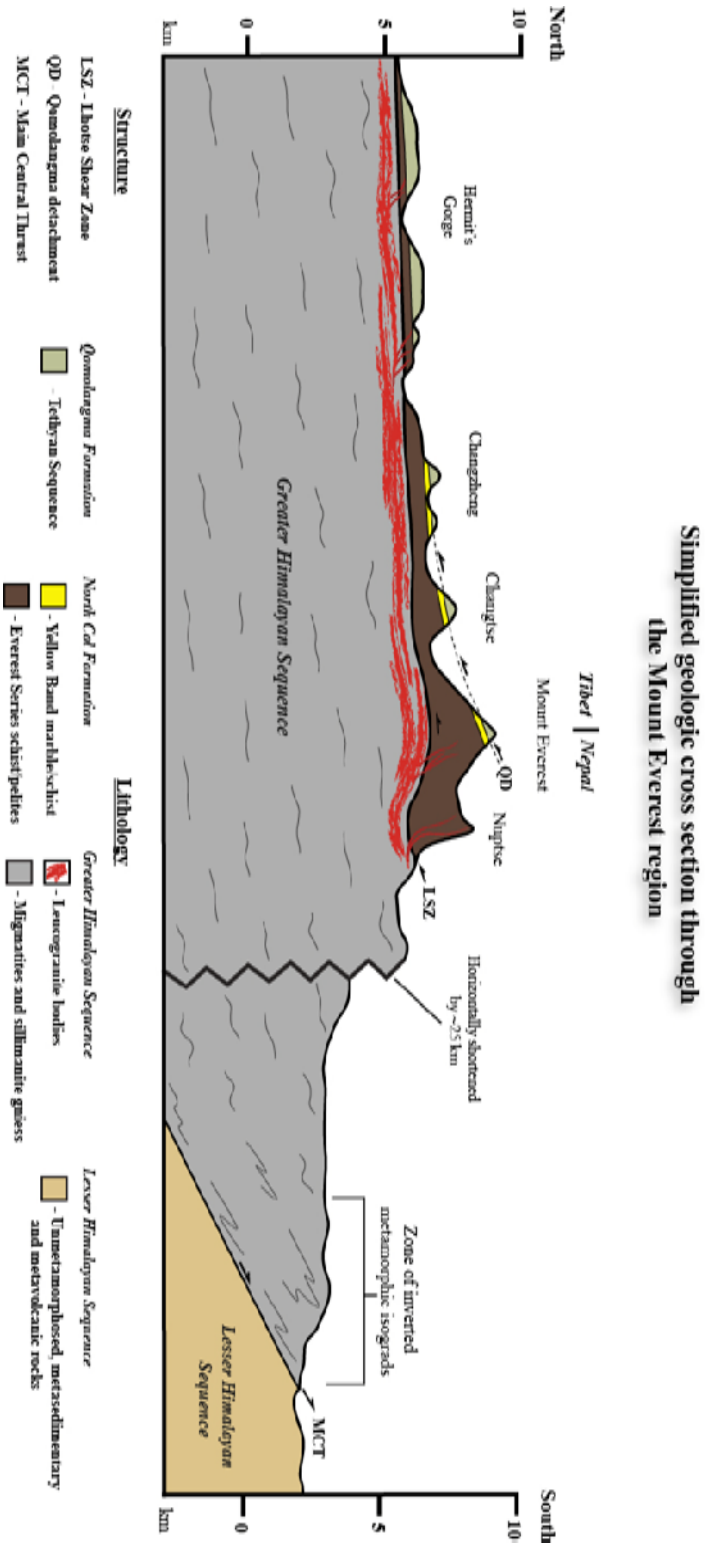


Figure 4. North-south cross-section through the Everest region, shortened horizontally by ~25 km. Modified from Jessup et al. (2006, 2008); Searle et al. (2003, 2006).

1997; Searle, 1999*a*; Searle et al., 2003; Sakai et al., 2005), a structurally higher strand of the STD that exists at the base of the summit limestone and gently dips north-northeast into Tibet where it is well-exposed at lower elevations in the Rongbuk Valley (Figure 5; Burchfiel et al., 1992; Hodges et al., 1992; Murphy and Harrison, 1999; Searle, 1999*a*).

The Greater Himalayan Sequence

The crystalline core of the Himalaya has many names (e.g., High Himalayan Crystallines, Greater Himalayan series, or Greater Himalayan slab), in this paper it is referred to as the Greater Himalayan Sequence or simply the Greater Himalaya. Well-exposed in the Everest area, this lithotectonic unit is both overlain and underlain by low-grade metasedimentary rocks of the Tethyan Himalayan Sequence and Lesser Himalayan Sequence, respectively (Hodges, 2000; Yin, 2006), and is composed of sillimanite gneiss, migmatites and extensive leucogranite bodies at upper structural levels (Figures 4; Searle et al., 2006). The Greater Himalayan Sequence is exposed for some ~45 km south of Everest, from the footwall of the STD at the base of the Everest pyramid, to Karikhola south of Lukla, Nepal (Figure 4; Searle et al., 2006). Many geologists have purported that the bounding fault zones of the Greater Himalayan Sequence were active simultaneously between *c*. 22-16 Ma (Burchfiel and Royden, 1985; Burchfiel et al., 1992; Hubbard and Harrison, 1989; Hodges et al., 1992, 1993); however, this is questionable because timing of initiation for the STDS is poorly constrained (Murphy and Harrison, 1999; Searle and Godin, 2003). Regardless of whether these structures had coeval activity, the basal MCT has indeed transported Greater Himalayan rocks southward while episodic detachment faulting, coupled with elevated erosion along the range front, has

resulted in the exhumation of this mid-crustal slab throughout the highest parts of the orogen. The Greater Himalayan Sequence was derived from Indian middle-crust that originated ≤1000 km south of the initial position of the Indus Tsangpo Suture zone (Jamieson et al., 2006), and the protolith for the sillimanite gneiss that comprises much of the Greater Himalayan rocks in the Everest area (Barun gneiss) is thought to be Proterozoic black shale (Searle et al., 2006). The Greater Himalayan Sequence is commonly modeled as a ductile slab that has been extruded southward (Figure 3), driven by gradients in lithostatic pressure beneath the Tibetan Plateau and focused denudation along the range front (Nelson et al., 1996; Grujic et al., 1996, 2002; Hodges et al., 2001; Beaumont et al., 2001, 2004; Godin et al., 2006*a*; Searle et al., 2006). Southward extrusion of the Greater Himalayan Sequence channel initiated in the Early Miocene and since then it has had a significant influence on the geomorphic evolution of the High Himalaya (Hodges et al., 2001; Law et al., 2006 and papers therein).

In the Everest region, the thermal evolution of the Greater Himalayan Sequence is defined by a clockwise P-T path composed of two phases of metamorphism (Hodges et al., 1988; Pecher, 1989), although some geologists have interpreted three phases (e.g., Pognante and Benna, 1993). Peak metamorphic conditions for the earlier, Eohimalayan event is bracketed between 38.9 ± 0.9 Ma (Cottle et al., 2009) and 32.2 ± 0.4 Ma (Simpson et al., 2000) and correlates with prograde, Barrovian metamorphism associated with crustal thickening. The Eohimalayan event is largely overprinted by Neohimalayan metamorphism throughout the core of the Greater Himalayan Sequence and it is best preserved along the upper structural levels and in superjacent rock formations, where P-T estimates of 550-680°C and 8-10 kbar have been reported (Pognante and Benna, 1993;

Viskupic et al., 2005; Jessup et al., 2008; Cottle et al., 2009). In contrast, Neohimalayan metamorphism is distinguished as a high temperature, low pressure event that records temperatures of 650-750°C and isothermal decompression from ~7 to 3 kbar (Hubbard, 1989; Searle et al., 2003; Viskupic et al., 2005; Jessup et al., 2008), occurring from 26.3 Ma to *c*. 20 Ma (Simpson et al., 2000; Viskupic et al., 2005). The decompression path of Neohimalayan metamorphism is interpreted by Jessup et al. (2008) as evidence of extrusion and exhumation of the Greater Himalayan Sequence at high temperatures and moderate to low pressures. During the Neohimalayan event, widespread crustal melting within the Greater Himalayan Sequence resulted in the generation and crystallization of leucogranites in the Early Miocene (e.g., Schärer et al., 1986; Harrison et al., 1999*b*; Viskupic et al., 2005).

Leucogranites of the Greater Himalayan Sequence

In the Everest region, the upper portion of the Greater Himalayan slab is heavily injected with crustal melt leucogranite comprised of early sills and later crosscutting dikes (Figure 6; Gansser, 1964; Searle, 1999*a*; Weinberg and Searle, 1999). The initial melting of protolith rocks is associated with Neohimalayan metamorphism and is thought to have taken place within the middle-crust of the underthrusted Indian plate. Early anatexis was followed by upward channeling and foliation-parallel migration of melts into the upper levels of the Greater Himalayan Sequence (Searle et al., 2009). Leucogranites concentrated at the top of the Greater Himalayan Sequence have laterally coalesced to form massive sheeted sill complexes, which in turn form some of the most spectacular, high peaks in the Himalaya (e.g., Makalu, Manaslu, Shivling and Shisha

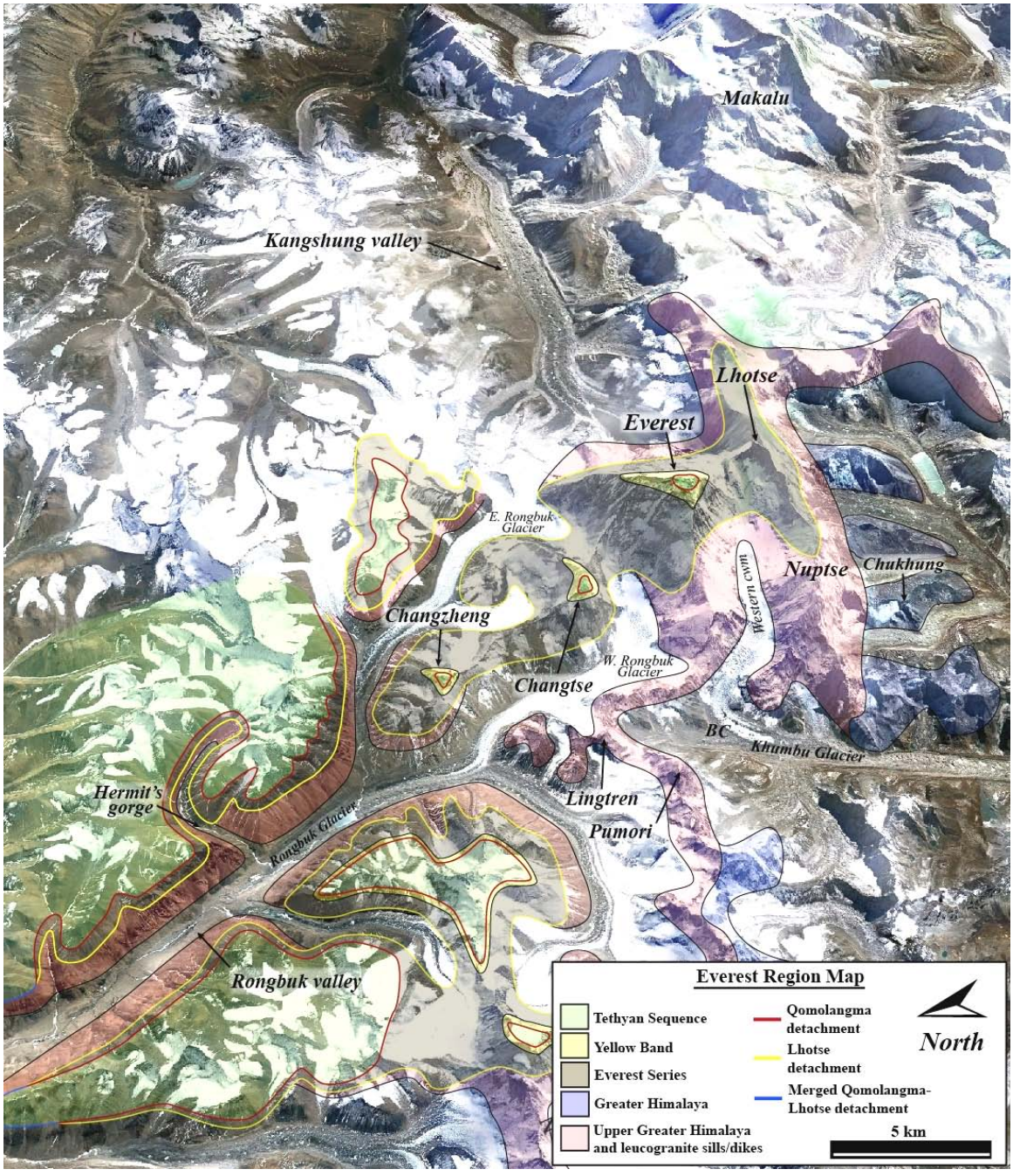


Figure 5. Simplified geologic map of the Everest area; peaks and locations referenced in the text are labeled; (BC) = Base Camp. Base layer is a Google earth image.

Pangma). Throughout the orogen, leucogranite is ubiquitous along the upper levels of the Greater Himalayan Sequence, and the Everest area contains perhaps the greatest proportion of leucogranites anywhere in the Himalaya (Searle et al., 2003). Spectacularly exposed on the south face of Nuptse, Everest's Kangshung face, and on the north faces of Chomolonzo and Makalu, are massive ballooning sills of leucogranite up to ~3000 meters thick. Extensive field mapping has shown that these leucogranite bodies all lie at the same structural horizon near the top of the Greater Himalayan slab, extending from Cho Oyu and the Shisha Pangma massif in the west to Makalu in the east (Figure 5; Searle, 1999*a*, *b*; Searle et al., 2003). Geochronologic evidence shows that anatexis and granite emplacement has been episodic (Viskupic et al., 2005) and crystallization ages throughout the orogen span a wide range between *c*. 24-12 Ma (Schärer et al., 1986; Harrison et al., 1999*b*; Viskupic et al., 2005; Searle et al., 2009), although younger leucogranite bodies have been dated in the Nanga Parbat syntaxis at 1.6-0.71 Ma (Crowley et al., 2005, 2009) and in the Namche Barwa syntaxis at < 4 Ma (Burg et al., 1998).

In the Everest region, U-Pb thermal ionization mass spectroscopy dating of monazite, xenotime and zircon has shown that initial, in-situ partial melting took place 25 km south of Everest in the Namche orthogneiss between *c*. 26-23 Ma (Viskupic et al., 2005), prior to melt migration. Evidence for early melt migration comes from a sample collected from the Nuptse granite, one of the largest leucogranite bodies in the Khumbu region, estimated at 4 km wide and 2 km thick (Figure 6c; Lombardo et al., 1993; Searle, 1999*b*; Searle et al., 2003). The sample was collected at the summit of Chukhung (Figure 5) < 2 km south of Nuptse and dated at 23.6 ± 0.7 Ma (Jessup et al., 2008) using U(-Th)-

Pb isotope analysis of monazite by laser ablation multi-collector-inductively coupled plasma ionization mass spectrometry (LA-MC-ICPMS); this age is interpreted as the final crystallization age of the Nuptse granite. Using U-Pb mass spectrometry isotope dating of monazite and xenotime, Simpson et al. (2000) dated a leucogranite sample from Kala Pattar at 22.7 ± 0.2 Ma, and a sample collected near the base of Khumbutse that dates the final emplacement and crystallization of the Everest granite at 20.5-21.3 Ma. Timing of early melt migration in the Everest region is further constrained by U-Pb geochronology of syn-kinematic sills which crystallized at 21.8 ± 0.05 and 21.33 ± 0.03 Ma (Viskupic et al., 2005). Ages for younger, post-kinematic leucogranite emplacement in the Everest area consists of a crosscutting dike on Lingtren which yielded an average age of 16.5 Ma, and a similar dike from the south face of Nuptse that crystallized at 20.2 ± 1.0 Ma, using U(-Th)-Pb isotope geochronology of monazite (Searle et al., 2003). Near Gokyo Ri, ~20 km west of Everest, crystallization of post-deformational leucogranite dikes occurred between 17.6 Ma and 18.3 Ma (Viskupic et al., 2005). Immediately to the north of Everest in the Rongbuk Valley (Figure 5), leucogranite is well exposed in cliffs near Rongbuk monastery, where it accounts for up to 50% of rock in the footwall of the STD (Wager, 1965). Here, Murphy and Harrison (1999) used Th-Pb ion-microprobe geochronology of monazites to date a dike that crosscuts metamorphic fabric in footwall rocks at 16.8 ± 0.8 Ma, a dike which has been deflected into parallelism with detachment shear zone foliation at 16.4 ± 0.6 Ma, and a mylonitic sill immediately beneath the detachment dated at 16.2 ± 0.8 Ma. In the Makalu region, just east of Everest (Figure 5), early anatexis and leucogranite crystallization occurred between *c*. 24-21 Ma (Schärer, 1984; Streule et al., 2010), while decompression related melting occurred at 16.0 ± 0.6

Ma and 15.6 ± 0.2 Ma, based on U(-Th)-Pb LA-MC-ICPMS dating of monazites from cordierite-bearing leucogranite and the migmatitic Barun gneiss, respectively (Streule et al., 2010).

The age of leucogranites from the Everest area shows that anatexis occurred in two phases, represented by (P1) foliation-parallel sills that crystallized between *c*. 23-20 Ma and (P2) crosscutting dikes that crystallized between *c*. 16-17 Ma. Because of the pressure-drop during Neohimalayan metamorphism, crustal anatexis has been temporally related to decompression and exhumation associated with movement on the STDS (e.g., Harris and Massey, 1994). But, the earliest known melting in the Everest region took place at least 3 Ma prior to the oldest dated phase of movement on the STD, and only the youngest P2 dikes temporally overlap with slip on the detachment system. This suggests that early anatexis was driven by some other cause such as radiogenic heating or crustal thickening, and only the more recent anatectic leucogranites (i.e., P2 leucogranites) may be related to decompression triggered by slip on faults of the STDS. Searle et al. (2009) advocates that melting was provoked by a combination of thermal relaxation due to crustal thickening and from high rates of internal heat production in the protolith rocks.

In the Everest area leucogranites are peraluminous and two main types have been identified: (1) two-mica leucogranite containing muscovite + biotite ± tourmaline ± cordierite ± andalusite ± sillimanite; and (2) tourmaline leucogranite containing muscovite + tourmaline ± biotite ± andalusite ± sillimanite ± garnet ± kyanite ± spinel ± corundum (Le Fort et al., 1987; Guillot and Le Fort, 1995; Searle et al., 1997; Harrison et al., 1999*a*: Visonà and Lombardo, 2002; Visonà et al., 2012). Both of these are believed to have formed by in-situ partial melting of muscovite-rich pelitic rocks at andalusite-

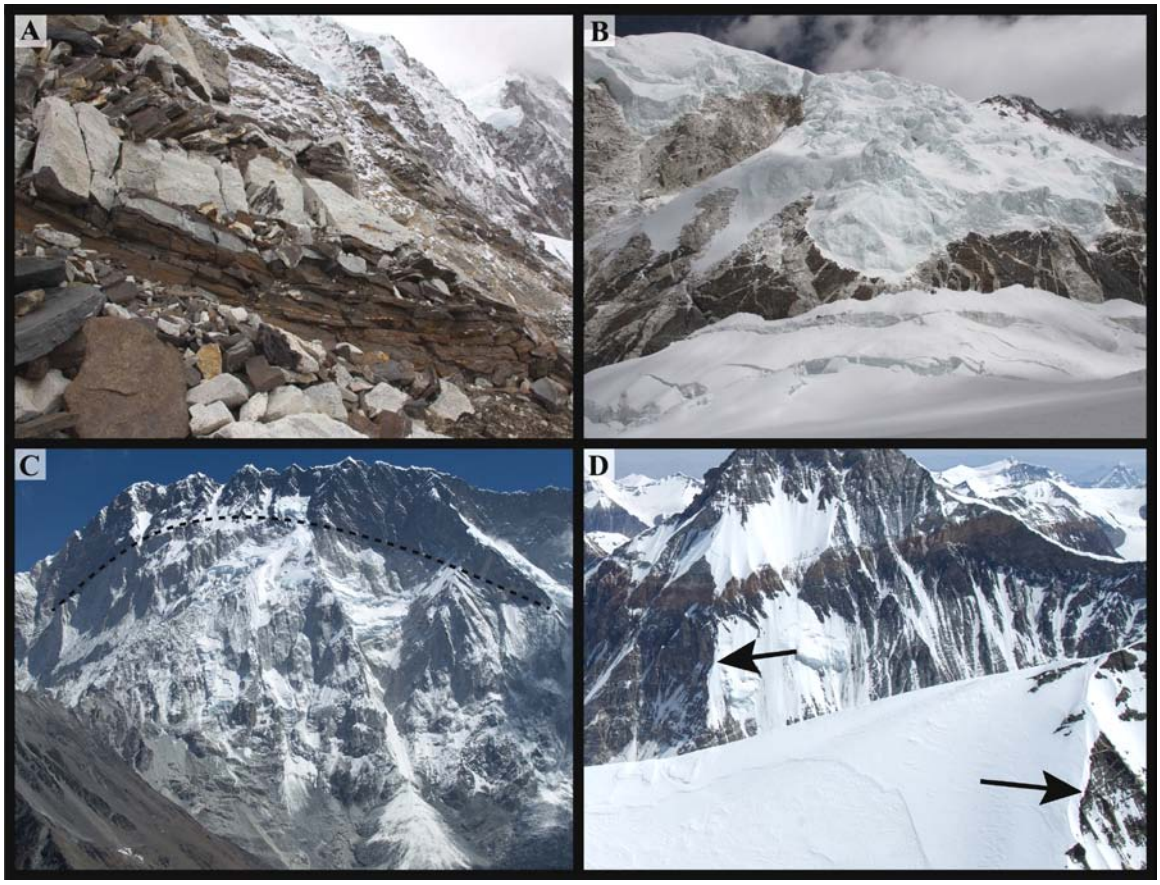


Figure 6. Leucogranites in the Everest area. A) Sills injected into schist; photo taken between Pumori camp 1 and 2. B) Dikes radiating up to the west ridge of Everest; photo taken in the Western Cwm (Figure 5) between camps 1 and 2. C) The Nuptse pluton seen on Nuptse's south face. D) The Qomolangma Formation and Yellow Band exposed on Changtse, immediately north of Everest. Lower right arrow points to leucogranite dikes on Everest's west ridge at ~7,600 meters; left arrow points to dike swarms on Changtse which nearly reach the Yellow Band. Photo: Max Lowe.

sillimanite grade and low- to moderate-pressure (4-6 kbar; Searle et al., 2009). Crosscutting relationships show that the two-mica leucogranites intruded first followed by the tourmaline leucogranites (Burchfiel et al., 1992; Searle et al., 1997; Weinberg and Searle, 1999). For example, the Makalu and Nuptse granite are composed of two-mica granite intruded by tourmaline granite (Visonà and Lombardo, 2002). In addition, Streule et al. (2010) reported even later dikes within the Makalu granite with large

cordierite crystals which they interpret to be related to decompression and exhumation of the Greater Himalayan Sequence. Visonà and Lombardo (2002) suggest that tourmaline leucogranites were produced by muscovite dehydration melting in muscovite-rich metapelites, while two-mica leucogranites were produced by biotite dehydration melting in biotite-rich metapelites. Guillot and Le Fort (1995) advocate that two-mica leucogranites have a metagreywacke source and formed under water-saturated conditions while tourmaline leucogranites formed from water-absent melting of a metapelitic source. For both lithologies, isotope geochemistry of Sr, Nd and Pb suggests a metasedimentary crustal protolith (Daniel et al., 1987; Harris et al., 1995) corresponding to metasediments of the Greater Himalayan Sequence. Guo and Wilson (2012) used whole-rock major and trace element data, combined with Sr-Nd isotope data, to show that the melt source was a two-component mixture derived of fluid from the Lesser Himalayan Sequence and the Greater Himalayan Sequence. More to the point, these studies show that leucogranite within an individual intrusive complex may comprise a mixed assemblage in terms of composition and timing of melt influx, suggesting polyphase intrusion from varying crustal sources dominantly within the Greater Himalayan Sequence.

North Col Formation

The North Col Formation is a thick package of dark, thin-bedded rocks that lie directly below the Qomolangma Formation (Figure 4). The North Col Formation was named by Lombardo et al. (1993) and Carosi et al. (1998, 1999), and it has also been referred to as the Everest Series by Wager (1934, 1965), Searle et al. (2003) and Jessup et al. (2006, 2008), which is a nonstratigraphic term that is defined on metamorphic and

structural criteria (Myrow et al., 2009). In this paper the Everest Series refers to the dark pelitic schists below the prominent Yellow Band (Figure 1) and together, the Everest Series and Yellow Band comprise the North Col Formation.

Everest Series Schist

The Everest Series is well-exposed on the southwest face of Everest as a thick succession of dark colored, thin-bedded pelitic rocks (Figure 7). Some of the first detailed descriptions of the Everest Series came from Gysin and Lombardo (1959, 1960) who described samples collected from Lhotse and the South Col by members of the Swiss expedition of 1956. From these samples, they described the Everest Series as "calc-schist, sandy calc-schist, and fine sandy, sericitic-quartzitic to feldspathic calcareous pelites." More recent samples collected at the South Col (7,986 meters) contained the assemblage: albite + quartz + biotite + chlorite + epidote ± muscovite, which Searle et al. (2003) interpreted as evidence for middle to upper greenschist facies metamorphic conditions. A comprehensive investigation on the metamorphic history of the Everest Series schist was conducted by Jessup et al. (2008) who used U(-Th)-Pb geochronology, geothermobarometry and micro-macro structural analysis. These authors showed that metamorphic grade in the Everest Series is higher than originally thought and is gradational as well, from amphibolite facies at the base of the unit to upper greenschist facies at the Yellow Band. Many samples of the Everest Series record Eohimalayan metamorphism under conditions estimated at ~649 ± 21ºC, 6.2 ± 0.7 kbar, while other samples record isothermal decompression during Neohimalayan metamorphism at temperatures and pressures of 607 ± 25ºC, 2.9 ± 0.6 kbar (Jessup et al.,

2008). The decompression path recorded in these more rare samples is characteristic of Greater Himalayan Sequence rocks located structurally below the Lhotse detachment, which are dominated by high-temperature, low-pressure conditions typical of Neohimalayan metamorphism.

Yellow Band

The Yellow Band comprises the uppermost part of the North Col Formation and is immediately subjacent to the Qomolangma Formation (Figures 1, 4 and 7). The Yellow Band is easily distinguished from the dark-colored rocks of the North Col Formation as a prominent, ~172 meter thick (Sakai et al., 2005), yellow-gold weathering package of rock that encircles the summit pyramid like a gold ring. The Yellow Band crops out between 8,275 - 8,530 meters on the northeast ridge and between 8,595 - 8,725 meters on the southeast ridge (this study). The first recorded description of the Yellow Band came from Lawrence Wager who collected a sample from the Yellow Band at ~8,290 meters along the northeast ridge directly above camp VI, and described the sample as a "typical yellow schistose marble forming the Yellow Band" (Lawrence Wager Collection records, Oxford University Museum; see also Wager, 1934 and 1939). The Yellow Band was also described by Gansser (1964) who reported that "The yellow band consists of schistose limestones and is covered by the greyish, arenaceous, schistose, and more or less dolomitic limestones." Subsequent characterizations of the Yellow Band have been given by Searle et al. (2003), Sakai et al. (2005) and Jessup et al. (2006). They describe this unit as coarse-grained marble, phyllite and schist composed of calcite, quartz, muscovite, dolomite ± biotite and is a similar metamorphic grade to the

underlying upper greenschist facies pelites and psammites of the Everest Series (Searle et al., 2003). Using aerial photographs, Sakai et al. (2005) identified large-scale cross-stratification within the Yellow Band, although they also claimed that parallel bedding is a prominent feature. Sakai et al. (2005) used fission-track dating of zircon and apatite to constrain the timing of cooling of the Yellow Band. Their results show an average age for zircons and apatites of 14.4 ± 0.9 Ma and 14.4 ± 1.4 Ma respectively, indicating that the Yellow Band cooled rapidly through the zircon partial annealing zone (230-330ºC) down to the apatite fission-track closure temperature (130 ± 30ºC) at *c*. 14.4 Ma.

The Yellow Band was originally considered to be Permian by Wager (1934), then Ordovician by Wang and Zhen (1975) and Burchfiel et al. (1992), based on correlations with lithologically similar rocks north of Everest and in the Annapurna region to the east. More recently, stratigraphic correlation with the Karsha Formation in Nyalam, 75 km west of Everest, demonstrates the Yellow Band to be Middle Cambrian and was deposited in a continuous Cambrian depositional system along the passive northern margin of East Gondwana (Myrow et al., 2009).

South Tibetan Detachment System

Early studies in southern Tibet identified a low-angle, north-directed fault that places unmetamorphosed Paleozoic rocks over high-grade gneisses and leucogranites of the Greater Himalayan Sequence (Caby et al., 1983; Burg et al., 1983; Burchfiel et al., 1992). This structure is known as the South Tibetan Detachment system (also called the South Tibetan Fault System), and it is an orogen-scale network of normal faults that traverses the crest of the orogen along strike for over ~2000 km (Figure 3; Burchfiel et

al., 1992). Outwardly, faulting on the STDS appears similar to low-angle detachment normal faults in the Basin and Range province of the western United States. However, in the Himalaya, these faults are restricted to upper crustal levels while coeval shortening is accommodated at lower structural levels by thrusting, whereas in the North American Cordillera the lithosphere is extending at all levels. The timing of initiation of the STDS is not well constrained, nor is it well known when motion on the detachment system ceased, as even the youngest leucogranite bodies are consistently restricted to the footwall and are often truncated by faulting (Burg et al., 1983; Searle et al., 1997; Murphy and Harrison, 1999; Searle and Godin, 2003). In fact, many of the current age constraints for movement on STD faults are single dates which only establish that a part of the fault system was active at a certain time. A lower age limit for slip on the STDS is provided by the initiation of north-trending normal faults in southern Tibet which locally crosscut the detachment system at 8 ± 1 Ma in the Nyainqentanghla Shan mountains ~ 100 km northwest of Lhasa (Harrison et al., 1995) and 11.9 Ma at Wagye La, Bhutan (Wu et al., 1998). These crosscutting normal faults should not be confused with those of the STDS, as they are not genetically related. Rather, these faults are associated with the end of metamorphism, melting and exhumation in the High Himalaya (Searle et al., 2002), and they have formed in response to east-west extension and lateral collapse across the southern margin of Tibet, producing structures that in many ways resemble metamorphic core complexes in the western United States.

There is arguably no better place to study this structure than in the Everest region, where glacial erosion has revealed a cross section of the STD and incised valleys to the north of Everest (e.g., Rongbuk Valley; Figure 5) have unveiled fantastic down-dip

exposure. On the Everest-Lhotse-Nuptse massif, the STD is believed to be comprised of two strands; the lower Lhotse detachment which formed first, and the upper Qomolangma detachment (Figures 4 and 7). The Lhotse detachment is modeled to dip less steeply than the Qomolangma detachment and, consequently, these faults merge to form one large shear zone north of Everest in the Rongbuk Valley. Here, the STD places largely unmetamorphosed Paleozoic sedimentary rocks over high-grade metamorphic rocks of the Greater Himalayan Sequence, which is locally comprised of nearly 50% leucogranite sills and dikes that are restricted to the footwall (Wager, 1965; Burg et al., 1983; Murphy and Harrison, 1999). Superposed low-angle normal faults like the Lhotse and Qomolangma detachments are not the only instance where the STD is bifurcated; other examples occur in Tibet near Khula Kangri (Edwards et al., 1996) and east of Manaslu in the Nar valley (Godin et al., 2006*b*). Much like on Everest, in these locations the lower strand was active first and the structurally higher strand second.

Lhotse Detachment (Lhotse Shear Zone)

The Lhotse detachment was first identified by Searle (1999*a*) and it marks the contact between the Greater Himalayan Sequence crystallines below and the North Col Formation above (Figure 4). As suggested by Searle et al. (2003), this structure marks a distinct break in metamorphic grade between upper-amphibolite facies sillimanite gneisses of the Greater Himalayan Sequence below, and middle to upper greenschist facies schist of the North Col Formation above. However, a comprehensive geothermobarometric study by Jessup et al. (2008) of rocks above, within and below the Lhotse detachment showed that metamorphic temperature is nearly isothermal across this

structure, although a break in pressure from ~6 to 3 kbar does occur. This break in pressure is due to Eohimalayan metamorphism that is preserved in the hanging wall of the Lhotse detachment, versus low-pressure Neohimalayan metamorphism that is dominantly preserved in the footwall Greater Himalayan Sequence rocks. Searle (1999*a*) and Searle et al. (2003) propose that no leucogranite bodies crosscut the Lhotse detachment structure, making it the upper limit of leucogranites in the Everest region. The Lhotse detachment is believed to wrap around the Nuptse leucogranite (Figure 6c; Searle et al., 2003) and crystallization of the Nuptse leucogranite at *c*. 23 Ma may signify the onset of movement on the Lhotse detachment when shearing in the Greater Himalayan Sequence was transferred into the overlying Everest Series during exhumation (Jessup et al., 2008). The only other timing constraint is proposed by Searle et al. (2003) who used U(-Th)-Pb dating of metamorphic monazites from schist sampled near Hermit's gorge (Figure 5) to suggest that this structure was active from 18.3 ± 0.2 Ma to 16.9 ± 0.2 Ma. The true nature and location of this structure, as well as the true vertical extent of leucogranites on Everest, may remain poorly understood due to limited exposure at the structural level of the Lhotse detachment. Also, due to a lack of evidence for a discrete fault surface and the absence of a jump in metamorphic grade, this structure is more appropriately referred to as a broad shear zone rather than a discrete detachment (e.g., Leloup et al., 2010).

Qomolangma Detachment

The Qomolangma detachment represents the upper splay of the STD exposed on Mount Everest (Figure 1, 4 and 7). This structure was first identified just north of

Everest in the Rongbuk Valley by Burchfiel et al. (1992) and Hodges et al. (1992) who described it as a north-northeast dipping, normal-sense fault separating unmetamorphosed limestone from sillimanite-grade gneiss, migmatite and leucogranite. Using aerial photographs, the report of Wang and Zhen (1975), an unpublished map from the successful Chinese accent of Qomolangma in 1975, and binocular reconnaissance, the Qomolangma detachment has subsequently been projected up-dip to the uppermost part of Mount Everest (Burchfiel et al., 1992; Hodges et al., 1998) where it is presumed to mark a sharp discontinuity in metamorphic grade between "unmetamorphosed" Tethyan limestone of the Qomolangma Formation in the hanging wall and greenschist facies rocks of the Yellow Band in the footwall below (Sakai, 1997; Searle, 1999*a*; Searle et al., 2003; Sakai et al., 2005). Nowhere along the exposed transect of the Qomolangma detachment can hanging wall rocks be matched to footwall rocks, and an absolute minimum displacement of 35 km has been proposed (Burchfiel et al., 1992).

While mapping along the Rongbuk glacier, Burchfiel et al. (1992) and Hodges et al. (1992) identified the Rongbuk granite pluton which they inferred to crosscut the Qomolangma detachment, although no direct observation of this was reported (Murphy and Harrison, 1999). Hodges et al. (1998) expanded upon this interpretation by dating a float sample from the Rongbuk granite using $^{40}Ar/^{39}Ar$ geochronology of muscovite and biotite to constrain movement along the Qomolangma detachment at 16.67-16.37 Ma. However, based on field observations, Wager (1965) and Burg et al. (1983) described all leucogranites in the Rongbuk region to be restricted to the footwall of the detachment, and subsequent field mapping by Murphy and Harrison (1999) confirmed that no leucogranite bodies crosscut the detachment. As reviewed earlier in this paper, the latter



Figure 7. View looking to the northeast at Everest and Changtse with the gently dipping Qomolangma detachment denoted by the red line. Notice that lithologies are repeated on each peak. (QF) Qomolangma Formation; (YB) Yellow Band; (ES) Everest Series.

authors used Th-Pb ion-microprobe dating of monazites from three variably sheared and mylonitized leucogranites immediately below the detachment to provide the only timing constraint of movement on the Qomolangma detachment, which ranges from 16.8 ± 0.8 Ma to 16.2 ± 0.8 Ma. The interpretation that the Rongbuk granite crosscuts the detachment (e.g., Hodges et al., 1998) has severe implications for the timing of slip along this strand of the STDS, as it places a lower limit on movement along this fault. Nowhere else along the STDS have leucogranites been mapped cutting across the fault plane into Tethyan rocks (Burchfiel et al., 1992; Edwards et al., 1996; Searle et al., 1997; Wu et al., 1998; Searle and Godin, 2003), nor do they appear to cut the Qomolangma detachment in the Everest region. To date, the best estimate for a lower constraint on detachment faulting in the Everest region comes from investigations in southern Tibet, which show that faulting ceased between *c*. 11-13 Ma (Cottle et al., 2011; Leloup et al., 2010).

CHAPTER 4

THE QOMOLANGMA FORMATION

Qomolangma Formation

On June 8th, 1924 George Mallory and Andrew Irvine vanished while climbing the northeast ridge of Mount Everest; Noel Odell, a geologist, was the last person to see them before they disappeared (Gansser, 1964, p. 162). On that same day, Odell climbed to 8,200 meters in excellent conditions to search for the climbers; in the process he became the first person to confirm that limestone forms the summit of Everest (Odell, 1925; Gansser, 1964, p. 162). In spite of modern advances in technology to improve the safety and consistency of summiting Mount Everest, sampling exposed rock above 7,000 meters has remained a challenge (Searle, 1999). Due to the consequent paucity of samples from the Qomolangma Formation, much of what we know about this formation has been inferred from samples collected at summit outcrops and, until this study, a structurally continuous sampling of the Qomolangma Formation on Mount Everest has not been documented.

Previous Research and Characterizations

The first documented description of the Qomolangma Formation came from a sample collected by Lawrence Wager during the 1933 Everest expedition. On May 29th, during their unsuccessful summit attempt on the northeast ridge, Wager and Percy Wyn Harris reached 8,573 meters before turning back. Wager collected a small sample ~3 cm

across “from a band forming the first step” and described the specimen as “grey nobbly limestone, not noticeably metamorphosed” (Lawrence Wager Collection records, Oxford University Museum; see also Wager, 1934 and 1939). A more detailed description of this formation was subsequently provided by Gysin and Lombard (1959, 1960) and Augusto Gansser (1964, p. 158-164), using samples gathered by the successful Swiss and American expeditions of 1956 and 1963, respectively (also see Odell, 1967). Professor Gansser described the various Summit samples as being lithologically identical, and composed of thin-bedded, fine-grained, grey calc-schist or platy limestone. Detrital grains of primarily quartz with some albite and microcline were present, as well as “lamellae of sericite aligned with the schistosity.” Each sample contained crinoid fragments preserved as large uniform calcite crystals which stood out against the “finer-grained calcites of the groundmass.” More detailed petrographic descriptions of the Qomolangma Formation have been provided by Searle et al. (2003), Sakai et al. (2005) and Jessup et al. (2006). They summarize the formation as gray, thick-bedded limestone dipping between ~15-20° to the north-northeast on the summit of Everest, but decreasing to <5° in the Rongbuk valley to the north. They described it as a 225 meter thick, unmetamorphosed, impure limestone containing calcite porphyroclasts within a fine-grained matrix of either micrite (Sakai et al., 2005) or recrystallized calcite (Jessup et al., 2006). Searle et al. (2003) reported samples to have fragments of conodonts and corals, and one sample collected close to the summit contained 88% calcite, 9% dolomite, 2% quartz, and 1% illite/muscovite, had a preferred alignment of calcite grains into a strong foliation, and contained calcite porphyroclasts with deformation twins and strain-free detrital quartz grains. Jessup et al. (2006) noted undulose extinction in some detrital

quartz as well as other strain-free grains within the calcite matrix, and these authors as well as Searle et al. (2003) suggests deformation temperatures of < 200-250°C. In comparison, samples collected six meters below the summit of Everest by Sakai et al. (2005) contain abundant fragments of crinoids, trilobites, ostracods and brachiopods, and reportedly seemed to be much less sheared and recrystallized.

Correlation between the summit limestone and rocks of the Chiatsun Group in the Nyalam region indicate that a white-weathering bed within the summit limestone is a ~60 meter thick thrombolite unit (Figure 1), based on the thickness of the white marker bed and the distance from the top of a prominent dolostone marker bed (i.e., the Yellow Band on Everest) at both localities (Myrow et al., 2009). These white-colored beds occur throughout the summit limestone, the most prominent of which occurs halfway between the base of the Qomolangma Formation and the summit, and is best seen on the west ridge of Everest (Figure 1). The term thrombolite was first proposed by Aitken (1967) to describe non-laminated cryptalgal structures characterized by a macroscopic clotted fabric. Thrombolites are common microbial deposits in Cambrian and Early Ordovician carbonate rocks (Armella, 1994), although their distribution in the rock record steeply declines in the Middle Ordovician (Kennard and James, 1986).

There is limited data on the uplift history of the Qomolangma Formation, however, recent fission-track analysis of a transect of samples from the Everest region yielded an apatite fission track age of 30.5 ± 5.1 Ma for a sample collected from the summit of Mount Everest (Streule et al., 2012). This is interpreted by these authors as evidence for exhumation of Tethyan sediments in the Oligocene, during initial crustal thickening.

Age

Fossil fragments in the first samples collected from the summit were not preserved well enough to allow an age determination, and early geologists regarded the Everest summit limestone as Carboniferous to lower Permian (Odell, 1925, 1967; Wager, 1939; Gansser, 1964). Decades later, the Qomolangma Formation was reinterpreted to be Ordovician (Mu et al., 1973; Wang and Zhen, 1975). In 1975, the Chinese Academy of Sciences conducted a comprehensive geologic study of Everest's northern slope, proposed a stratigraphic division, and assigned the summit limestone to the Early to Middle Ordovician based on a fossil assemblage of brachiopods collected from the down-dip continuation of the summit limestone (Yin and Kuo, 1978; Yin, 1987). The age of the Qomolangma Formation was further refined by Myrow et al. (2009) using stratigraphic correlations with Cambrian-Ordovician strata to better constrain the age of rocks on the Mount Everest massif. Their work correlated the Qomolangma Formation to the time-equivalent Lower Chiatsun Group in the Nyalam region 75 km west of Everest, based on their similarity in structural position relative to the STD, lithology, and stratigraphic succession. The Lower Chiatsun Group has also been assigned to the Lower to Middle Ordovician based on nautaloid, brachiopod and conodont assemblages (Yin and Kuo, 1978; Yin, 1987; Burchfiel et al., 1992). Other time-equivalent formations have been identified, such as the Thaple Formation in the Zanskar Valley and the Thango Formation in the Spiti Valley (Myrow et al., 2009), but their lithology and structural proximity to the STD precludes them from being correlative with the Qomolangma Formation.

Depositional Setting

It is remarkable that the highest rocks in the world are marine limestones deposited approximately 470 million years ago, during one of the most biologically significant times on earth, the Great Ordovician Biodiversification Event (GOBE) (Webby et al., 2004; Harper, 2006). The GOBE saw an immense increase in marine biodiversity at the family level over a brief time span from 485 Ma to 460 Ma, and many consider this to be the most rapid increase in marine biodiversity during Earth history (Servais et al., 2010). This burgeoning of aquatic life is no doubt reflected in the summit limestone of Mount Everest, which has been reported by many to contain a range of fossils (Gansser, 1964; Odell, 1967; Searle et al., 2003; Sakai et al., 2005). The Qomolangma Formation is part of the Tethyan Himalayan Sequence, a continuous sedimentary succession deposited on the passive northern margin of India, along the eastern edge of Gondwana (Brookfield, 1993; Garzanti and Pagni Frette, 1991; Garzanti, 1999). At the time of deposition, Gondwana was the largest fused landmass on the planet (Figure 8), including within it Africa, South America, Antarctica, Australia and India, as well as other smaller landmasses. Despite the size of Gondwana, the Ordovician was a time of maximum dispersal of continents, occurring between episodes of the supercontinents Rodinia and Pangaea. Valentine and Moores (1972) recognized a correlation between times of such great continental dispersal and biological diversity, such that diversity was highest when continents were fragmented and lowest when they were amalgamated. They argued that during periods of continental dispersion, there was more opportunity for allopatric speciation. Thus, the two largest Phanerozoic radiations

can be related to the two largest supercontinent breakups, Rodinia and Pangaea (Servais et al., 2010).

In the Nyalam region of Tibet, carbonate rocks of the Lower Chiatsun Group have been traced eastward to the summit of Everest where they are correlated to the Qomolangma Formation (Myrow et al., 2009; Harper et al., 2011). On Everest, this package of Early to Middle Ordovician limestone is too heavily sheared and recrystallized to preserve depositional fabrics and intact fossils; thus, the depositional setting and fauna of the Qomolangma Formation are better inferred from the less deformed Lower Chiatsun Group. The Lower Chiatsun Group represents a transgressive sequence associated with global flooding of continental shelves (Algeo and Seslavinsky, 1995). This formation consists of bioclastic shelf limestones and peritidal dolomites deposited within warm, subtropical, mid-shelf carbonate environments (Harper et al., 2011). It contains crinoids, particularly cladid crinoids (Mu and Wu, 1975), as well as a brachiopod fauna from the plectambonitoidea and orthoidea superfamilies (Liu, 1976), which reflects the vast increase in brachiopod diversity during the Floian-Darriwilian (Harper, 2006). From available paleomagnetic data the zone of deposition for Tethyan sediments would have been proximal to the Indian craton at 30°S during the Early Ordovician, forming a part of the eastern Gondwana margin (Figure 8; Torsvik et al., 2009). Fauna of the Chiatsun Group in the Nyalam region have been compared to faunas of the Whiterock, Toquima-Table Head province, which extended around the margin of the Laurentian continent (North America) and developed in the early Darriwilian age of the Ordovician (Harper et al., 2011).

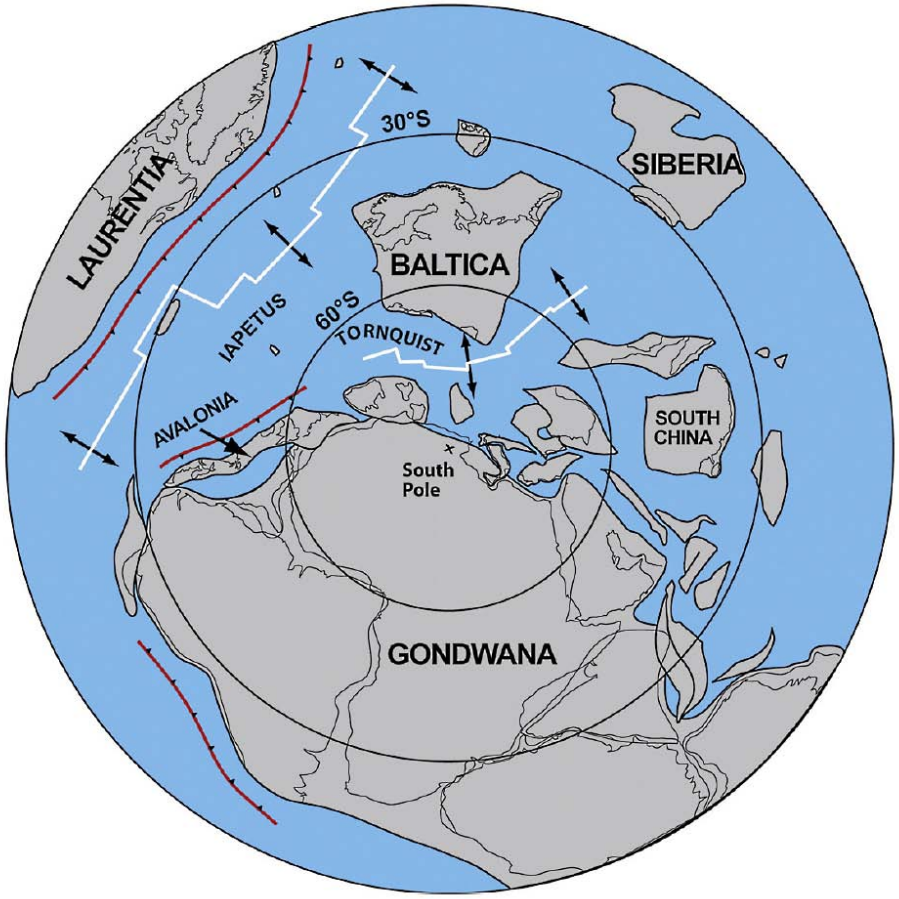


Figure 8. Paleogeographic reconstruction of landmasses during the Early-Middle Ordovician (Servias et al., 2010)

CHAPTER 5

METHODS

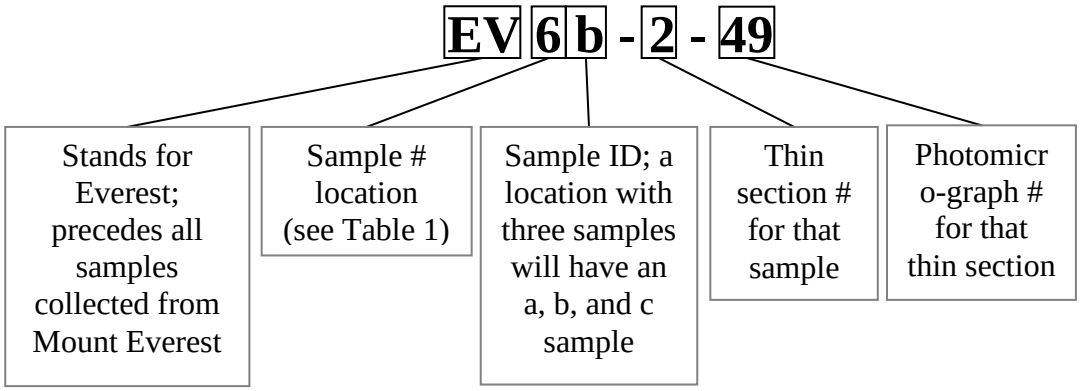
Sampling Strategy and Sample Processing

The samples for this investigation were collected during the *Everest Education Expedition*, also known as the National Geographic *Legacy* expedition, in the spring of 2012 with the help of Sherpa climbers. In an effort to overcome the challenge of sampling rock above 8,000 meters, we employed Danuru Sherpa of Phortse, Nepal and Jangbu Sherpa of Makalu, Nepal; who, together, have nearly 20 successful accents of Everest. During our time on Everest, we had several planning and training sessions with Danuru and Jangbu, which were twofold: (1) to teach them the proper techniques of geologic sampling, ensuring that samples of a proper size were sampled from in-place outcrops; (2) to devise a rigorous, though realistic sampling strategy by using their extensive familiarity of the southeast ridge to predetermine locations that would have a high chance of exposed rock close to the climbing route. This plan sought to increase safety by reducing the time spent sampling, and to ensure that several samples were collected from multiple sites across the Qomolangma Formation.

The location of each sample was preserved by recording the altitude and topographic feature of the sample location on the sample bag (e.g., SS for South Summit, HS for Hillary Step) using a Sharpie and an altimeter attached to a neck lanyard. Afterward, the location of each sample was confirmed by using the information recorded

on each sample bag and verbal descriptions of the sample sites, coupled with the known position of the southeast ridge route.

All samples were cut into billets and made into 30 µm-thick petrographic thin sections. Due to the irreplaceable nature of these samples, and because many were quite friable, several hand samples were impregnated with epoxy to reduce the risk of losing sample material while cutting billets. The epoxy used was EpoThin, a low viscosity, fast drying epoxy made by Buehler; samples were impregnated using a bell-jar vacuum apparatus attached to a standard lab pump. Billets were then cut using a mounted circular saw with a diamond blade, and were cut orthogonal to one another. If a foliation or lineation was observable in hand sample, billets were cut normal to the foliation and parallel to the lineation, and if enough sample material was available, then additional billets were cut at other angles of interest. At least one thin section from each sample location was stained with alizarin red-S to help distinguish dolomite from calcite. In total, sixty five uncovered, micro-polished (1 µm) thin sections were made by Spectrum Petrographics. Labels that appear on the bottom right of photomicrographs are explained in the example diagram below:



Images with a name that does not have a photomicrograph number are full thin sections scans, or they are cropped from a scan.

Cathodoluminescence

Optical cathodoluminescence (CL) has been used for imaging of quartz and calcite grains to reveal crystal properties, not visible under a conventional polarizing microscope. Minerals of interest included calcite and detrital quartz grains within the matrix, fossil fragments, as well as any mineral occurring in dilation sites. Reasons for using CL in this study include: to determine if post-deformation static recrystallization of matrix grains occurred; obtain information on the provenance of detrital quartz grains; differentiate between diagenetic structures and deformational structures; and to ensure a thorough characterization of samples. See Appendix A for analytical conditions and instrumentation.

Calcite Twin Morphology Analysis

Twinning is a common phenomenon that can happen during the growth of a mineral or from an applied stress. Twins formed from stress are called mechanical twins or deformation twins and they occur when an applied stress is greater than the critical resolved shear stress (CRSS) of the mineral being twinned (Passchier and Trouw, 2005). Mechanical e-twinning in calcite is the dominant crystal-plastic deformation mechanism under 400°C (Groshong, 1988), occurring between 2 and 12 MPa (i.e., CRSS of calcite; Turner et al., 1954; Wenk et al., 1986). While twinning may be a function of differential stress with no temperature dependence (Rowe and Rutter, 1990), the morphology of

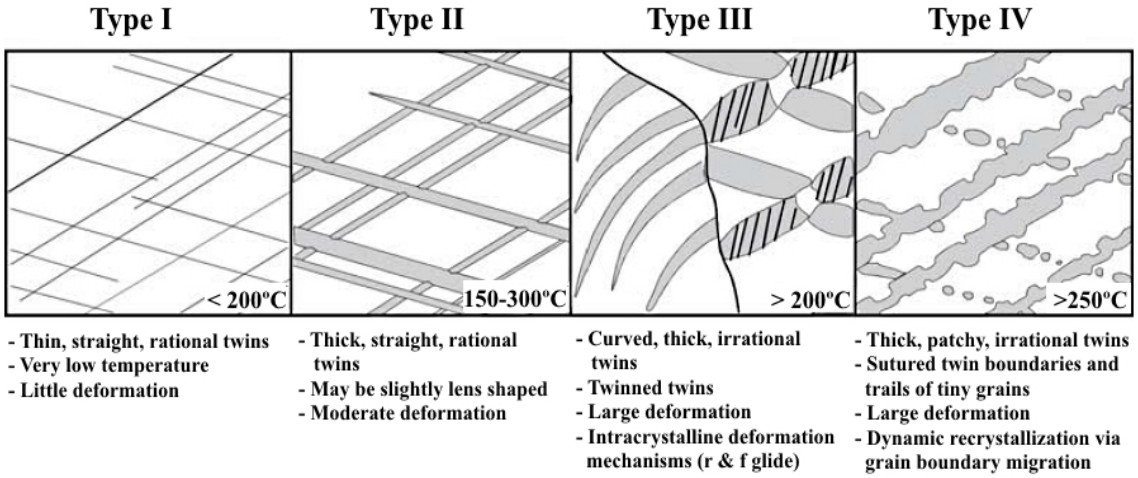


Figure 9. Calcite twin morphologies and their associated temperature regimes. Modified after Burkhard (1993).

calcite twins is significantly influenced by temperature (Burkhard, 1993). As a result, four types of calcite twin morphology and their associated temperature regime have been established (Figure 9; Burkhard, 1993; Ferrill et al., 2004). Ferrill (1991) recognized that twinning between 100-200ºC produces new narrow twins (type I and II), whereas above 200ºC deformation results in the widening of existing twins, and curved and twinned twins are common (type III); above 250ºC twins begin to dynamically recrystallize via boundary migration, forming patchy twins and serrated twin boundaries (type IV). In this study calcite twin morphology has been used to infer temperatures during deformation of the Qomolangma Formation.

Electron Backscattered Diffraction Analysis

Electron backscattered diffraction (EBSD) analysis is currently the most effective method for characterizing the crystallographic orientation of minerals in thin section, and

is commonly used in detailed studies of microstructures and deformation mechanisms. Since this type of analysis is rather new, especially for its purpose in geosciences, the concept and application of EBSD is briefly reviewed; for a more exhaustive treatment of this analysis refer to Wilkinson and Hirsch (1997), Prior et al. (1999), and Humphreys (1999, 2001). See Appendix A for sample preparation, analytical conditions and instrumentation.

EBSD is based on the principle that high-energy electrons are diffracted from a specimen surface after incidence with an electron beam generated in a scanning electron microscope. The electrons emitted from the sample's surface are considered backscattered electrons, and they describe conical trajectories for those which satisfy the Bragg equation. Imaged on a phosphor screen, these diffraction cones create a network of intersecting planes that define an electron backscattered diffraction pattern (EBSP) or Kikuchi pattern. The intersecting lines correspond to zone axes which are linked to the specimen crystal structure, allowing for lattice parameters to be recognized. Correctly relating a given EBSP to the mineral from which it is derived is known as indexing, and is done by software that rigorously compares the live EBSP to those of known simulation patterns. If indexed correctly, this defines the orientation of a crystal structure at a given point. Point data is gathered incrementally along line scans at an interval between points (step size) predetermined based on the purpose of the analysis and grain size of the sample. Automated acquisition of line scans across a predefined area on the sample surface is used to create orientation maps. In an orientation map, grain boundaries are calculated based on misorientation angles, such that grains are comprised of data points with mutual misorientations of, for example, $< 10^{o}$ and grain boundaries are drawn

between points with a misorientation difference of > 10º. A group of data points that comprise a grain are assigned a unique color based on their orientation and the result is known as an AVA diagram (*Achsenverteilungsanalyse* diagram; Sander, 1950, 1970) which expresses each grain as a color that is related to orientation by a defined color look-up table (Randle, 1992).

The crystallographic orientation of each point is plotted on a lower hemisphere equal area stereographic projection known as a pole (Figure 10), and the relative clustering of data points is telling of the orientation of the minerals in aggregate (Randle and Caul, 1996). For pole figures with a strong clustering of data points, it can be reasonably concluded that the lattice orientation of crystals is not randomly distributed, but is arranged in a systematic manner, known as a lattice preferred orientation (LPO). In plastically deformed rocks, LPO's typically form as a consequence of dynamic recrystallization (Bell and Etheridge, 1976; Poirier and Guillopé, 1979; Urai et al., 1986; Rutter et al., 1994) and they are an extremely useful microstructure for elucidating the history of deformation in tectonites (Passchier and Trouw, 2005). The clustering of data points in a pole figure can form many different patterns, such as strong "maxima" when points all plot in the same area, or "girdles" when points form into crossing bands. These different LPO patterns form in response to many competing factors, the most important of which is the slip system(s) that operated during deformation (Figure 10; Schmid, 1994). In this study EBSD analysis has been used to examine dynamic recrystallization fabrics in quartz and calcite, as well as to measure recrystallized grain size. Orientation data plotted on pole figures has been used to determine if a LPO is present and if so, what crystal slip system(s) activated to produce it. The activation of a given slip system can

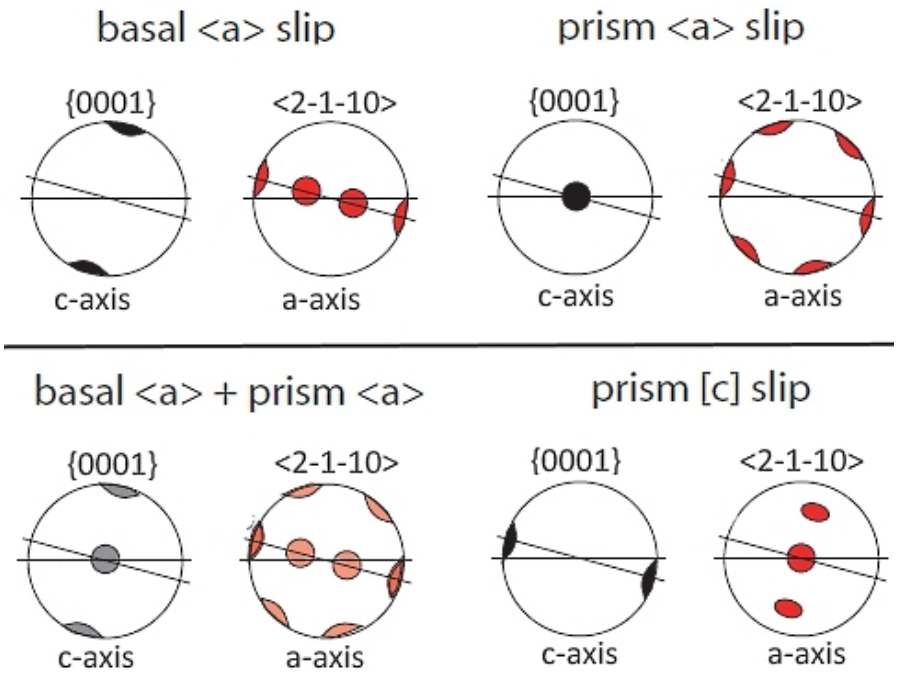


Figure 10. Examples of c-axis {0001} and a-axis <2-1-10> pole figures showing well-developed lattice preferred orientation patterns and the slip systems(s) that activate to create them.

provide insight to the temperature of deformation as each slip system activates under a specific temperature range (Stipp et al., 2002*a*; Passchier and Trouw, 2005).

Grain Size Measurements and Paleostress Calculations

It has been empirically shown that recrystallized grain size has an inverse relationship to differential stress, making it a valuable tool as a paleopiezometer (Twiss, 1977; Schmid et al., 1980; Ord and Christie, 1984; Rutter, 1995; Post and Tullis, 1999; Stipp and Tullis, 2003; Shimizu, 2008; Holyoke and Kronenberg, 2010). Differential stress analysis using dynamically recrystallized grain size was developed in the field of metallurgy and, subsequently, has been applied to deformed rocks (Mercier et al., 1977; Twiss, 1977). The equation and constants used to relate grain size to differential stress

have been empirically derived from the results of high-temperature, high-pressure experiments (e.g., Rutter, 1995; Stipp and Tullis, 2003; Holyoke and Kronenberg, 2010). In principal, this analysis is based on the understanding that for a mineral subjected to a given magnitude of differential stress, there is a grain size for which that mineral is stable. While dynamic recrystallization may be a thermally driven process, the grain size of dynamically recrystallized grains is diagnostic of the differential stress magnitude at the time of recrystallization (Twiss, 1977). Therefore, the recrystallized grain size of calcite and quartz has been used in this study to calculate differential stress during deformation of the Qomolangma Formation. Grain size measurements were done automatically using EBSD analysis (Prior, 1999; Humphreys, 2001), as well as manually using the line intercept method (Smith and Guttman, 1953; de Hoff and Rhines, 1968). Grain size measurements using EBSD were carried out on recrystallized calcite in samples from the Summit and Hillary Step, and on recrystallized zones within a large quartz vein in sample EV6b. Manual measurements of detrital quartz grains or mica laths were done using photomicrographs in the image analysis software Fiji (formerly called ImageJ), which was used to calculate grain size by finding the radius of an equal-area circle of traced grains.

Paleo-differential stress can be related to recrystallized grain size through the following formula:

$$\sigma = Cd^{-m}$$

where σ is paleostress in megapascals (MPa), d is the recrystallized grain size in microns (μm), and C and *m* are empirically derived constants for the mineral analyzed. For both

calcite and quartz there are different constants that have been calculated based on the mechanism interpreted to have operated during recrystallization (e.g., bulging vs. subgrain rotation recrystallization) (Rutter, 1995; Stipp and Tullis, 2003; Holyoke and Kronenberg, 2010). The constants used in this study are given in subsequent sections on paleostress calculations, once recrystallization mechanisms have been discussed.

One of the most realistic sources of error for paleostress calculations is the possibility of post-dynamic recrystallization static grain growth. Therefore, paleostress estimates from samples that show strong evidence of static recrystallization have been used with caution or omitted completely. Also, the average calculated grain size could be affected if relict grains or grains that have not recrystallized dynamically are used in the calculation. To avoid this pitfall, such grains were removed from the data set using the *Channel 5* EBSD post-processing software, and only matrix calcite grains with requisite characteristics of dynamic recrystallization were used.

Electron Microprobe Analysis

High resolution compositional data of white mica, biotite, chlorite, and tourmaline were acquired on an electron microprobe at the University of Minnesota's Department of Earth Sciences, and data for large deformed quartz veins in samples EV6a and EV6b were acquired at University of Tennessee, Knoxville. Composition data of individual mineral phases has been used to confirm the presence of certain minerals observed optically, to determine the exact species of white mica and tourmaline, and to use for other analyses such as Titanium-in-biotite geothermometry and geochemical analysis of tourmaline. For analytical conditions see Appendix A.

Geochemical Analysis of Tourmaline

There are currently 30 recognized species of tourmaline that comprise the tourmaline supergroup (Dutrow and Henry, 2014). Due to tourmaline's compositional and textural sensitivity to its host environment and its wide P-T stability range (Figure 11; Henry and Dutrow, 1996), it is a sensitive petrogenetic indicator to the conditions under which it crystallized (van Hinsberg et al., 2011*a*). Tourmalines are able to preserve such information through cycles of uplift, metamorphism and erosion because of negligible element diffusion in its crystal structure (van Hinsberg et al., 2011*b*) and due to its hardness and lack of cleavage, making it very resistant to weathering. The large range in composition of tourmaline is owed to its complex structural arrangements and its ability to incorporate many different cations and anions (Hawthorne and Dirlam, 2011).

$$XY_3Z_6[T_6O_{18}][BO_3]_3V_3W$$

X = □ (vacancy), Na, K, Ca, Pb^{2+},
Y = Li, Mg, Fe^{2+}, Mn^{2+}, Cu^{2+}, Al, V^{3+}, Cr^{3+}, Fe^{3+}, Mn^{3+}, Ti^{4+},
Z = Mg, Fe^{2+}, Al, V^{3+}, Cr^{3+}, Fe^{3+},
T = Si, B, Al,
B = B,
V = OH, O, and
W = OH, F, O.

Figure 11. General chemical formula for minerals in the tourmaline supergroup. Notice the wide range of substitutions for various lattice sites (modified from Hawthorne and Dirlam, 2011).

This makes tourmaline an extremely valuable tool as a forensic mineral (van Hinsberg et al., 2011*a*) and it has been used in this study to determine the source of metasomatic fluid.

Tourmaline grains within the secondary mineral assemblage found in South Summit samples were analyzed with an electron microprobe to acquire high-resolution chemical composition data (Figure 12; refer to Appendix B for raw composition data). The microprobe data was then used to determine the species of tourmaline present by calculating the structural formula for the various tourmaline grains analyzed. Structural formulas were calculated following the normalization procedure of Henry and Dutrow (1996), using a 31-anion normalization.

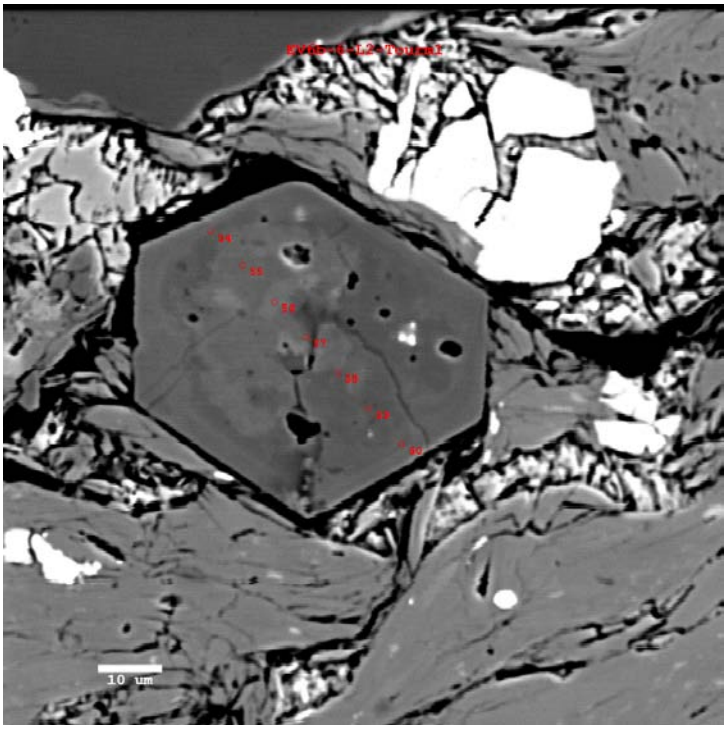


Figure 12. Example of an electron microprobe grain transect of a tourmaline found in South Summit sample EV6b. The red dotes indicate the location of each spot analysis.

Titanium-in-Biotite Geothermometry

The concentration of titanium in biotite as an indicator of metamorphic temperature is a geothermometer pioneered by Henry et al. (2005) for low-to-medium pressure, peraluminous metapelitic biotites. The amount of trace element Ti that is incorporated into the crystal structure of biotite is controlled by temperature, pressure and the composition of biotite, though experimental investigation by Henry and Guidotti (2002) has shown that temperature is the most influential effect. For the best results, it is critical that the mineral assemblage be chemically similar to that of samples used to calibrate the geothermometer by Henry and Guidotti (2002) and Henry et al. (2005). The paragenesis should include quartz, aluminous phases (such as chlorite, staurolite, or sillimanite), Ti phases (ilmenite or rutile), and for samples equilibrated below upper-sillimanite grade, muscovite. This maximizes Si, Al, and Ti at saturation levels in biotite, essentially limiting the effects of bulk composition for these elements. It is also important that the mineral assemblage was equilibrated between ~3-6 kbar. Below this pressure range, Ti is more readily incorporated into biotite and therefore, results may produce artificially high temperatures (Henry et al., 2005).

In this study, electron microprobe data from biotites within the secondary mineral assemblage in South Summit samples has been used for Ti-in-biotite geothermometry (refer to Appendix B for raw composition data). All calculations were carried out following the methods of Henry et al. (2005), based on a 24-anion normalization. The metamorphic event that produced biotite in South Summit samples may have occurred at

pressures slightly lower than 3-6 kbar and therefore, the results from this geothermometer are interpreted as maximum metamorphic temperatures.

Titanium-in-Quartz Geothermometry (TitaniQ)

Titanium is a common trace element that is incorporated into the crystal structure of quartz through the substitution of Ti^{4+} for Si^{4+} on fourfold tetrahedral sites (Thomas et al., 2010). It has been shown that the amount of Ti that is integrated into quartz grown or recrystallized in the presence of rutile correlates to temperature, such that the concentration of Ti in quartz increases exponentially with increasing temperature (Wark and Watson, 2006). This relationship has led to the calibration of a thermometer that provides an estimate of metamorphic temperature, known as the *TitaniQ* geothermometer (Wark and Watson, 2006). Subsequent studies have refined this thermometer to account for the influence of pressure on the solubility of Ti in quartz (e.g., Thomas et al., 2010). Initial application of the TitaniQ thermometer was thought to be restricted to quartz crystallized at $\geq 400°C$, or recrystallized through grain boundary migration mechanisms. However, recent studies have shown that this thermometer is useful down to temperatures of ~350°C and that recrystallization through grain boundary bulging is also capable of equilibrating Ti concentrations in quartz (Haertel et al., 2013). Therefore, the TitaniQ thermometer may be used to infer temperatures of quartz growth or recrystallization, as the equilibration of Ti is achieved during either process (Spear and Wark, 2009).

In this study, TitaniQ geothermometry has been used on large quartz veins in sample EV6a and EV6b to provide an additional constraint on temperatures during deformation and metamorphism. Chemical composition data was gathered by electron

microprobe at the University of Tennessee, Knoxville and the operating conditions for each spot analysis is given along with raw composition data in Appendix C. To account for the effect of pressure on the solubility of Ti in quartz, all calculations were done using the formula of Thomas et al. (2010), which is:

$$RT\ln X_{TiO2} = -60952 + 1.520 \cdot T - 1741 \cdot P(\text{kbar}) + RT\ln a_{TiO2}$$

where R is the gas constant 8.3145 J/K, T is temperature in Kelvin, X_{TiO2} is the mole fraction of TiO_2 in quartz, and a_{TiO2} is the activity of TiO_2 in the system. Since rutile is abundantly present in EV6a and EV6b, calculations done in this study used a TiO_2 activity of 1; following the general assumption of Wark and Watson (2006) and Thomas et al. (2010) that if rutile is present the activity is effectively 1. A possible source of error for this analysis is compositions with Ti concentrations near or below the detection limit for the electron microprobe, which is about ~15 ppm. Therefore, data that yielded Ti concentrations below 15 ppm were not used for TitaniQ geothermometry.

$^{40}Ar/^{39}Ar$ Geochronology

The $^{40}Ar/^{39}Ar$ (argon-argon) method of numerically dating rocks is a geochronometer that has its foundation in the K/Ar (potassium-argon) isotopic dating technique (Merrihue and Turner, 1966; McDougall and Harrison, 1999). The K/Ar method is based on the occurrence and decay of radioactive potassium (^{40}K), an isotope with a half life of 1250 Ma. The decay of ^{40}K in potassium bearing minerals produces radiogenic argon (^{40}Ar) as a daughter isotope (Aldrich and Nier, 1948), and the accumulation of ^{40}Ar over geologic time is the basis for the K/Ar dating method (McDougall and Harrison, 1999). By using the known rate of decay for ^{40}K (1250 Ma)

and the measured ratio of parent to daughter isotopes of ^{40}K to ^{40}Ar, respectively, an age of the rock or mineral phase analyzed can be calculated. In the $^{40}Ar/^{39}Ar$ technique the quantity of ^{40}K is not directly measured, but is instead calculated from the amount of ^{39}Ar produced when a sample is irradiated in a nuclear reactor, which transforms ^{39}K into ^{39}Ar through interaction with fast neutrons. The quantity of ^{40}K can then be determined because the $^{39}K/^{40}K$ ratio is essentially constant in nature. Following irradiation, argon is extracted from the sample through fusion in an ultra high vacuum system or by melting the sample at incremental heating steps, causing the argon to release as gas (Wänke and König, 1959; Merrihue and Turner, 1966). Argon isotope ratios are then measured with a mass spectrometer. Because the abundance of ^{39}Ar is dependent on the amount of ^{39}K present in the sample and the ratio of $^{39}K/^{40}K$ is constant, the $^{40}Ar/^{39}Ar$ ratio is proportional to the $^{40}Ar/^{40}K$ ratio in the sample and, therefore, is proportional to age (McDougall and Harrison, 1999). For K/Ar and $^{40}Ar/^{39}Ar$ dating, it is assumed that all radiogenic argon accumulated since crystallization has been retained. However, heating events subsequent to crystallization (i.e., metamorphism) may cause argon to diffuse out of crystal lattice sites where argon is retained, resulting in argon loss; or at high enough temperatures, the mineral may completely recrystallize and the age will reflect the metamorphic event rather than the true sample age. In samples that have experienced partial argon loss the age data generated during incremental heating will reflect this as a spectrum of ages, from which a wealth of data about the thermal history of the sample may be inferred (McDougall and Harrison, 1999; Faure and Mensing, 2005).

In this study, $^{40}Ar/^{39}Ar$ geochronology has been used on muscovite, a dioctahedral mica capable of incorporating up to 9.7% potassium into its crystal structure (Nesse,

2011), and will begin accumulating radiogenic argon once cooled below ~350°C (i.e., closure temperature). Muscovite was manually extracted with an X-ACTO knife and tweezers from large aggregates of mica found as layers on the outside of South Summit sample EV6a. The material extracted was sent to the United States Geological Survey (USGS) $^{40}Ar/^{39}Ar$ Laboratory in Denver, Colorado, where analytical work was carried out by USGS research geologist Michael Cosca. Irradiation of the sample material was done in a nuclear reactor, followed by incremental heating of the sample with an infrared (CO_2) laser, and isotopic measurement of argon with a Mass Analyser Products (MAP) 215-50 mass spectrometer.

CHAPTER 6

RESULTS AND DISCUSSION

Stratigraphic Thickness and Dip Calculations

Current publications that describe the Qomolangma Formation and Yellow Band have approximated their thicknesses at 225 meters and 172 meters respectively (Sakai et al., 2005). In this study, we used a 1:5,000 meter scale topographic map created by Swissphoto, Zurich and edited by Bradford Washburn, to create a high-resolution geologic map of the upper portion of the Mount Everest pyramid (Figure 13). The precise placement of contacts between the Qomolangma Formation, Yellow Band and Everest Series has been done using a number of resources including: Google earth; gigapixel-resolution photos viewable on *Glacierworks.org*; high-altitude photos taken from helicopter provided by Simon Moro and Max Lowe; high-resolution photos taken during our field season on Everest; and photos donated by climbers and Sherpas a part of our expedition in 2012. These images have provided numerous perspectives for every aspect of Everest, except the Kangshung face.

Using this map, the dip and dip direction of the Qomolangma detachment have been calculated at 19.3° and 330°, respectively, using a three-point-problem technique. This dip angle has been used with the vertical and horizontal thicknesses of the Yellow Band and Qomolangma Formation, as determined with this map, to calculate stratigraphic thickness, yielding 164 meters for the Yellow Band and 242 meters for the Qomolangma Formation on Mount Everest.

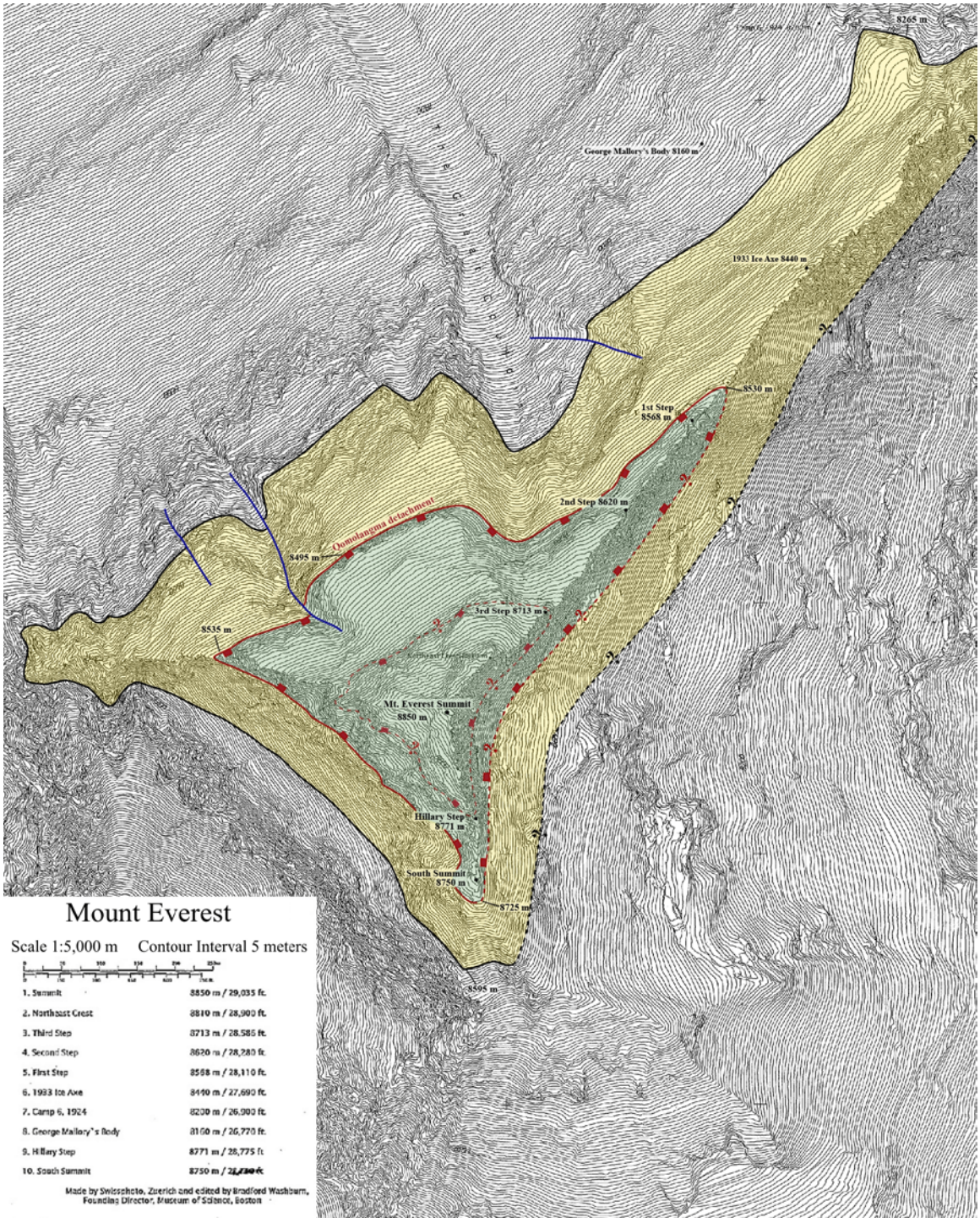


Figure 13. Geologic map of the summit pyramid compiled from an extensive collection of high resolution aerial photos, high-altitude images taken from helicopter, photos donated from climbers, and Google earth. (YB) = Yellow Band; (QF) = Qomolangma Formation. A possible structurally higher strand of the Qomolangma detachment is indicated. Topographic map made by Swissphoto and edited by Bradford Washburn.

The steep physiographic expression of the Hillary Step on the southeast ridge and the Third Step on the northeast ridge appears to form a continuous topographic feature that can be traced across the north and southwest face. This is seen on the topographic map used in Figure 13, and the topographic expression of this feature is very much like that created by the Qomolangma detachment. Consequently, a structurally higher strand of the Qomolangma detachment has been queried.

Qomolangma Formation Samples

Danuru Sherpa and Jangbu Sherpa collected eleven samples from six different locations during their descent from the summit of Mount Everest on May 25th, 2012 (Table 1). Qomolangma Formation Samples have been divided into four structural horizons: Summit samples, Busher Rock samples, Hillary Step samples, and South Summit samples. In this chapter, results from each of these structural levels will be presented in order from Summit to South Summit.

Summit Samples

Six samples were collected from outcrops exposed in the immediate vicinity of the summit. Sample EV1 is the highest elevation sample, collected from the uppermost exposed outcrop on the southwestern aspect of the summit, whereas samples EV2a and EV2b were collected closer to the southeast ridge and slightly lower than sample EV1 (Figure 1; Table 1). In total, 19 thin sections were produced from these samples. In hand sample, these rocks are light gray-green with patchy yellow staining, have visible stepped-calcite slip-fibers, and appear to be foliated.

Sample ID	Date Collected	Sample Location	Elevation (meters)	Sample Weight (grams)
EV1	5/25/2012	Summit	8840	334.63
EV2a	5/25/2012	Summit	8836	329.73
EV2b	5/25/2012	Summit	8836	424.9
EV3a	5/25/2012	Busher Rock	8811	237.49
EV3b	5/25/2012	Busher Rock	8811	80.74
EV3c	5/25/2012	Busher Rock	8811	252.26
EV4	5/25/2012	Hil. Step - Top	8783	180.62
EV5	5/25/2012	Hil. Step - Base	8764	169.67
EV6a	5/25/2012	South Summit	8750	103.23
EV6b	5/25/2012	South Summit	8750	290.82
EV6c	5/25/2012	South Summit	8750	102.39

Table 1. Pertinent information about the samples used in this study

Petrographic Observations

All Summit samples are lithologically identical and contain the common mineral assemblage calcite + quartz + dolomite + white mica ± pyrite ± zircon. Calcite has undergone significant grain size reduction via dynamic recrystallization, resulting in a matrix of fine-grained, slightly elongate, and strain-free calcite grains with an average grain size and aspect ratio of 8.32 μm and 2.03 respectively. Laths of white mica up to 250 μm in length with well-defined grain boundaries are dispersed throughout the matrix and are generally parallel to fabric, though more rare discordant mica laths are present as

well. Large, diagenetic pyrite grains up to ~800 μm are present along with trace amounts of small detrital zircon grains averaging ~20 μm. The extensive recrystallization of calcite and the development of stylolites has completely destroyed any primary depositional fabric of the original limestone. However, a few calcite porphyroclasts can be recognized as fossil fragments, which are some of the only distinguishable primary constituents found by this study. Most abundant of the fossil fragments identified are crinoid ossicles, ring-like discs that comprise the segmented stalk of a crinoid (Figure 14a; Benton and Harper, 2009). A brachiopod shell may also be present in one thin section, though extensive recrystallization precludes a definitive identification.

Alignment of elongate calcite grains forms a strong grain shape preferred orientation (GSPO), which defines a continuous foliation that is deflected around calcite and dolomite porphyroclasts creating augen structures, which in samples EV1 and EV2b, produces a well-developed mylonitic foliation (Figure 14a-d). Foliation is also defined by the differentiation of recrystallized grains into alternating bands of different grain size (Figure 15c). Based on observed microstructures and the proportion of recrystallized matrix, Summit samples are classified as calc-mesomylonites (White et al., 1980; Tullis et al., 1982; Passchier and Trouw, 2005). Calcite grains that have not been fully consumed by recrystallization remain as deformed porphyroclasts ranging in size between 250-1500 μm. These relict grains are characterized by type III and type IV deformation twins (Figure 9; Burkhard, 1993; Ferrill et al., 2004), and subgrain development within the grain and along its boundary, forming core-and-mantle structures (Figures 14c-e; White, 1976). Such twin morphology indicates deformation occurred at temperatures > 200°C (type III twins) and > 250°C (type IV twins) (Figure 9; Burkhard,

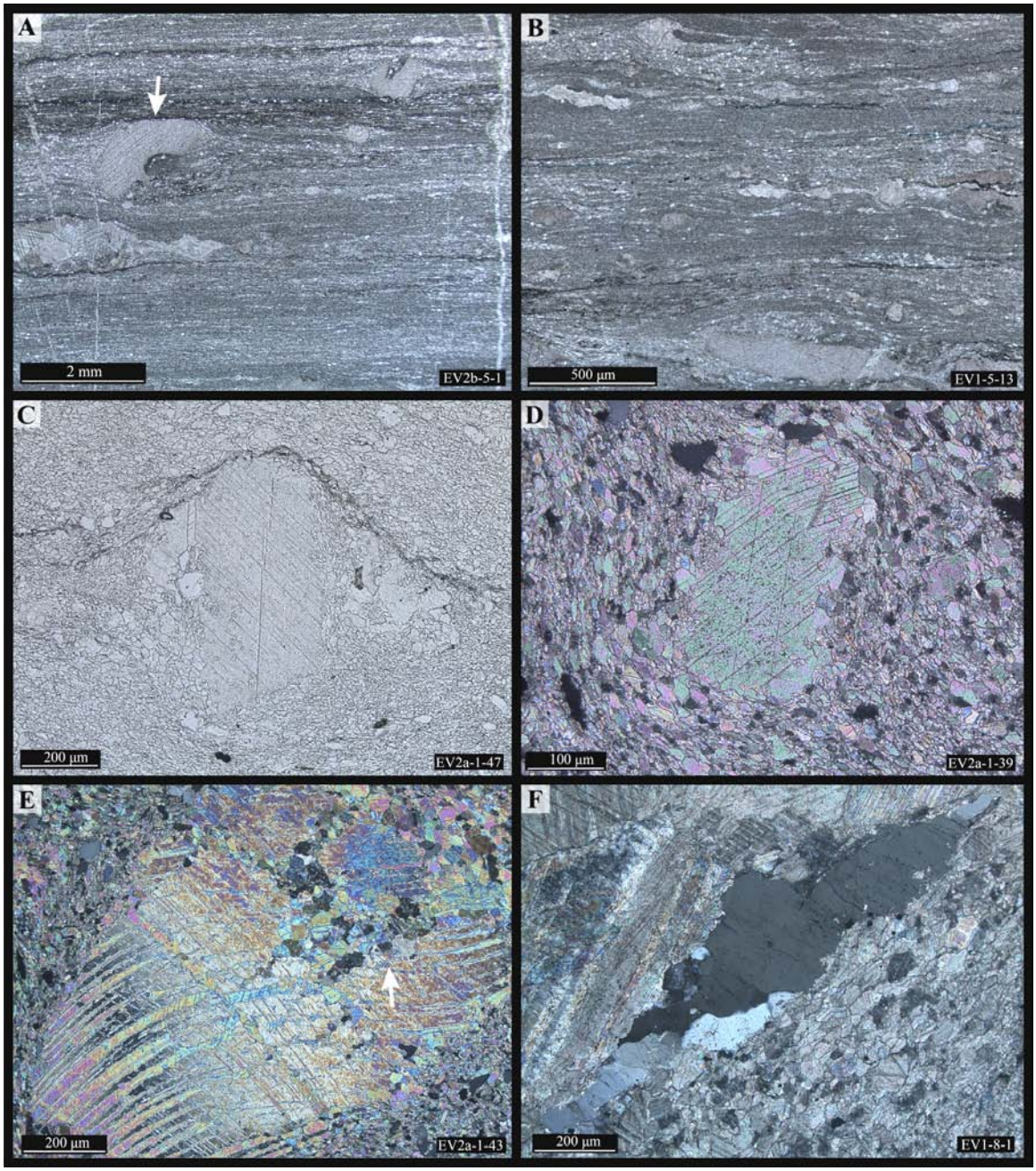


Figure 14. Photomicrographs of Summit samples; A-C are in PPL. A) Recrystallized grains and porphyroclasts define a mylonitic foliation; arrow denotes a crinoid ossicle. B) Mylonitic foliation typical of Summit samples. C) Calcite porphyroclast draped by a strain cap; calcite grains have crystallized in the strain shadow to the right of the clast. D) A small porphyroclast creating a perturbation in the flow fabric. E) Porphyroclast with type IV deformation twins, T > 250°C (Burkhard, 1993); notice the serrated nature of the twin boundaries, typical of type IV twin; subgrain formation indicated by the arrow as well as along the periphery of the clast. F) Quartz vein with sweeping and patchy undulose extinction indicating deformation at ~280 ± 30°C (Stipp et al., 2002*a*).

1993). Dynamic recrystallization becomes an important deformation mechanism in course grained calcite at temperatures above 250°C (Burkhard, 1993) and can occur within grains or along grain and twin boundaries producing serrated, jigsaw-like boundaries (Schmid et al., 1980; Groshong, 1988; Burkhard, 1993). Recrystallization can entirely destroy primary rock textures, often leaving a texture characterized by large relict grains surrounded and invaded by new, strain-free recrystallized grains (Schmid et al., 1980; Ferrill et al., 2004) whose size is a function of differential stress at the time of recrystallization, such that grain size decreases with increasing differential stress (e.g., Twiss, 1977; De Bresser et al., 2001). For example, the large grain at center in Figure 14d is partially recrystallized along the edge of the grain, producing a serrated grain boundary. Recrystallization of the large porphyroclast in Figure 14e has taken place along the periphery of the clast as well as inward from the boundary, forming a cluster of recrystallized grains within the upper right portion of the porphyroclast. The new, recrystallized grains observed here and in most porphyroclasts are similar in size to the recrystallized grains in the matrix, suggesting that recrystallization was accommodated through subgrain rotation (Passchier and Trouw, 2005). Several studies on naturally deformed marble and limestone have shown that the onset of dynamic recrystallization in calcite coincides with metamorphic temperature between 250-350°C (Mosar, 1989; Burkhard, 1993; Ferrill and Groshong, 1993; Evans and Dunne, 1991) and the formation of shear zones in carbonate rocks occurs at ~275°C (Schenk et al., 2005). While the calcite twin morphologies presented here suggest that deformation occurred at temperatures > 250°C, the microstructural evidence for widespread dynamic

recrystallization of calcite gives further evidence that temperatures during deformation were at least this high.

Dark seams of insoluble material occur throughout all Summit samples as strain caps around porphyroclasts (Figure 14c) and along dissolution surfaces as stylolites (Figure 15a and 15b), indicating pressure solution. Foliation-parallel stylolites are thick and wavy, suggesting that the clay content of the protolith limestone was > 10% (Van der Pluijm and Marshak, 2004). Laths of white mica commonly occur within aligned seams of insoluble residue, presumably having been reprecipitated from fluid saturated with ions from dissolved calcite, detrital mica and clay. Pressure solution and stylolite formation is typically associated with upper-crustal, diagenetic conditions. However, Rutter and Brodie (1988) have shown that pressure solution can operate under lower-crustal conditions within shear zones, in sufficiently fine-grained material. In fact, pressure solution is an important, though poorly understood, deformation mechanism that can operate at all crustal levels (Wheeler, 1992). Important to this study is: (1) pressure solution is controlled by diffusion along boundaries of individual grains, and therefore smaller grain size encourages the process; (2) the activation energy for diffusion is usually lower than for dislocation creep, so pressure solution will dominate at lower temperatures; (3) pressure solution commonly operates coeval with other deformation mechanisms, primarily dislocation creep (i.e., dynamic recrystallization; Rutter and Brodie, 1988). In light of this, it is possible that pressure solution operated at all phases of deformation, especially during and after dynamic recrystallization, facilitating deformation in the fine-grained matrix through dissolution-precipitation creep (den Brok and Spiers, 1991). Although evidence of this is rarely preserved, it appears that pressure

solution was at least a dominating mechanism in the final phases of deformation, as seen by well-developed stylolites that truncate the matrix flow fabric at moderate angles (Figure 15a and 15b). The transport of dissolved material away from sites of dissolution over some distance is supported by veins present throughout Summit samples (Figure 15a; Passchier and Trouw, 2005), which also suggests that stylolite formation may have led to an unknown amount of volume loss through diffusive mass transfer.

Past studies of the Qomolangma Formation have characterized it as a micritic limestone (e.g., Sakai et al., 2005); however, the average recrystallized grain size of calcite in Summit samples is ~8 μm, whereas micrite is between 1-4 μm (Folk, 1962). Also, the fine-grained calcite observed in this study has distinguishable grain boundaries and extinction, opposed to micrite which would have poorly-defined grains and typically a non-translucent, dark gray appearance under a polarizing microscope. Therefore, petrographic evidence from this study does not support the interpretation that the Qomolangma Formation is a micritic limestone.

Detrital quartz grains are scattered throughout the matrix and are equant to elongate, sub-angular to sub-rounded, range in size between 25-125 μm, and are locally present in large quantities. Many of the detrital quartz grains have patchy or sweeping undulose extinction (Figure 14f), indicating that deformation temperatures reached ~280 ± 30ºC (i.e., minimum temperature for the onset of plastic deformation of quartz; Stipp et al., 2002*a*). Some past characterizations of the Qomolangma Formation have described it as a “sandy limestone” (Jessup et al., 2006); however, this quality is probably not entirely an inherent trait of the original limestone. Instead, the apparent concentration of quartz is due to extensive volume loss during the dissolution and removal of calcite through

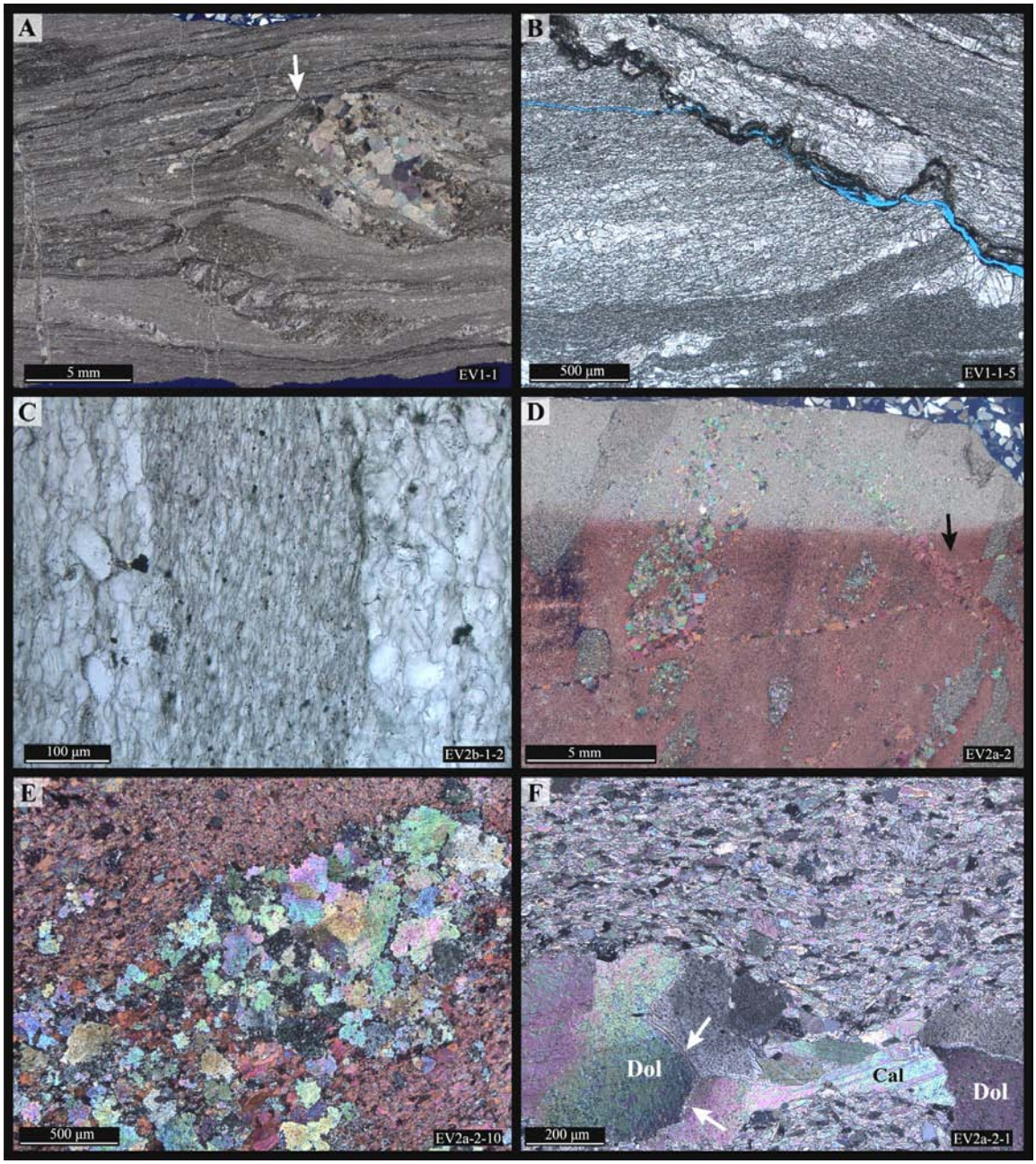


Figure 15. Photomicrographs of Summit samples; B and C are in PPL. A) Stylolites truncate fabric at a moderate angle (arrow); notice the early, offset veins and a late stage vein that overprints fabric at the left of the image. B) Higher magnification photo of truncating stylolite seen at the arrow in A; slight orientation difference between images. C) Grain size differentiation in the recrystallized calcite matrix; a common trait of a mylonitic foliation. D) Aggregates of secondary dolomite revealed by staining (calcite = red) and a shear fracture (arrow). E) Higher magnification image of an aggregate of secondary dolomite. F) Primary dolomite porphyroclast (Dol) creates a perturbation in the flow fabric. There appears to be boudinage of the dolomite and large calcite grains (Cal) have crystallized in the stress shadow between the two rigid dolomite grains.

pressure solution and solution transfer processes, which consequently increased the ratio of quartz to calcite. This may seem trivial, but it is an important consideration to make when resolving the depositional environment of the Qomolangma Formation. CL imaging of quartz in Summit samples shows that the majority of grains luminesce blue, which is typical of quartz with elevated concentration of trace titanium (Rusk et al., 2006).

Staining of Summit samples to distinguish between dolomite and calcite has shown that dolomite is quite common as nonplanar-anhedral (xenotopic) dolomite (Figures 15d - 15f; Gregg and Sibley, 1984; Sibley and Gregg, 1987; see also Boggs, 2003). There appears to be two generations of dolomite: (1) primary dolomite formed during diagenesis; and (2) secondary, hydrothermal dolomite formed syn- to post-deformation. Primary dolomite occurs as single, isolated grains set in the calcite matrix whereas secondary dolomite occurs in large aggregates. Grains of primary dolomite are distinguished by large grain size (500-800 μm), sweeping undulose extinction, and one or more curved crystal face (Figure 15f). These grains appear porphyroclastic (i.e., were a part of the pre-deformed carbonate protolith) and have characteristics of saddle dolomite as described by Radke and Mathis (1980). As seen in Figure 15f, these grains create perturbations in the flow fabric of matrix calcite in the same way as relict calcite porphyroclasts, demonstrating that they were present before deformation and fabric formation. The curved crystal faces leading to a pointed termination seen in the porphyroclastic dolomite grains found in Summit samples is a characteristic of saddle dolomite crystals of cement origin (Boggs, 2003). Therefore, saddle dolomite likely formed penecontemporaneously or mesogenetically as cement. Due to the greater

rheologic strength of dolomite compared to calcite (Jamison and Spang, 1976; Barber and Wenk, 2001; Davis et al., 2008), these grains have resisted significant deformation and recrystallization and now exist as relict porphyroclasts. Aggregates of secondary dolomite have numerous forms ranging from sprawling and ameba-like, to linear-elongate aggregates that are parallel to fabric (Figure 15d and 15e). Individual grains of secondary dolomite show no sign of deformation and are anhedral, amoeboid in shape, often contain a scattering of calcite inclusions, and have serrated grain boundaries (Figure 15e). Within a given aggregate of dolomite, grain size is unimodal, but there is a marked difference in grain size from one aggregate to the next, ranging between 75-200 μm. An important observation about these aggregates is they do not deflect the flow fabric; instead they overprint it, indicating that aggregate formation followed deformation or at least outlasted it. Unimodal grain size of replacement dolomite is suggested by Sibley and Gregg (1987) to indicate a single dolomite nucleation event on a unimodal carbonate substrate. Also, Scoffin (1987) proposes that secondary dolomitization that is fabric destructive forms at higher fluid flow rates, compared to fabric preserving dolomitization. This would imply that hydrothermal dolomite replacement happened during one event from a fluid that infiltrated the Qomolangma Formation at a relatively high rate. Inclusions of calcite further indicate that dolomitization was a replacement process that ensued at the expense of calcite.

Calcite veins that crosscut fabric at moderate to high angles and sometimes form aligned sets, are ubiquitous in most samples (Figure 15a and 15d). Vein-fill is composed of subhedral-euhedral calcite grains with rational twins that range in size between 200-500 μm. There have been multiple episodes of vein formation based on crosscutting

relationships, and the most recent generation crosscuts all other veins and fabrics (Figure 15a). Notice in Figure 15a the two veins of different generations have the same orientation, suggesting there was no change in the stress orientation between the two episodes of fracture formation. Many of the veins are calcite-filled shear fractures, which show offsets ranging from a fraction of a millimeter to several millimeters (Figure 15d). The formation of veins may have been facilitated by the dissolution of calcite during pressure solution, such that dissolved ions were readily available to be re-precipitated locally in dilation sites as veins. Other signs of late-stage brittle behavior in calcite are fractures that crosscut deformation twins in calcite porphyroclasts and unfilled fractures that traverse whole thin sections.

EBSD Analysis

Three successful EBSD analyses were done on sample EV2a to determine whether a lattice preferred orientation (LPO) is present within the recrystallized calcite matrix, as well as to measure grain size. The quality of the three EBSD analyses is quite good, averaging a ~91% index rate.

The combined average recrystallized grain size and aspect ratio of matrix calcite from all three analyses is 8.32 ± 3.77 μm and 2.03 ± 0.60 respectively. Orientation data for the three analyses is presented in pole figures as well as an orientation map from one analysis (Figure 16). Two of the three analyses appear to have a weak LPO shown by diffuse c-axis and a-axis maxima (Figure 16b and 16c). On the far left side of the orientation map (Figure 16a) is the margin of a large porphyroclast that is twinned (this grain is lighter in color because its orientation data has been removed from the data set).

The unique orientation of the twins and that of the host grain is represented by the colors blue and green; notice that immediately adjacent to the porphyroclast is a population of grains with these same colors, indicating the misorientation angle of the new grains is similar to the porphyroclast. These grains may represent a special type of LPO known as an "orientation family," indicating they were derived from the porphyroclast, and it is a feature typical of core-mantle microstructure (Passchier and Trouw, 2005). This, coupled with the observation that subgrains in porphyroclasts are similar in size to recrystallized grains in the matrix, suggests that recrystallization of calcite in Summit samples was accommodated by subgrain rotation recrystallization (e.g., Bestmann and Prior, 2003).

Before proceeding with further interpretation, to better understand the meaning of these data it is important to consider the factors and competing mechanisms that operate during deformation, especially with respect to recrystallization processes. The dominant deformation mechanisms change as conditions of temperature, stress, strain rate, grain size, and fluid content change and the microstructures that we observe in thin section are dominantly related to the last stages of deformation, formed shortly before conditions dropped below a critical value and the structures became "frozen in" (Passchier and Trouw, 2005). Therefore, what is seen in a deformed rock is typically an expression of the dominant deformation mechanism(s) that operated in the final stages of deformation. At low temperature, crystals respond to stress by brittle fracture and cataclasis, but at higher temperatures crystals may deform internally through intracrystalline deformation processes (Passchier and Trouw, 2005). Intracrystalline deformation involves the movement of lattice defects, known as dislocations, and vacancies through the crystal along lattice planes, allowing the crystal to reach a more stable state by decreasing stored

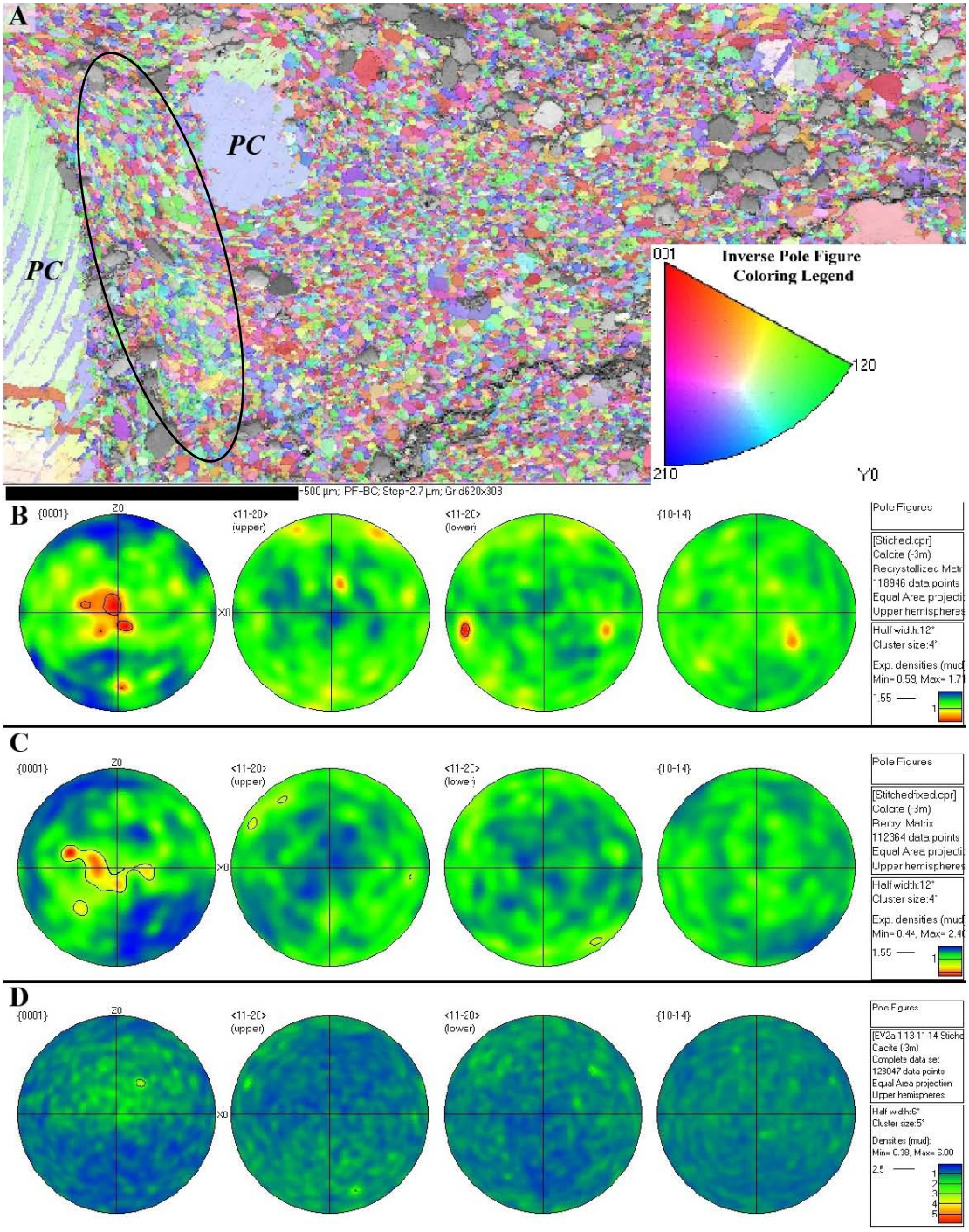


Figure 16. EBSD orientation data from three analyses done on EV2a. A) Orientation map for the analysis shown in B; (PC) = porphyroclast; notice the population of grains (circled) to the right of the twinned porphyroclast which have the same color as the twins; the left porphyroclast is the same as seen in Figure 14e and the right porphyroclast is the same as in Figure 14d. B) Pole figure for the analysis shown in A; a poorly-defined lattice preferred orientation (LPO) is present, and is defined by the red grains in the orientation map. C) Similar LPO as B. C) Very little indication of a LPO.

strain energy (Nicolas and Poirier, 1976; Guillopé and Poirier, 1979; Urai et al., 1986; Hirth and Tullis, 1992; Kennedy and White, 2002). This process may result in a permanent change in the shape of crystals or in complete recrystallization (Poirier, 1985; Hull, 1975). There are many different types of dislocations and styles in which they are translated through the crystal. Two important ways that defects pass through a crystal are known as dislocation glide for the migration of defects along specific crystallographic planes, or dislocation climb for the passage of defects over lattice obstructions such as dislocation tangles and lattice-site vacancies. Dislocation climb generally occurs at higher temperature than glide, and defects are able to migrate, or "climb," into other lattice planes, allowing them to pass obstructions. The combined process of glide and climb is known as dislocation creep, and it is an important process involved in the recrystallization of deforming minerals, often referred to as dynamic recrystallization. Dynamic recrystallization is a grain size insensitive (GSI) deformation mechanism which operates on relatively large grains and produces volumes of smaller, strain-free grains (Twiss, 1977; Rutter et al., 1994). Because dislocations will move in specific directions (known as the Burgers vector) in response to differential stress, a rock deforming through dislocation creep may develop a LPO (Passchier and Trouw, 2005) and, accordingly, there is typically a strong LPO in an aggregate of grains produced by dynamic recrystallization. But, other deformation mechanisms that operate coeval with, or after, dynamic recrystallization may partially or completely overprint that LPO (Vernon, 2004; Passchier and Trouw, 2005). As deformation proceeds, fine-grained aggregates may continue to deform, but may do so through mechanisms which favor finer grain sizes (< 10 μm) such as diffusion creep (e.g., Coble creep and Nabarro-Herring creep). Diffusion

creep is a grain size sensitive (GSS) deformation mechanism (Schmid, 1976) involving the migration of vacancies through the crystal lattice (Nabarro-Herring creep) or along grain boundaries (Coble creep), which may destroy an existing LPO (Knipe, 1989; Wheeler, 1992). It has been proposed that grain size reduction through dynamic recrystallization can lead to a switch from GSI dislocation creep to GSS diffusion creep (Schmid, 1976; De Bresser et al., 2001 and references therein). Urai and Jessell (2001) advocate that diffusion processes may contribute significantly to deformation while operating simultaneously with dislocation creep. De Bresser et al. (2001) further suggest that dynamic recrystallization leads to a balance between grain size reduction and growth processes, set up in the neighborhood of the boundary between the dislocation creep field and the diffusion creep field.

Microstructural evidence from petrographic observations in the preceding section strongly suggests that dynamic recrystallization did in fact operate, producing the fine-grained calcite matrix. However, the orientation data from EBSD analysis does not strongly support this, as weak c-axis maxima may only suggest that a strong LPO once existed (Figure 16b and 16c). Based on the microstructures observed in Summit samples coupled with somewhat ambiguous EBSD data, it seems likely that deformation originally proceeded by way of dynamic recrystallization which produced the fine-grained calcite matrix seen in all Summit samples. As temperature remained high, dynamic recrystallization likely continued to operate on any residual large calcite grains, whereas diffusion creep and dissolution-precipitation creep took over in the fine-grained calcite matrix, partially or completely destroying any LPO produced as a consequence of dynamic recrystallization. Once plastic deformation of calcite ceased, pressure solution

continued to operate, as indicated by tectonic stylolites that truncate the ductile flow fabric at low- to moderate-angles (Figure 15a and 15b).

Paleostress Calculation

Grain size data from three EBSD analyses of sample EV2a have been filtered to remove misindexed data points and points that correlate to non-recrystallized grains. In total, 34,099 grains were measured yielding an average grain size of 8.32 ± 3.77 μm. As previously mentioned, the microstructures observed in Summit samples suggest that calcite recrystallized dynamically through subgrain rotation. Accordingly, the constants calculated by Rutter (1995) for subgrain rotation have been used for paleostress calculations, which are 813 and .88 for A and *i*, respectively. Using these constants with the measured recrystallized grain size, a paleo-differential stress of ~126 MPa has been calculated. The accuracy of this measurement is dependent on the assumption that the apparent grain size is solely a function of dynamic recrystallization (dislocation creep), and that grains have not undergone any subsequent grain size change through other deformation mechanisms (diffusion creep). As discussed in the preceding section, it is possible that other deformation processes did in fact occur during and following dislocation creep. However, the effect that these deformation processes may have had on individual grains is restricted to grain growth and grain distortion, and cathodoluminescence imaging did not show any sign of static overgrowth. Thus, the observable grain size in thin section is probably greater than or equal to that immediately following dynamic recrystallization. Because differential stress is proportional to recrystallized grain size (smaller grain size = greater differential stress), paleostress

calculations here are taken as minimum estimates. Also, the formula and constants used in this calculation were derived by empirical studies that did not include temperature as a variable, which has been shown by De Bresser et al. (2001) to be a potential source of error in paleostress calculations for calcite using recrystallized grain size.

Significance

The purpose of differential stress calculations is to better understand the magnitude of stress at the time grain size reduction occurred in the development of a mylonitic foliation. In its most fundamental definition, a mylonite is formed in high-strain, ductile shear zones under conditions necessary for the operation of dynamic recrystallization; that is to say, conditions of greenschist facies or higher depending on the mineralogy (Bell and Etheridge, 1973; White et al., 1980; Tullis et al., 1982). Presented earlier in this section is evidence that temperatures reached those required for the onset of dynamic recrystallization in calcite (250-350ºC), as well as microstructural evidence supporting that dynamic recrystallization of calcite did in fact occur in Summit samples. Therefore, based on data presented in this section, it is concluded that the Qomolangma Formation at this structural horizon is a heavily sheared carbonate that has been deformed at temperatures of ≥ 250°C, and it is best described as a calc-mesomylonite.

Busher Rock Samples

Samples EV3a-EV3c were gathered along the southeast ridge at ~8,811 meters, at a location called Busher Rock (Figure 1; Table 1). At first, these samples were lumped

together with Summit samples due to similarities in lithology, degree of deformation and sampling proximity. But, detailed petrographic observations have revealed important microstructural differences between Busher Rock and Summit samples. Following a brief description of these samples, petrographic observations presented below will primarily focus on these differences and their relevance.

Petrographic Observations

A continuous foliation is defined by the alignment of elongate calcite grains and, to a lesser degree, by fabric-parallel veins (Figure 17b and 17e). Dolomite is present in the same fashion as in Summit samples, occurring as aggregates of secondary dolomite and as porphyroclastic grains of saddle dolomite which create perturbations in the flow fabric, exactly as seen in Summit samples (Figure 15f). No fossil fragments or depositional fabrics can be recognized in Busher Rock samples and porphyroclasts of calcite are scarce, if not absent. The only coarse grains of calcite occur in fabric-parallel veins, often showing type III and type IV deformation twins as well as subgrain development (Figure 17d). Within these veins are zones of quartz that have sweeping and patchy undulose extinction (Figure 17e), indicating that deformation temperatures reached ~280 ± 30ºC (Stipp et al., 2002*a*).

Three significant microstructural differences between Summit and Busher Rock samples have been recognized. (1) There are no residual calcite porphyroclasts in Busher Rock samples and the texture in these rocks has progressed to ultra-mylonite (Figure 17b and 17f). (2) The stylolites in Busher Rock samples are thick, diffuse bands that have been tightly folded by ductile shearing in the matrix (Figure 17c), in contrast to the well-

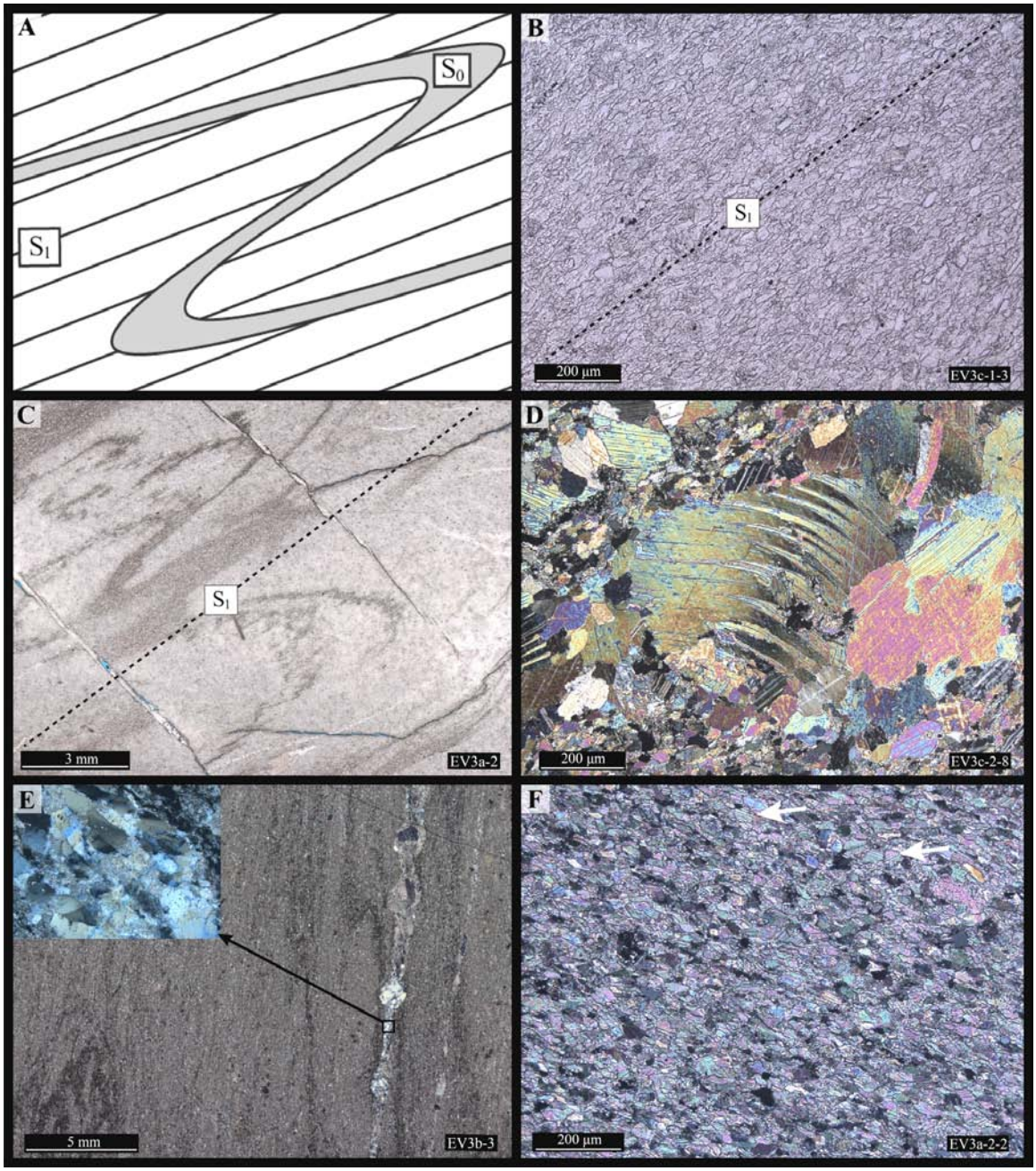


Figure 17. Photomicrographs of Busher Rock samples; B and C are in PPL. A) Illustration of folding of primary layering (S_o) during shearing and foliation development (S_1); related to images B and C. B) Continuous foliation is a secondary surface (S_1). C) Primary, diagenetic stylolites tightly folded by shearing and foliation development. D) Deformation twins that have begun to recrystallize along their boundary, forming type IV twins, indicating temperatures > 250°C (Burkhard, 1993). E) Quartz vein with patchy and sweeping extinction and sub-domains, indicating temperatures of ~280 ± 30°C (Stipp et al., 2002*a*, *b*). F) Matrix in Busher Rock samples; arrows point to slightly larger than average calcite grains that are twinned.

defined, wavy stylolites of Summit samples. The axial plane (axial surface in 3D) of these folds is parallel to the foliation surface, indicating that foliation and folds are genetically related (Passchier and Trouw, 2005). The bands of insoluble material are thought to have been compaction stylolites that formed during burial, which were then folded during deformation, causing them to become diffuse and poorly-defined. Folding of primary layering (S_0; in this case compaction stylolites) during shearing and foliation development (S_1; Figures 17a-c) is produced in ultra-mylonite at medium- to high-grade conditions (Passchier and Trouw, 2005, p. 123). The term "grade" in this instance is relative to the deforming material and its rheologic character, which in this case is calcite. Therefore, medium- to high-grade conditions relative to calcite are inferred to be $\geq 275°C$ (Schenk et al., 2005; i.e., the formation of shear zones in carbonate rocks). (3) There is a population of calcite grains in the recrystallized matrix that are slightly larger in size and have thin rational twins (Figure 17f). These grains are only slightly bigger than the primary population of strain free grains, but they may indicate changing deformation conditions, such as decreasing flow stress or post-recrystallization static growth. Overall, microstructural observations from Busher Rock samples are consistent with those from Summit samples, though there is evidence for an increase in the extent of recrystallization and degree of shearing at the Busher Rock structural level.

Hillary Step Samples

The Hillary Step (8,770 meters) is a historic point on the southeast ridge, named in honor of Sir Edmund Hillary, the first man to summit Mount Everest along with his companion Tenzing Norgay Sherpa in May 1953. The physiographic expression of the

Hillary Step is a steep, ~20 meter cliff that crops out nearly halfway between the summit of Everest and the bottom of the Qomolangma Formation (Figures 1 and 13). Two samples were collected at the Hillary Step, one at the top of the step (EV4) and one immediately below the step (EV5; Table 1). A total of five thin sections were produced from these two samples. In hand sample, both samples are grayish-green and rather fine-grained due to their cryptocrystalline texture, and sample EV5 had a dark, foliated or sheared zone running through the middle.

Petrographic Observations

The two Hillary Step samples are identical to each other in terms of lithology and microstructure, and are composed of the mineral assemblage calcite + quartz + white mica + albite ± zircon. Calcite has undergone extensive deformation and most or all original calcite grains have been consumed by recrystallization, such that relict porphyroclasts are absent (Figure 18). No fossil fragments are present, nor can any primary fabric be recognized in Hillary Step samples. Detrital quartz grains are scattered throughout the matrix of each sample much in the same way as Summit samples. These grains are generally sub-angular to sub-rounded, range in size between 40-200 μm, and are noticeably more elongate than those in structurally higher samples. A small proportion of quartz grains have sweeping or patchy undulose extinction and some detrital quartz grains are fractured perpendicular to their long axis, especially when they occur at a bend within a shear band (Figure 18b). CL imaging of quartz grains shows the majority of grains luminescence bright blue, indicating elevated concentrations of titanium (Rusk et al., 2006). Quartz grains seem to have acted passively during fabric

development due to their fine grain size, and because no dolomite or calcite porphyroclasts are present, there is little or no rheologic contrast in Hillary Step samples. Detrital albite grains occur in trace amounts and they are sub-rounded, average ~50 μm in size, and are easily distinguished from quartz by their synthetic twins. White mica laths up to ~300 μm in length with well-defined grain boundaries are scattered throughout each sample and are parallel to foliation (Figure 18a). Much like Summit samples, the penetrative fabric seen in Hillary Step samples is crosscut at moderate- to high-angles by calcite-filled fractures and microfaults (Figure 18d).

Thin section EV5-2 contains a significant amount of insoluble material that is concentrated into a ~1 cm thick band that diagonally crosses the thin section (Figure 18d); this is the previously mentioned dark band seen in hand sample. Although the complete mineral assemblage is represented in thin section EV5-2, the bulk of this dark band is comprised of smooth, parallel seams of opaque, insoluble residue (Figure 18e). Aligned white mica laths are abundant amongst these seams and their pristine grain boundaries suggest that they crystallized syn-deformation, rather than being of detrital origin (Figure 18e). Seams of opaque material are not stylolitic in nature and do not truncate individual grains or fabric along a dissolution surface, as stylolites do in Summit samples. The formation of this zone is likely related to fluids that acted as a critical dispersive and concentrating mechanism for dissolved material and insoluble residue, respectively. Dilation sites are partially comprised of local veins, although the possibility that dissolved material was completely removed by solution transfer must be considered. Interestingly, some seams within the dark band have been isoclinally folded and, though attenuation of their limbs makes it difficult to tell, appear to connect into a thin-section-

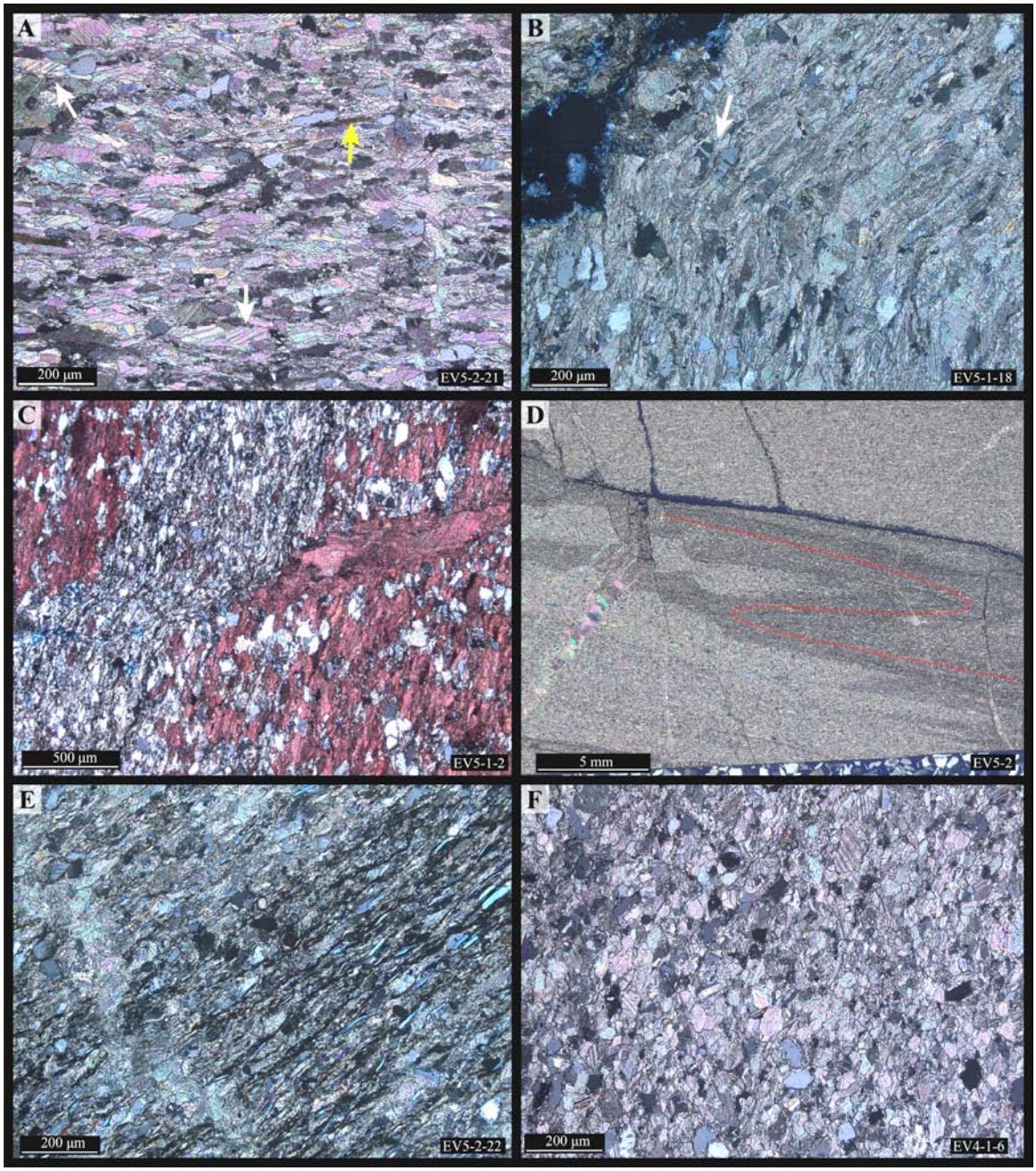


Figure 18. Photomicrographs of Hillary Step samples; all images are in XPL. A) Image showing the highly elongate nature of calcite and to a lesser degree quartz; white arrows = larger twinned grains; yellow arrow = mica lath. B) A shear band in the matrix foliation; arrow points to quartz grains fractured perpendicular to their long-axis. C) Shear band produced from offset along a shear fracture; red staining is for calcite. D) Thin section scan of EV5 showing a band of concentrated insoluble residue with seams of opaque material folded into a z-fold. E) Higher magnification view of the dark band in D; notice the abundant, foliation-parallel laths of mica. F) Thin sections cut perpendicular to the stretching direction of matrix grains look much like a marble.

scale z-fold (Figure 18d); this is similar to folding of diagenetic stylolites in Busher Rock samples (Figure 17c). The dextral shear sense indicated by this fold is nicely supported by the stair-stepping geometry produced by offset along microfaults that crosscut the band, suggesting that the orientation of principle stresses did not significantly change after temperatures dropped into the brittle regime.

Calcite comprises a matrix of elongate grains with an average grain size and aspect ratio of 21.06 ± 12.79 μm and 2.76 ± 1.15 respectively, as calculated from grains measured manually and using EBSD analysis. Because the EBSD map areas were not large enough to produce a representative average grain size, manual grain size measurements were also incorporated to ensure that an accurate average grain size was calculated. Results show that both grain size and aspect ratio have increased relative to structurally higher samples and there is greater variability in the size and aspect ratio of grains. Relative to Summit samples, the increased aspect ratio of calcite grains in Hillary Step samples has amplified the GSPO fabric. Because recrystallization has seemingly consumed nearly all porphyroclastic calcite grains, the mylonitic foliation seen in Summit samples is not present at the Hillary Step; instead, the alignment of elongate calcite, quartz and mica grains defines a continuous foliation (Figure 18a). In sample EV5 this foliation is bent into a shear band that appears to have formed in response to offset along a shear plane (Figure 18c), and a second larger shear band is present that cannot be clearly related to a genetic process as it is juxtaposed with the “normal” foliation along a shear fracture. Amongst the recrystallized matrix is a population of calcite grains of larger relative size ~59 μm, reflected by the large standard deviation in grain size. These larger grains commonly have rational twins, while populations of small grains are

generally strain-free (Figure 18a). Yet, these larger twinned grains are certainly a part of the recrystallized matrix and are not relicts of the original limestone. Consequently, the calcite matrix in Hillary Step samples can be divided into populations of smaller, strain-free grains and larger, strained grains. This attribute of Hillary Step samples is similar to that discussed for Busher Rock samples, which also has a bimodal grain size population, with the larger population being characteristically twinned. But, in Busher Rock samples this trait is rather obscure and is not as well-developed as it is in Hillary Step samples. It has been shown through experimental studies on naturally deformed carbonates that twinning of calcite is easier in coarser grains than in finer grains (Rowe and Rutter, 1990; Newman, 1994). Thus, for adjacent grains of different sizes, it is statistically more likely for the larger grains to accommodate the strain by twinning than the smaller grains. While this may explain the apparent selectivity of twinning, it is still ambiguous how two different grain size populations evolved alongside each other. It may have involved selective deformation controlled by the c-axis orientation of individual grains with respect to the orientation of stress axes, or perhaps post-deformational mimetic grain growth in the direction of the foliation (Passchier and Trouw, 2005). CL imaging of Hillary Step samples does not show any overgrowth structures or significant evidence that grains have grown statically.

Overall, the fabric, grain characteristics, and microstructures present in Hillary Step samples makes it difficult to precisely map the deformation path taken by rocks at this structural level. Seemingly, Hillary Step samples have experienced more sustained deformation or have experienced more than one cycle of deformation, and the observed fabric is most likely a function of the relative importance of different competing

processes during the final stages of deformation. In thin sections that do not reveal the elongate nature of calcite grains (i.e., cut perpendicular to the instantaneous stretching axis), the texture appears to approach that of a marble (Figure 18f). Accordingly, Hillary Step samples may be a transitional form between the calc-mylonites of Summit samples and the deformed marbles of the South Summit (described in subsequent sections).

EBSD Analysis

EBSD analysis has been used on Hillary Step sample EV5 to acquire orientation data for the recrystallized calcite matrix and to automatically measure grain size. Two successful EBSD analyses were completed with an average indexing rate of ~70%. The indexing rate was negatively influenced by a large amount of detrital quartz within the respective map areas, which did not index well due to the relief contrast between calcite and quartz.

The orientation data produced shows that Hillary Step sample EV5 does not have a LPO (Figure 19). These results may suggest that deformation through diffusion creep processes had a significant influence. If dislocation creep of calcite occurred, it would have likely produced a LPO which may have been destroyed by later grain-scale diffusion processes. The relict porphyroclasts seen in Summit samples suggest that the Qomolangma Formation protolith was limestone composed of course-grained calcite and fossils (refer to Chapter 7), that were then deformed and consumed by dynamic recrystallization. It is assumed here that the protolith limestone was approximately the same at all structural horizons across the Qomolangma Formation exposed on Mount Everest. Since the average grain size in Hillary Step samples is significantly lower than

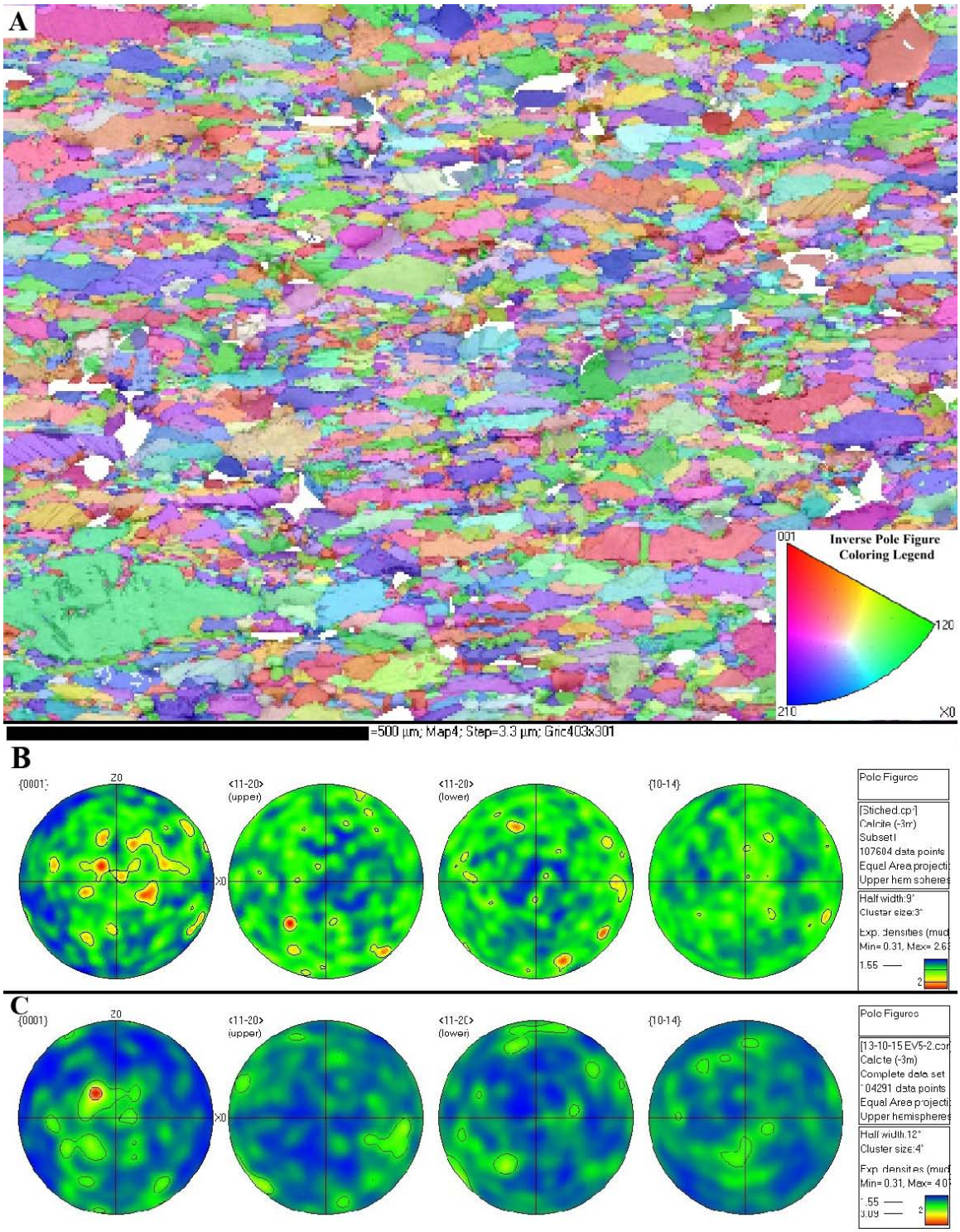


Figure 19. EBSD orientation data for the two analyses carried out on EV5; which together indexed ~70% on average. A) Orientation map corresponding to the pole figures in B. B) and C) Pole figures show that there is no lattice preferred orientation in sample EV5.

expected for a course-grained, fossiliferous limestone, it is evident that grain size reduction occurred during deformation, presumably through dynamic recrystallization. However, the mechanism responsible for grain size reduction is not explicit from the data presented here, especially since calcite grains in these samples are quite elongate and dynamic recrystallization typically produces relatively equant grains (Passchier and Trouw, 2005). This data, however, does support the operation of diffusion processes which can result in aggregates of elongate grains without a LPO (Passchier and Trouw, 2005). It is suggested here that the elongate nature of calcite grains is due to stress-induced pressure solution (e.g., dissolution-precipitation creep; den Brok and Spiers, 1991), which dissolves and removes material from sites of high stress and deposits material at sights of low stress, effectively reducing the length of one axis and increasing the length of another.

Significance

What is important about the Hillary Step samples is how the well-developed mylonitic foliation preserved in overlying Summit samples is not present, nor are there any course calcite grains or fossil fragments. A mylonitic foliation is produced in ductile shear zones under conditions necessary for dynamic recrystallization and with progressive shearing and deformation eventually all original grains will be consumed by recrystallization; or for a polymineralic rock, the rheologically weaker minerals will be. This seems to be the progression moving down-section from the Summit to Busher Rock to the Hillary Step, such that all original grains have been completely recrystallized. Without porphyroclasts of dolomite or calcite, and because quartz grains appear to have

acted passively due to their fine grain size, there would have been no rheologic contrast in the deforming material at the Hillary Step. Under these circumstances and with temperatures of ~250°C or higher, calcite appears to have accommodated differential stress through diffusion processes and by shearing in the matrix. These conditions explain the lack of a LPO and the noticeably more elongate nature of calcite, and only isoclinal folding of layering (Figure 18d) reveals the true intensity of strain at the Hillary Step. Overall, the Hillary Step samples do not offer any definitive resolutions, but they do suggest a progressive change in deformation conditions moving down-section from the summit area toward the base of the Qomolangma Formation.

South Summit Samples

The South Summit (8,750 meters) is a topographic prominence on the southeast ridge which serves as a staging area for climbers before they ascend the Hillary Step (Figures 1 and 13). In terms of its geologic significance, it marks the lower limit of our sampling transect across the Qomolangma Formation, at ~25 meters above the Qomolangma detachment. Three samples were collected from easily accessed outcrops exposed on the west side of the ridge, and a total of 13 thin sections were made (Table 1). In hand sample, EV6a is composed entirely of a quartz vein ~4 cm thick that is bounded between layers of mica. Sample EV6b is a greenish-brown, well-foliated specimen with a ~2 cm thick, foliation-parallel quartz vein that divides the sample in half. Sample EV6c is noteworthy for its orange to reddish brown color and an apparent spaced cleavage or very consistent fracture pattern. Overall, South Summit samples appear to be much more

crystalline and foliated relative to those from higher structural levels, and they do not look anything like a limestone.

Petrographic Observations

The metamorphic grade at the South Summit is higher than seen in structurally higher Qomolangma Formation samples, and samples here do not have any discernible depositional fabric, or relict calcite porphyroclasts, nor are there any fossil fragments. Instead, a continuous foliation is defined by multiple fabric elements including the alignment of micas, elongate grains, linear aggregates of coarse-grained calcite, and aligned zones of concentrated insoluble material.

The mineralogy is quite different as well, containing calcite + quartz + white mica + chlorite + biotite + tourmaline + rutile + albite ± microcline ± dolomite. This assemblage can be divided into minerals that have recrystallized from original constituents of the protolith (*primary* phases), those that crystallized predominantly from extrinsically sourced hydrothermal fluids (*metasomatic* phases), and those produced from reactions (*metamorphic* phases) involving primary phases, metasomatic phases and fluids of either intrinsic or extrinsic origin.

Primary phases consist of calcite, quartz and white mica, and together, these phases comprise what is considered to be the matrix in South Summit samples. *Metasomatic* phases consist primarily of white mica, chlorite, tourmaline and, in lower volume, albite and microcline. Since white mica and chlorite are aluminous phases, and aluminum is a relatively immobile element (Winter, 2001), these minerals are interpreted to have crystallized from an extrinsic metasomatic fluid that reacted with local pore fluids

enriched in aluminum from dissolved clays within the Qomolangma Formation protolith. Tourmaline occurs in large volume, and because it relies heavily on the availability of boron to form (e.g., Henry and Dutrow, 1996), metasomatic fluids are thought to have been rich in boron. *Metamorphic* phases consist of biotite and rutile, with biotite grains occurring isolated in the matrix while rutile grains occur exclusively within aggregates of white mica and chlorite. Biotite is interpreted to have formed from a continuous reaction between white mica and chlorite (Winter, 2001), which typically occur as aggregates adjacent to one another, whereas rutile is thought to have formed from a reaction between fluids of both intrinsic and extrinsic origin. The formation of rutile is dependent on the availability of titanium (Nesse, 2011) and because TiO_2 is relatively immobile, the titanium required must have been derived locally from within the Qomolangma Formation. In Summit samples there are no detrital grains of rutile or other titanium oxides that could have provided a local titanium source; instead titanium is thought to have been derived from detrital quartz grains. As discussed in previous sections, CL analysis of detrital quartz in Summit and Hillary Step samples shows that these grains are rich in Ti, based on their blue luminescence (Rusk et al., 2006). Therefore, rutile found within aggregates of metasomatic phases is interpreted to have formed from a reaction between metasomatic fluid and a titanium-rich fluid produced by the dissolution of titanous detrital quartz grains. Together, the *metasomatic* and *metamorphic* phases in South Summit samples will be referred to as *secondary* phases, or as the *secondary* mineral assemblage. With this context, the proceeding petrographic descriptions of South Summit samples will be discussed in terms of the *primary* mineral assemblage and the *secondary* mineral assemblage.

Primary Mineral Assemblage. Within the primary mineral assemblage, calcite grains are subhedral-euhedral, equant, and often form a mosaic of polygonal interlocking grains with rational and irrational twins averaging ~66 μm (Figures 20b, 21d and 21e). Zones of interlocking calcite are best developed in stress shadows formed around the large quartz vein in sample EV6b (Figure 20a). Some calcite grains are quite large (> 500 μm) and could be interpreted as original coarse grains of calcite from the protolith; however, given their well-developed crystal faces and the highly altered state of South Summit samples, it seems unlikely that they are original grains. Instead, these coarse grains have probably grown statically under elevated temperature from grains that recrystallized dynamically during an earlier phase of deformation. This is supported by CL imaging which shows equi-dimensional overgrowths that lead into well-formed grain boundaries (Figure 21e and 21f). As calcite grains grew larger, they eventually accommodated deformation by twinning, much like the population of large twinned grains in Hillary Step samples. Some of the large calcite grains have developed subgrains, possibly indicating a new cycle of dynamic recrystallization. The widespread growth of calcite suggests that rocks have progressed to marble at the South Summit.

Detrital quartz grains are scattered throughout thin sections, as they are in all Qomolangma Formation samples. They are sub-rounded to rounded and are noticeably more equant than the smeared, elongate quartz grains in Hillary Step samples. Many grains are littered with fluid inclusions which often trace the outline of a former crystal boundary that has been overgrown (Figures 21d, 22a and 22b).

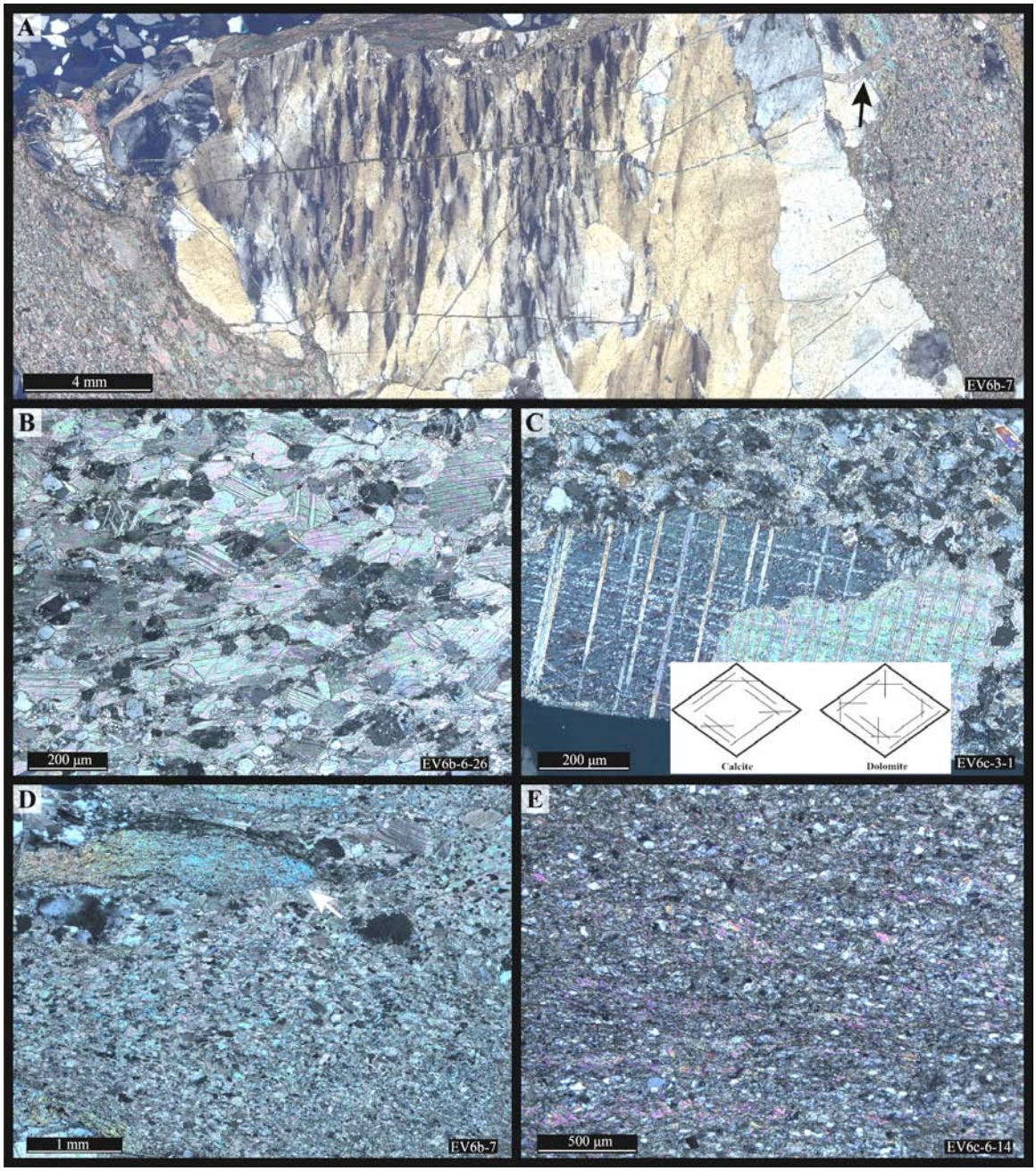


Figure 20. Photomicrographs of South Summit samples. A) Thin section scan of EV6b showing the large quartz vein with prismatic subgrains; arrow points to a fracture that crosscuts the vein, matrix flow fabric, and an aggregate of metasomatic phases. B) Statically recrystallized calcite in the matrix. C) Twinned dolomite grain within a large vein; schematic picture shows how twinning in dolomite differs than calcite (see Boggs, 2003 or Nesse, 2011). Above the dolomite grain is matrix typical of EV6c, which is rather devoid of calcite grains. D) Foliation-parallel aggregate of metasomatic phases including white mica, chlorite, tourmaline, and rutile. E) Sample EV6c showing a lack of calcite and abundant white mica and quartz.

Sample EV6c is largely devoid of any discernible calcite grains and it is mostly composed of equant quartz grains with sweeping undulose extinction that average ~35 μm in size, as well as muscovite and opaque phases (Figure 20e). This sample is likely a result of extensive dissolution and removal of calcite (diffusive mass transfer), leaving residual calcite as a mesh-like material mixed with insoluble residue between quartz grains that make up the bulk of the sample (Figure 20c). The only discernible grains of calcite comprise a large vein that crosscuts fabric at a high-angle and has grains of calcite up to ~3 mm. Though this sample has not been stained, dolomite is also present as recognized by its diagnostic twinning; dolomite twins parallel both the long and short diagonals of the cleavage rhomb forming perpendicular sets, whereas calcite twin lamellae only parallel the long diagonal of cleavage (Figure 20c; Boggs, 2003; also see Nesse, 2011). Deformation twinning in dolomite takes place on f-planes and generally does not occur below 300ºC (Barber et al., 1994; Passchier and Trouw, 2005), compared to calcite which can twin at room temperature. Also, quartz grains in sample EV6c are often in direct contact with each other and have sutured grain boundaries, suggesting pressure solution.

Secondary Mineral Assemblage. The secondary phases occur in varying concentrations in each of the three South Summit samples. In sample EV6a secondary phases are present, occurring on either side of the large quartz vein as ~2-3 mm thick aggregates of white mica, chlorite, rutile, and tourmaline (Figure 22e). In EV6c, the assemblage is a bit weak, but it does exist as vein-like aggregates of white mica (Figure 20e), small tourmaline grains averaging ~20 μm in size, as well as microcline with

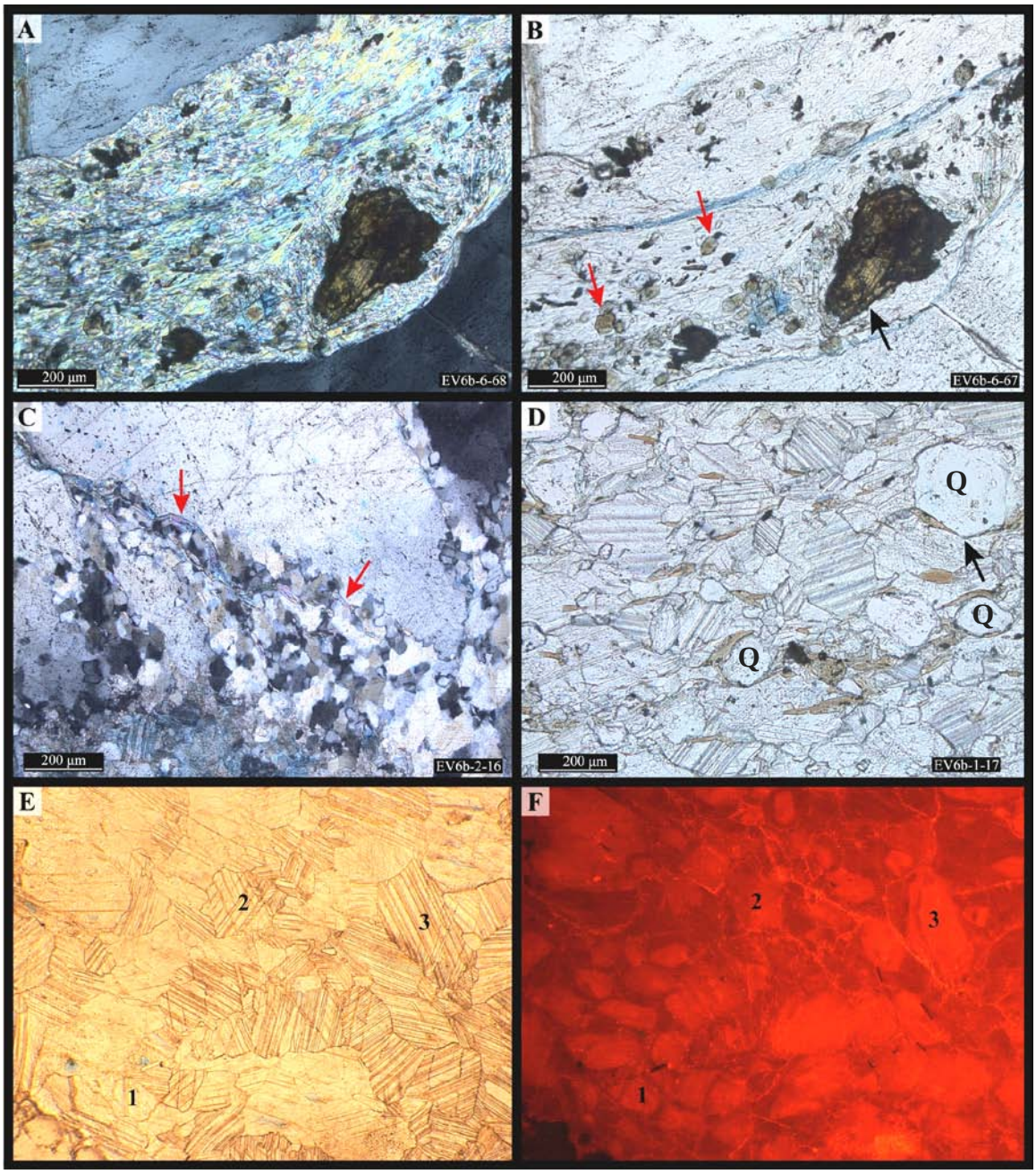


Figure 21. Photomicrographs of South Summit samples; B, D and E are in PPL; F is a CL image. A) A wide fracture through the large quartz vein in EV6b is filled exclusively with metasomatic minerals. B) Same photo as A; red arrows point to tourmaline grains and the black arrow to a large rutile grain. C) Dynamic recrystallization of the quartz vein in EV6b forming a core-mantle structure; red arrows point to white mica grains. D) Static growth of matrix calcite (generally twinned) and quartz grains (Q); brown grains are biotite; arrow points to a quartz grain with a ring of inclusions that denotes a former grain boundary. E) Same image as F; numbers are for reference with F. F) CL image of statically recrystallized calcite, as seen by the core-overgrowth structures.

diagnostic tartan twins. The secondary assemblage is best exhibited in sample EV6b where it is primarily comprised of white mica, chlorite, biotite, rutile, and grains of tourmaline averaging ~43 μm in size (Figure 21a and 21b). These phases may fill fractures in the large quartz vein or may be disseminated throughout the matrix. White mica and chlorite commonly form elongate, foliation-parallel aggregates within the matrix and rutile and tourmaline always occur within these aggregates (Figures 20a, 20d and 22c). The margins of the aggregates may be well-defined or diffuse, and both chlorite and white mica also occur within the matrix as individual grains parallel to foliation. Individual grains of white mica, chlorite and biotite in the matrix appear to have precipitated from interstitial fluid that percolated into micro-voids (Figures 21d, 22a and 22d). Swarms of aligned biotite grains frequently occur within the matrix proximal to the aggregates of white mica and chlorite, but they do not appear to be a part of the aggregates themselves. This is interpreted as evidence that biotite has been derived from a continuous reaction between chlorite and muscovite (Winter, 2001), rather than crystallizing directly from metasomatic fluids.

Where biotite precipitated in the matrix, tourmaline and albite are commonly associated with it. In Figure 21d is a large quartz grain in the upper right (arrow) with a ring of inclusions that denotes this grains former boundary. Outward from this ring is an overgrowth that has produced well-defined, straight crystal faces that pinched a biotite grain as the crystal grew (arrow). In the same photo there are also signs for static growth of calcite, such as polygonal grains with clean crystal faces that often pinch-out the biotites which nucleated interstitially. Further evidence that matrix grains have grown statically is seen in CL images which show nearly equi-dimensional core-overgrowth

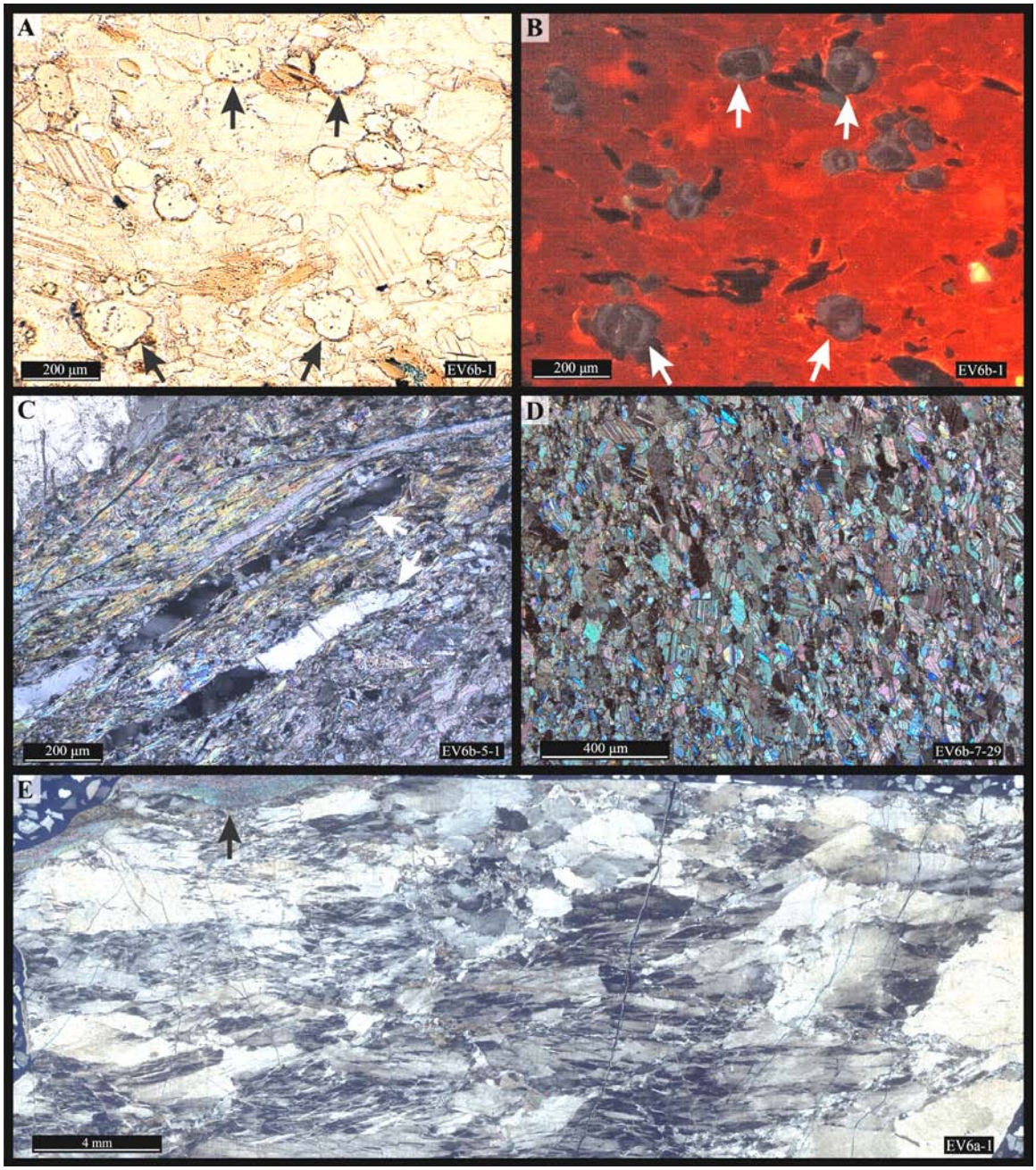


Figure 22. Photomicrographs of South Summit samples; A is in PPL; B is a CL image. A) Photo of matrix quartz grains (arrows) which have statically grown in response to hot metasomatic fluids which the biotites (brown grains) crystallized from. B) CL image of the same photo in A; quartz grains reveal bluish overgrowths. C) Matrix photo showing abundant white mica (yellow grains) as well as ribbon quartz (white arrows). D) Characteristic marble texture displayed throughout the matrix of EV6b; notice the blue, foliation-parallel mica grains. E) Thin section scan of sample EV6a showing well-developed prismatic subgrains in the deformed quartz vein that comprises this sample; on the side of the vein are aggregates of metasomatic phases (arrow).

structures on many quartz and calcite grains (Figures 21e, 21f, 22a and 22b). What is especially striking about most of the quartz overgrowths is that cores are typically gray-black in color and the overgrowths are a bluish shade that grades to gray-black toward the rim. Under CL, authigenic quartz that has formed diagenetically will appear gray-black, and blue shades (415 nm) in quartz indicate elevated concentrations of titanium (Rusk et al., 2006). This is because Ti^{4+} substitutes for Si^{4+} on fourfold tetrahedral sites in quartz, and the solubility of Ti in quartz increases with increasing temperature (Wark and Watson, 2006; Thomas et al., 2010); therefore, Ti concentration increases as a function of temperature. Conveniently, increasing the concentration of Ti also increases the degree of blue luminescence, thereby providing a relative indication of temperature at which the grain equilibrated (Spear and Wark, 2009). Thus, the blue overgrowths indicate that static growth of detrital quartz grains occurred at elevated temperatures, which implicates hot fluid as the cause for static recrystallization. The gradational nature in color of the overgrowths, which grade to black toward the rim, suggests decreasing temperature as static growth ensued. This scenario is a trend throughout sample EV6b, which is a relationship between the static growth of calcite and quartz and the occurrence of secondary phases, such that the fluid which precipitated these minerals induced growth of matrix grains.

EBSD Analysis

EBSD analysis has been used on the large, plastically deformed quartz vein in sample EV6b (Figure 20a). The fabrics displayed in this vein include thin-section-scale prismatic subgrains (Figure 20a) and zones of recrystallized grains (Figure 21c and 23a).

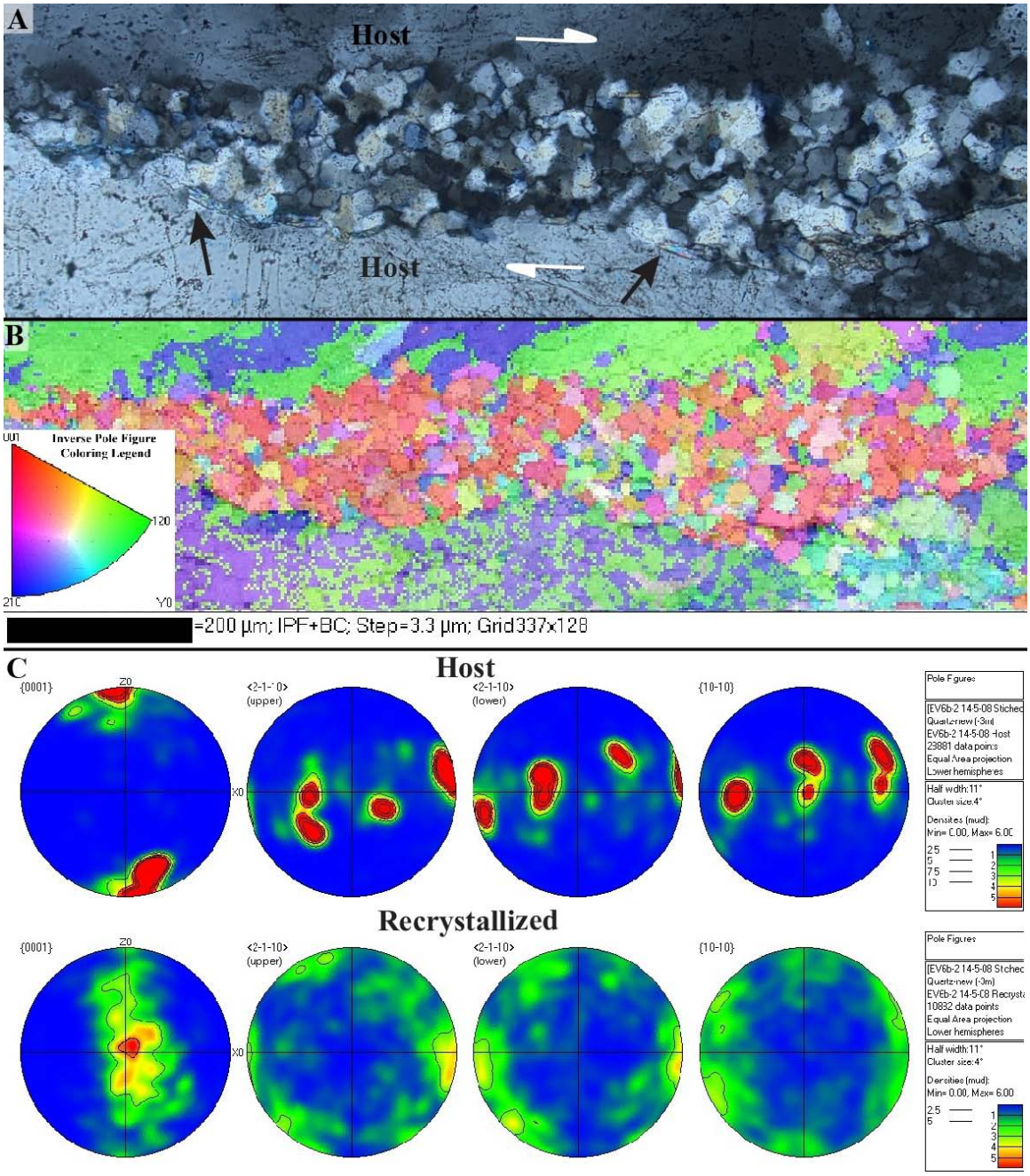


Figure 23. EBSD orientation data for one analysis on sample EV6b; this analysis indexed ~78%. A) XPL photomicrograph showing the recrystallized zone analyzed; arrows point to small laths of metasomatic mica that rim the zone of recrystallized grains suggesting that hot metasomatic fluid may have caused the localized recrystallization. B) Pole figures for host grain orientation. C) Pole figures for the recrystallized grains which show there is a LPO, that formed from dominant prism <a> slip with some contribution of rhomb <a> slip (Figure 10); prism <a> slip occurs at 400-500°C in quartz (Stipp et al., 2002*a*).

The large prismatic subgrains are quite spectacularly developed, but the scale of these structures precludes a pragmatic use of EBSD analysis. Instead, smaller scale recrystallization fabrics within this vein were the focus of EBSD analysis. These recrystallized zones are often lenticular bands that are bordered by relatively undeformed portions of the original vein material, referred to as *host* material (Figure 21c and 23a). By mapping the orientation of the recrystallized grains and the host material, it has been possible to determine what slip system(s) were activated during recrystallization. This, in turn, has provided constraint on temperatures during recrystallization.

In Figure 23 is a complete orientation data set from a single analysis of an elongate zone of recrystallized grains occurring within the large quartz vein in sample EV6b. Pole figures show that the recrystallized grains have a new, unique orientation relative to the host from which they recrystallized. The clustering of data points in the center of the c-axis pole figure {0001} is an LPO pattern that forms from dominant prism <a> slip in quartz (Figure 10; Passchier and Trouw, 2005), which occurs between 400-500ºC (Stipp et al., 2002*a*). This c-axis maxima is not perfectly defined at the center of the figure and the points that plot slightly outward from the center indicate there was a component of rhomb <a> slip involved as well. At these temperatures the dominant dynamic recrystallization mechanism is subgrain rotation recrystallization (SGR; Lloyd and Freeman, 1994; Stipp et al., 2002*a*), corresponding to regime II of the three dislocation creep regimes established in an experimental study by Hirth and Tullis (1992).

Results from three other EBSD analyses of similar recrystallization fabrics in the same vein show the activity of prism <a> slip (Figure 24a and 24b), with some inherited

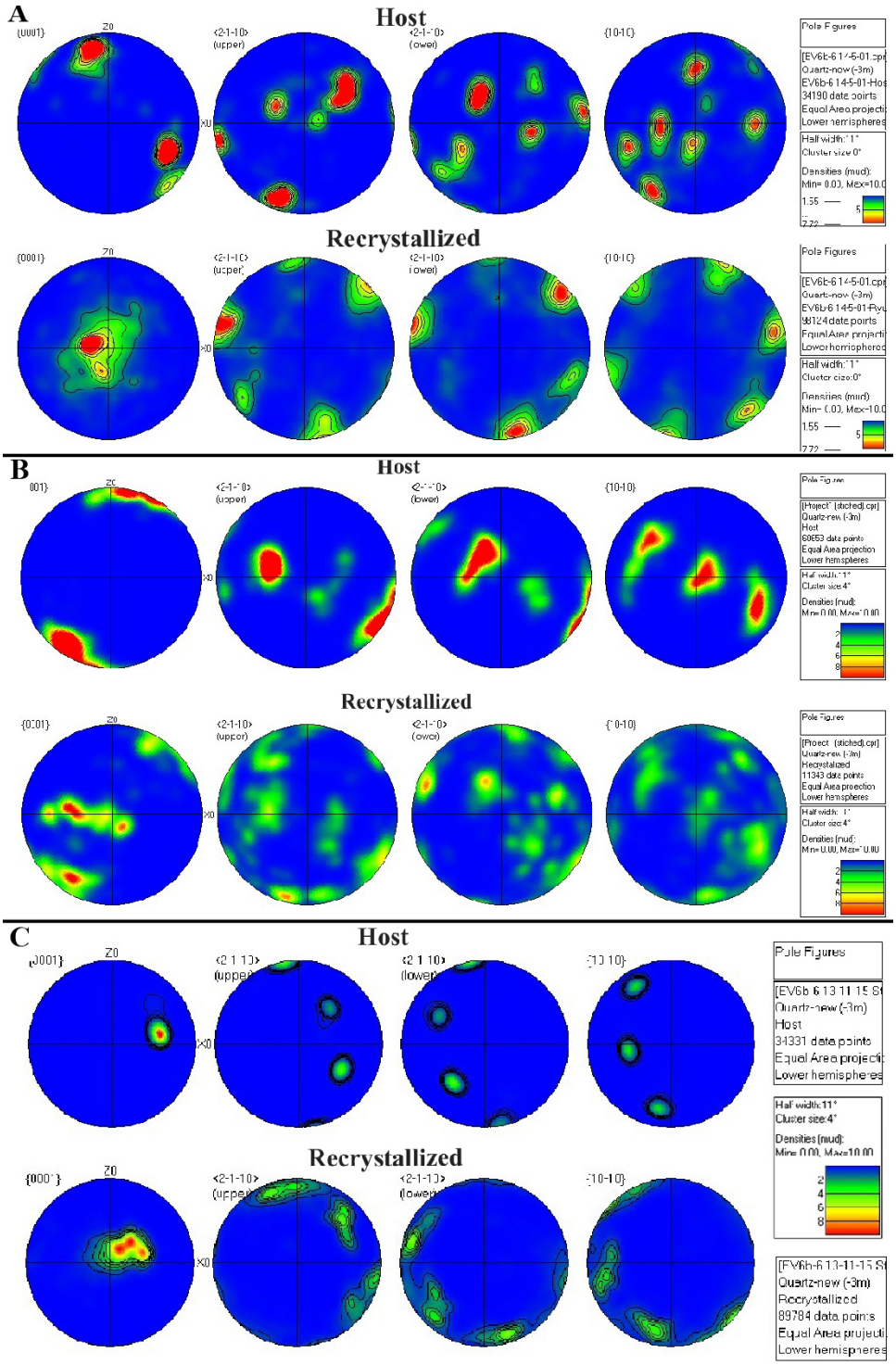


Figure 24. EBSD pole figures for three analyses on EV6b. A) A lattice preferred orientation (LPO) indicative of prism <a> slip. B) An LPO pattern that is indicative of prism <a> slip, but there is some orientation inheritance from the host material. C) LPO pattern, but it is not significantly different from the host; no conclusions have been derived from this analysis.

orientation from the host shown in Figure 24b. The data in Figure 24c may show the activity of prism <a> slip as seen by the slight migration of the maxima in the host {0001} pole figure toward the center of the recrystallized grains {0001} pole figure. But, the data in Figure 24c is not taken as strong evidence for prism <a> slip because overall there is little difference between the orientation of the host and recrystallized grains. With the exception of the analysis shown in Figure 24c, these data indicate that recrystallization of this vein took place through a combination of prism <a> and rhomb <a> slip.

The orientation of the elongate recrystallized zones is the same from one zone to the next and the long axis of these zones parallels the shear plane in the surrounding matrix, suggesting these zones may be related to shearing of the sample. Therefore, the LPOs observed are assumed to have formed in response to strain experienced by the vein during shearing. Also, the recrystallized zones are often bordered by metasomatic mica phases (Figure 21c), suggesting that hot fluids may have been a thermal cause of dynamic recrystallization. The same recrystallization fabrics are displayed in the quartz vein from sample EV6a (Figure 22e), indicating that this sample may have been deformed under similar conditions as EV6b.

Paleostress Calculations

The matrix calcite in South Summit samples does not meet the criteria for paleostress calculations because CL imaging shows strong evidence of static growth in these grains. However, the zones of recrystallized quartz may provide an approximation of stress at the time of recrystallization. Because there is a considerable rheologic

contrast between the matrix and the large quartz vein undergoing recrystallization, these calculations are used with caution. Grain size data from the two analyses with the highest indexing rate, which corresponds to Figures 23 and 24a were used, yielding an average grain size of 16.09 ± 13.31 μm from 3,524 grains measured. Based on microstructural observations, recrystallization is interpreted to have occurred through subgrain rotation (i.e., climb-accommodated dislocation creep) and the constants and formula of Stipp and Tullis (2003), modified after Holyoke and Kronenberg (2010), have been used for climb-accommodated dislocation creep, giving the formula:

$$d = 2451\sigma^{-1.26}$$

Using the average recrystallized grain size for d, solving for σ yields a paleo-differential stress estimate of ~54 MPa, which is significantly smaller than the value obtained from Summit samples. If the mylonitic foliation found in Summit samples is the result of faulting on the Qomolangma detachment, than these results contradict theoretical expectations, as differential stress should increase closer to the detachment. This could imply that the fabric observed in Summit samples is not related to that seen in South Summit samples, which are presumed to have formed from faulting on the Qomolangma detachment. As such, further discussion about the possible implications of these results will be addressed in Chapter 8.

Geochemical Analysis of Tourmaline

Tourmaline minerals have an exceptional stability range because they are able to adjust their composition to suit a wide variety of conditions in terms of pressure, temperature, fluid composition, and host-rock composition (e.g., van Hinsberg et al.,

2011*a* and *b*). The compositional sensitivity of tourmaline, therefore, makes it an excellent petrogenetic indicator mineral of the host environment in which it crystallizes and evolves. Because tourmaline is a major constituent of the metasomatic mineral assemblage found in South Summit samples, it has been used in this study to trace the origin of metasomatic fluids.

All tourmaline grains observed are euhedral with pristine crystal boundaries, and are typically littered with mineral inclusions, though they do not have a detrital core (Figures 12, 21a and 21b). Two electron microprobe grain-transects and two single spot analyses were collected from four different tourmaline grains in sample EV6b. The structural formula calculated from the averaged chemical composition data of 16 electron microprobe data sets shows that dravite is the species of tourmaline present:

$$(Na_{.67}Ca_{.06}K_{.01}Xvac_{.26})(Mg_{1.7}Fe_{.85}Al_{.34}Ti_{.06})Al_6(Si_{5.82}Al_{.18}O_{18})(BO_3)_3(OH)_4$$

Chemical composition data plotted on the variation diagrams presented in Figure 25 show that all spot analyses, except one, plot as dravite. As previously discussed, tourmaline has significant compositional sensitivity to the environment under which it evolves (van Hinsberg et al., 2011*a* and *b*). Therefore, if multiple influxes of boron-rich metasomatic fluid occurred, a “memory” of this event would be recorded in tourmaline grains as growth zones. The composition data from transects across two tourmaline grains from the South Summit (Figure 12) show an absence of growth zones and a complete lack of any meaningful chemical variation from core-to-rim (Appendix B), indicating that metasomatic minerals crystallized during a single event under relatively homogenous chemical conditions (Henry and Dutrow, 1996; van Hinsberg et al., 2011*a*).

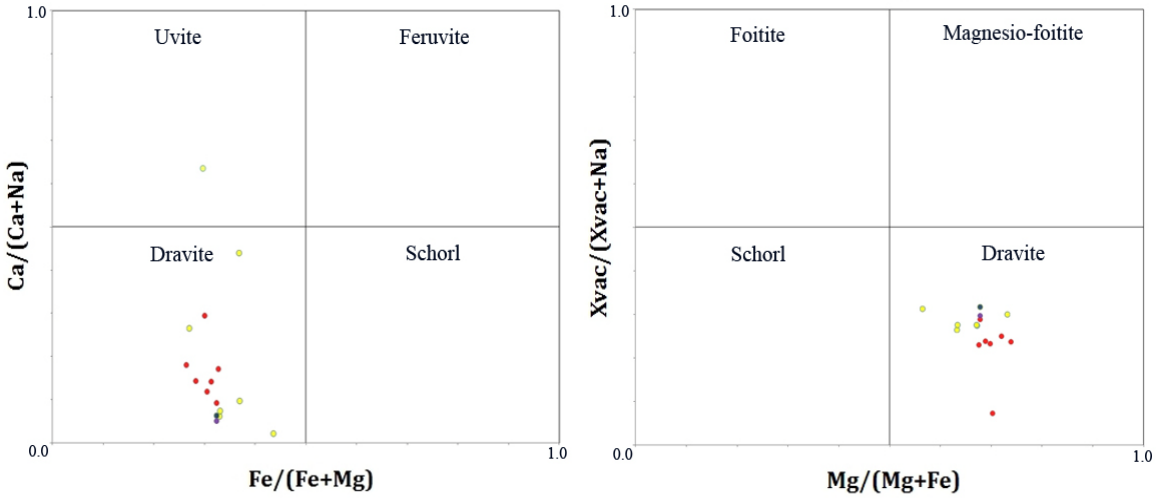


Figure 25. Chemical systematics of tourmaline in the Mg-Fe^{2+}-Ca-X_{vac} subsystem, plotting chemical composition data of tourmalines in South Summit samples. Xvac = X-site vacancy; see Figure 11.

Metasomatism and the Significance of Dravitic Tourmaline

Dravite is a type of tourmaline commonly found in metasomatically altered carbonate rocks in contact metamorphic zones around granitic bodies (Henry and Dutrow, 1996; Nesse, 2011). The occurrence of dravite in South Summit samples is interpreted to be a result of metasomatism associated with the emplacement of leucogranite sills and dikes into pelitic rocks of the North Col Formation, subjacent to the summit limestone. This interpretation has important implications to the current tectonometamorphic model established for the Everest region. As such, some of the fundamental systematics for tourmaline formation, as well as the range of possible scenarios that could produce dravitic tourmaline in the Qomolangma Formation, are discussed below.

Boron Sequestration and the Formation of Tourmaline. The formation of tourmaline relies on the availability of boron, either intrinsically (closed system) from boron-hosting minerals contained locally in the rock system prior to tourmaline formation, or extrinsically (open system) from boron brought into the system from an external source (i.e., metasomatically; Dietrich, 1985; Henry and Dutrow, 1996; van Hinsberg et al., 2011*a*). Tourmaline contains 33,000-34,000 ppm boron (Henry and Dutrow, 1996, p. 531) and it is a ubiquitous borosilicate mineral that can form in a wide range of settings, but it is most commonly found in and around granitic melts and their associated hydrothermal systems, and in medium- to high-grade metamorphic rocks of pelitic composition (Morgan and London, 1987; Grew, 1996; London et al., 1996); though tourmaline can also develop at diagenetic to low-grade metamorphic conditions (Dutrow and Henry, 2011; Henry and Dutrow, 2012). Boron is a trace constituent in the crust and its availability for the precipitation of tourmaline relies on geochemical processes to concentrate it (Henry and Dutrow, 1996). Boron is strongly partitioned into the fluid phase at relatively low temperature >150°C (Leeman and Sisson, 1996), and precipitation of tourmaline occurs once a minimum boron content in the fluid is reached and favorable bulk compositions are encountered, usually where Fe, Mg, and Al are abundant. The sequestration of boron into newly formed tourmaline grains is dependent on hydrothermal fluids, which act as a critical dispersive and concentrating mechanism for boron in both the igneous and metamorphic settings (Leeman and Sisson, 1996). Tourmaline associated with granitic systems is usually derived from boron-rich, late-stage hydrothermal solutions that are expelled into the surrounding country rock from

well-fractionated melts (Morgan and London, 1987; London et al., 1996, London, 1999), forming moderate to large amounts of tourmaline where sufficient Fe, Mg, and Al are present in the country rock (Slack, 2002). Boron may also be derived intrinsically from the breakdown of boron-bearing minerals during metamorphism (Henry and Dutrow, 1996), such as for a calcareous shale, a significant amount of boron will be released during the breakdown of clays, which are the most important seat of boron in shale (Harder, 1970).

The possible origins for tourmaline grains within the Qomolangma Formation include: (1) a detrital origin; formed diagenetically as authigenic tourmaline; (2) through metamorphism and the breakdown of boron rich minerals within the Qomolangma Formation (e.g., clays); or (3) from metasomatism associated with an invasive hydrothermal fluid. With the exception of a detrital origin, the setting for these scenarios is either an open or closed system, which implies whether boron was sourced intrinsically or extrinsically. Diagenetic tourmaline and tourmaline formed from the breakdown of clay within the Qomolangma Formation would have an intrinsic boron source, while tourmaline formed from an invasive hydrothermal fluid would have an external boron source. Each origin is considered in more detail below.

Origin: Detrital. A detrital origin for tourmaline grains in the Qomolangma Formation is unlikely for the following two reasons: (1) Tourmaline is only found in South Summit samples, occurring in high concentrations within veins and aggregates of muscovite, chlorite, and biotite, with a notable lack of tourmaline within the matrix. For tourmaline grains incorporated penecontemporaneously in the Qomolangma Formation,

one would expect tourmaline to be distributed throughout the formation, rather than heavily concentrated in one zone. (2) Optically, tourmaline grains in South Summit samples are euhedral and show no sign of rounding. Though tourmaline is very resistant to weathering, the absence of any sign of mechanical transport suggests that these grains do not have a detrital origin.

Origin: Intrinsic Boron Source. For a closed-system, the precipitation of tourmaline in limestone requires the liberation of boron from clay, which is the dominant seat of boron in carbonate rocks (Lerman, 1966; Harder, 1970; Couch and Grim, 1986; Grew, 1996). Illite, the most abundant clay mineral in limestone prior to the Late Mississippian (Weaver, 1959), contains 100-2,000 ppm boron and it can serve as an intrinsic boron source during metamorphism (Henry and Dutrow, 1996, p. 531). In a study of boron in carbonate rocks, Reynolds (1965) noted that under greenschist facies metamorphism, the polytypic transformation of illite to its higher temperature 2M polymorph caused boron to release from the crystal lattice, resulting in the crystallization of dravitic tourmaline grains throughout the rock matrix, each with a small detrital tourmaline nucleus.

The composition, morphology, and nature of occurrence of the tourmaline grains found in South Summit samples preclude the possibility of a closed-system origin. As previously mentioned, tourmaline found in South Summit samples is almost exclusively associated within veins and aggregates of other secondary phases, and such locally high concentrations of tourmaline in a rock is a common feature of tourmalinization by way of an infiltrating external fluid (Henry and Dutrow, 1996). The tourmaline grains are also

unzoned, chemically homogeneous, and lack a detrital tourmaline nucleus, suggesting that precipitation occurred all at once from a large influx of boron-enriched hydrothermal fluid (Dutrow et al., 1989); in a closed system environment tourmalines often have zoning, reflecting the episodic nature of intrinsic boron release (Henry and Dutrow, 2012). It is possible, and quite common, to have diagenetic tourmaline without a detrital tourmaline nucleus in carbonate rocks, but such occurrences are generally the X-site-vacant foitite or magnesio-foitite species (Henry et al., 1994; Rosenberg and Foit, 2006). While it is unlikely that boron was sourced exclusively from within the Qomolangma Formation, it is possible, however, that the release of boron from clay minerals did occur, augmenting the concentration of boron in aqueous solution and facilitating the sequestering of boron into tourmaline during a large external influx of boron rich fluid.

Origin: Extrinsic Boron Source. Felsic granitic magmas that have undergone significant fractionation are enriched in boron because boron behaves incompatibly in igneous systems (Morgan and London; 1987; London et al., 1996). Therefore, tourmaline commonly forms late in the crystallization history of the magma, when concentrations of boron and water are very high. However, because of the low Fe and Mg content in many felsic magmas, they are not able to conserve boron as tourmaline and consequently, boron may be lost from the magma into the wall-rock as a late stage hydrothermal fluid that is heavily enriched in boron. A significant amount of boron can be retained within the wallrock as tourmaline, if the wallrock interacting with the fluid contains a sufficient amount of Mg, Fe and Al (Morgan and London, 1987; London et al., 1996). The extent that an invasive magmatic fluid may permeate into country rock is

highly variable; the contact aureole may reach a few meters to a few kilometers, and the envelope of tourmalinization can be just as variable (London et al., 1996). At the Larderello geothermal field in Italy, Cavarretta and Puxeddu (1990) showed that boron metasomatism associated with a large granitic intrusion can be far reaching, and well logs from the area showed the occurrence of metasomatic tourmaline in country rock at ~600 meters above the inferred wallrock-granite contact. These tourmalines were consistently dravitic, while those close to the contact had a composition similar to the granitic source, indicating the increasing influence that the wall rock has on the composition of hydrothermal fluid and the species of tourmaline precipitated.

In the Everest region and throughout the Himalaya, it is well established that the upper structural levels of the Greater Himalayan Sequence are heavily injected with leucogranite sills, dikes and plutons (Le Fort et al., 1987; Searle, 1999*b*; Searle et al., 2009). However, due to the relative inaccessibility and widespread cover of snow and glacial ice, the vertical extent of leucogranite bodies on Everest is not completely understood. Recent, high resolution photos viewable on *glacierworks.org* and photos taken from helicopter provided by Simon Moro and Max Lowe, have been used in this study to reinterpret the spatial distribution of leucogranite on the Everest massif. These images show leucogranite bodies injected well into the Everest Series schists up to ~7,600 meters on the southwest face of Everest (Figure 26), as well as dykes as high as the summit of Nuptse (7,879 meters) and a large swarm of dikes and sills on the south face of Changtse that reaches nearly to the Yellow Band (Figure 6d). These observations suggest that leucogranites extend above the Lhotse detachment and are not restricted to its footwall, as previously thought (e.g., Searle, 1999). There are other areas where the



Figure 26. Southwest face of Everest, from the summit at 8,850 meters down to camp II at 6,500 meters in the Western Cwm. The large leucogranite body (Lg) at the base of the southwest face is the Everest granite (*c*. 21 Ma; Simpson et al., 2000). Notice the dikes (Lgd) running from lower right to upper left, these reach up to ~7,600 meters on the west ridge. White hash marks indicate the dip of bedding. Photo: Max Lowe.

STD is comprised of superposed faults, as on Everest, and in these locations the lower detachment(s) is often crosscut by leucogranites (e.g., Leloup et al., 2010); thus, it is not surprising that the Lhotse detachment is crosscut on Everest. These observations imply that for leucogranite-associated fluid to have reached the South Summit (8,750 meters), it needed to travel a maximum vertical distance of just over a kilometer. However, this number could be significantly reduced if unexposed leucogranite bodies within the massif have a higher vertical extent than those that are exposed.

As discussed in Chapter 3, leucogranites in the Everest region are well-fractionated, peraluminous, felsic granite bodies (Le Fort et al., 1987; Guillot and Le Fort, 1995; Visonà and Lombardo, 2002). Although tourmaline is present in Himalayan leucogranites, due to their alkaline nature these melts do not efficiently preserve boron as tourmaline, often expelling late-stage boron-rich fluids into the country rock. Upon intrusion into the Everest Series pelites, contact metamorphism and associated metasomatism could have resulted in further boron enrichment from the breakdown of muscovite and chlorite, both of which are significant seats of boron in pelitic compositions (Henry and Dutrow, 1996 and references therein). By the time metasomatic fluid reached the Qomolangma Formation, its geochemical signature would have been flush with boron and presumably with other requisite elements for stabilizing dravitic tourmaline (Mg and Al), derived from the Everest Series pelites. Furthermore, the South Summit tourmalines are very similar in character and style of occurrence to those described in a study by Dutrow et al. (1989), where extensive fluid infiltration, sourced from a nearby granitic pluton, caused anomalously high concentrations of

unzoned, chemically homogenous tourmaline grains around muscovite-rich pseudomorphs.

Titanium-in-Biotite Geothermometry

For the Ti-in-biotite geothermometer to be reliable the mineral assemblage must be similar to that of calibration samples used by Henry and Guidotti (2002), and it needs to have been equilibrated between ~3-6 kbar. Minerals a part of the secondary assemblage in South Summit samples that are of proper chemical character include quartz, chlorite, rutile and muscovite. However, determining that biotite grains have reached chemical equilibrium with a certain set of minerals is difficult. But, as pointed out by Henry et al. (2005), the degree of homogeneity in Ti content of biotite grains can be used to evaluate the attainment and extent of chemical equilibrium or disequilibrium. Microprobe data show that the Ti concentration in biotite grains used in this study is quite consistent (Table 2; Appendix B), demonstrating that the assemblage may have reached equilibrium. It is interpreted here that equilibration of the secondary phases occurred in the Early Miocene, during leucogranite emplacement associated with Neohimalayan metamorphism. Neohimalayan pressure estimates from other studies have been calculated for footwall rocks and results from near Everest at Hermit's gorge (down-dip) yielded 4.6 kbar (Hodges et al., 1992), and a float sample from the Everest Series collected ~6 km south of Everest at the base of the south face of Nuptse (up-dip) yielded 2.9 kbar (Jessup et al., 2008). Because there is strong evidence for post-Neohimalayan movement on the South Tibetan Detachment in the Everest region until *c*. 11-13 Ma (Leloup et al., 2010; Cottle et al., 2011), the up-dip value is a more representative

estimate of footwall rocks that were immediately below the Qomolangma Formation at the time of metasomatism. Therefore, 2.9 kbar is taken as a maximum estimate of pressure at the South Summit at the time equilibration occurred. If we assume that at the time of equilibration the South Summit was positioned structurally above the location where this float sample originated, this value can be further refined to between 1.77-2.55 kbar by doing a partial restoration of the Qomolangma detachment using ~6 km heave, a constant dip of 10º for the Qomolangma detachment, a calculated throw of ~1 km, the range of elevations for the float sample source (~5,800 - 8,500 meters; Jessup et al., 2008), and using a pressure gradient of 3.5 km $kbar^{-1}$ (gradient used in other South Tibetan Detachment restorations; e.g., Searle et al., 2003).

Of the 22 electron microprobe data sets, the 12 best analyses (and the most appropriate for Ti-in-biotite geothermometry) were selected for temperature calculations. The composition of the selected data sets and their averaged composition are presented in Table 2, as well as the temperature calculated from the averaged composition. The calculated temperature is 603ºC, which is interpreted as peak metamorphic conditions at the time of metasomatism. This temperature may be slightly inflated due to the expected low pressure conditions under which the metasomatic phases equilibrated. Still, using these data conservatively, it is concluded that metamorphism at the South Summit reached as high as ~500ºC. The electron microprobe transects of tourmaline grains do not show any growth zoning or compositional variations from core-to-rim, indicating metasomatism was a single-phase event that occurred under relatively homogeneous conditions (Henry and Dutrow, 1996; van Hinsberg et al., 2011*a*). Also, there is no evidence for a later phase of deformation or metamorphism that could have re-

Electron Microprobe Data: Biotite

Analysis Point	195	196	197	198	199	200	201	202	203	211	212	213
SiO2	35.79	35.13	36.42	35.92	36.63	36.57	37.80	36.20	36.64	36.53	36.78	36.50
TiO2	1.65	1.45	1.70	1.50	1.67	1.82	1.77	1.75	1.74	1.71	1.61	1.49
Al2O3	18.12	18.47	17.99	18.14	17.94	17.95	17.96	17.70	18.08	17.01	17.72	18.14
FeO	17.03	17.63	17.12	16.90	16.95	17.03	16.75	16.51	16.81	17.01	17.14	16.74
MnO	0.00	-0.02	0.02	-0.01	0.05	0.00	0.06	-0.03	0.04	0.02	0.01	0.02
MgO	11.89	12.30	11.80	11.84	12.17	11.91	11.21	11.43	11.83	11.83	11.65	11.72
CaO	0.13	0.12	0.14	0.26	0.39	0.33	0.15	0.17	0.12	0.15	0.17	0.22
Na2O	0.13	0.09	0.06	0.11	0.12	0.15	0.08	0.11	0.13	0.10	0.11	0.05
K2O	8.92	8.14	9.50	9.11	9.05	9.24	9.19	9.20	9.57	9.31	9.52	9.44
Cr2O3	0.05	0.07	0.06	0.04	0.07	0.03	0.13	0.09	0.05	0.05	0.07	0.04
Cl	0.03	0.04	0.03	0.04	0.04	0.01	0.04	0.08	0.03	0.05	0.02	0.04
BaO	0.11	0.14	0.13	0.07	0.00	0.05	0.16	0.07	0.14	0.09	0.14	0.11
F	0.78	0.80	0.83	0.80	0.92	0.88	0.86	0.86	0.83	0.87	0.88	0.87

Analysis Point	214	215	216	217	218	219	220	221	222	223	Avg.	Avg. of Best Analyses
SiO2	36.06	27.08	36.04	36.60	36.07	36.28	36.93	36.74	36.69	36.27	36.11	36.48
TiO2	2.12	1.22	1.47	1.71	1.48	1.64	0.61	1.36	1.80	1.79	1.56	1.71
Al2O3	17.88	13.76	18.69	17.81	18.20	18.01	18.35	18.01	17.95	17.99	17.90	17.97
FeO	16.92	14.41	17.09	17.41	17.87	17.01	16.43	16.56	16.82	16.66	16.89	16.92
MnO	0.03	0.03	0.00	-0.02	0.04	-0.02	0.03	-0.03	0.00	0.01	0.01	0.01
MgO	12.05	9.35	11.85	11.93	12.14	11.76	12.97	12.10	11.83	11.83	11.86	11.78
CaO	0.18	8.60	0.37	0.17	0.28	0.17	0.09	0.31	0.11	0.06	0.47	0.18
Na2O	0.09	0.12	0.14	0.16	0.12	0.12	0.09	0.11	0.14	0.11	0.11	0.12
K2O	8.43	7.17	8.18	9.20	8.39	9.23	9.48	9.53	9.44	9.48	9.05	9.26
Cr2O3	0.09	0.07	0.12	0.05	0.03	0.04	0.01	0.06	0.02	0.05	0.06	0.06
Cl	0.07	0.07	0.09	0.04	0.03	0.08	0.06	0.04	0.04	0.01	0.04	0.04
BaO	0.08	0.05	0.04	0.13	0.12	0.04	0.02	0.01	0.11	0.16	0.09	0.10
F	0.78	1.00	0.82	0.90	0.88	0.90	1.02	0.98	0.88	0.86	0.88	0.86
												Avg. Temp
												603°C

Analysis point	195	196	197	198	199	200	201	202	203	211	212
Temp.	597	570	601	577	598	614	603	609	606	605	588

Analysis point	213	214	215	216	217	218	219	220	221	222	223
Temp.	574	644	565	571	601	570	595	199	557	612	613

Table 2. Chemical composition data of biotites used for Ti-in-biotite geothermometry. The 12 best analyses (highlighted in blue) were averaged and then used for thermometry calculation. These analyses were selected with help from Darrell Henry at Louisiana State University.

equilibrated the secondary phases and, therefore, the temperature calculated using the Ti-in-biotite geothermometer is taken as a reliable estimate of temperature at the time of metamorphism.

Titanium-in-Quartz Geothermometry (TitaniQ)

TitaniQ geothermometry has been used on the large quartz veins found in samples EV6a and EV6b (Figure 20a and 22e). As discussed in the previous section, Ti-in-biotite geothermometry produced temperature estimates of at least ~500°C for metamorphism at the South Summit, for sample EV6b. Due to the similarity in fabrics, the EV6a quartz vein is interpreted to have been deformed under similar conditions and TitaniQ geothermometry of sample EV6a provides evidence to support or refute this assumption. Since recrystallization of these large quartz veins is interpreted to have occurred during metamorphism associated with metasomatism, the pressure would be the same as discussed in the previous section on Ti-in-biotite geothermometry. Therefore, all calculations were done using an estimated pressure value of 2.25 kbar. All electron microprobe data and electron microprobe operating conditions are given in Appendix C, and the averaged data is presented here (Table 3).

Due to sample charging during microprobe analysis, data for sample EV6a is limited to three spot analyses, which yield an average temperature of 558°C (Table 3). This temperature estimate matches nicely with estimates for EV6b obtained using EBSD analysis and Ti-in-biotite geothermometry, suggesting that metamorphism and deformation of sample EV6a did in fact occur under similar conditions as EV6b. The microprobe data for the EV6b quartz vein is more robust and consists of 32 electron

Averaged EMP data for EV6a quartz vein

	Weight%	Norm Weight%	Atomic%	Ti Oxide ppm	Pure Ti ppm	Det.Lim ppm	StdDev wt%
	0.013500	0.10	0.005667	80.23	135.00	15.00	0.001300
Si	46.7	46.7	33.34	**Temperature calculated from averaged Ti concentration = 558.11°C**			
O	53.2	53.2	66.66				
Total	99.91	100	100				

Averaged EMP data for EV6b quartz vein *proximal* to metasomatic phases

	Weight%	Norm Weight%	Atomic%	Ti Oxide ppm	Pure Ti ppm	Det.Lim ppm	StdDev wt%
	0.022433	0.10	0.0094	133.29	224.30	15.50	0.00136667
Si	46.7	46.7	33.33387	**Temperature calculated from averaged Ti concentration = 605.65°C**			
O	53.2	53.2	66.65678				
Total	99.92247	100	100				

Averaged EMP data for EV6b quartz vein *distal* to metasomatic phases

	Weight%	Norm Weight%	Atomic%	Ti Oxide ppm	Pure Ti ppm	Det.Lim ppm	StdDev wt%
	0.002391	0.10	0.001009	14.21	23.91	15.45	0.001300
Si	46.7	46.7	33.33666	**Temperature calculated from averaged Ti concentration = 428.68°C**			
O	53.2	53.2	66.66236				
Total	99.9024	100	100				

Table 3. Averaged electron microprobe (EMP) data for the large quartz veins in sample EV6a and EV6b, as well as the temperatures calculated using TitaniQ geothermometry. Data from sample EV6b has been divided into two groups which correspond to different locations of the vein where data was acquired (i.e., *distal* or *proximal* to metasomatic phases). Temperatures calculated from data collected at locations proximal to metasomatic phases is clearly much higher than temperatures calculated from data acquired distal to metasomatic phases.

microprobe data sets. Of these data sets, 18 were used for TitaniQ geothermometry and the rest were omitted due to Ti concentrations below the electron microprobe detection limit of ~15 ppm. The temperature calculations produced from this data show a strong

correlation with the location where composition data was gathered from the vein, such that spot analyses for locations proximal to aggregates of metasomatic phases produce higher temperatures compared with those acquired distal to metasomatic minerals and closer to the core of the vein. Consequently, these data have been divided into spot analyses acquired *proximal* to metasomatic phases and analyses acquired *distal* to metasomatic phases (Table 3). Results for locations proximal to metasomatic minerals yield an average temperature of 606°C, whereas the distal locations yield an average temperature of 429°C. The contrast in temperatures presented here shows that Ti exchange and equilibration is not homogenous across the vein, and that Ti concentrations are elevated for parts of the vein close to metasomatic minerals. This is interpreted as additional evidence that hot metasomatic fluids promoted localized recrystallization of the large quartz vein in sample EV6b and presumably EV6a, which has large aggregates of metasomatic phases on either side of the quartz vein analyzed (Figure 27a and 27c). The most important part of the data offered by TitaniQ thermometry is the temperature constraint provided for sample EV6a, as it is the only quantifiable geothermometry data for this sample. Adding these findings to what has already been presented for the South Summit shows that sample EV6a has also undergone metamorphism at temperatures as high as ~550°C.

$^{40}Ar/^{39}Ar$ Geochronology

Results presented thus far have provided evidence that metasomatic fluids, released from Himalayan leucogranites, reached the South Summit, causing localized metamorphism and leading to the precipitation of many secondary phases. In the Everest

area, leucogranite bodies intruded into footwall rocks of the Qomolangma detachment were emplaced episodically throughout the Early Miocene (Simpson et al., 2001; Searle et al., 2003; Viskupic et al., 2005). Therefore, metasomatism of the Qomolangma Formation is expected to have occurred during this time period, and $^{40}Ar/^{39}Ar$ dating of muscovite a part of the metasomatic assemblage has been used to provide more conclusive results for the timing of metasomatism and metamorphism at the base of the Qomolangma Formation (Figure 27).

The results generated during incremental step heating shows a monotonically rising age spectrum spanning from *c*. 18 Ma to *c*. 27.5 Ma (Figure 27e), including several argon gas releases in-between. This is considered complex behavior typical of samples with a non-uniform distribution of radiogenic argon, often produced from the partial loss of ^{40}Ar during a metamorphic event that occurred sometime after initial crystallization (McDougall and Harrison, 1999). For age spectra like this it can be theoretically inferred that the initial low temperature gas release, corresponding to 18 Ma, represents the time of metamorphism; whereas the final, high-temperature argon release corresponding to 27.5 Ma, represents the time that the muscovite originally crystallized (McDougall and Harrison, 1999; Faure and Mensing, 2005). However, this interpretation is purely theoretical and cannot be proven conclusively in this study. The age spectra generated may also reflect a mixed signal produced from other potassium-bearing phases in the sample, which would release different argon gas fractions at different temperatures. For such spectra, gas fraction ratios (e.g., K/Ca, Ca/K, Cl/K, etc.) released at each step can be used to determine if argon was released from other mineral phases. In this study, the aggregate from which the muscovite was extracted does in fact contain other phases such

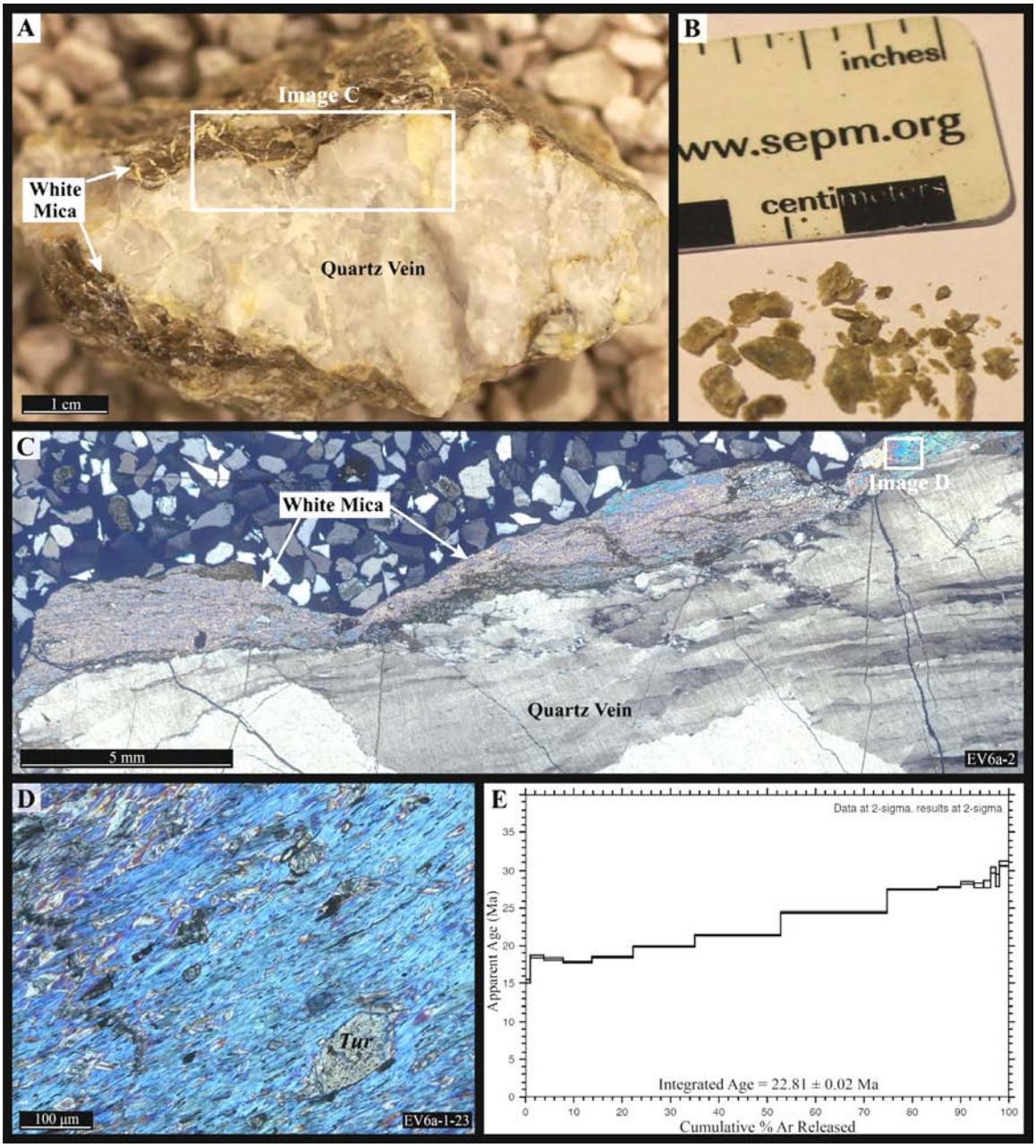


Figure 27. Pertinent information for $^{40}Ar/^{39}Ar$ geochronology. A) Hand sample photo of EV6a showing the layers of white mica (muscovite) and other secondary phases on either side of the large quartz vein. B) Flakes of muscovite extracted by hand from sample EV6a and used for geochronology. C) Thin section scan of sample EV6a showing the large quartz vein and aggregates of secondary phases. D) Photomicrograph from the same thin section in C showing white mica (blue grains), tourmaline (Tur) and fine-grained rutile seen as high relief grains. E) The $^{40}Ar/^{39}Ar$ age spectra generated from incremental heating.

as chlorite, rutile and tourmaline (Figure 27d); however, these minerals do not contain significant quantities of potassium. Furthermore, auxiliary plots of gas fraction ratios do not show evidence that argon was released from minerals other than muscovite; therefore, the age spectra generated is not a result of mixed phases.

Overall, the geochronologic data could suggest a number of possible scenarios that, unfortunately, cannot be unequivocally interpreted. Although a definitive age is not offered by these data, it can at least be inferred that from the Late Oligocene through the Early Miocene, the base of the Qomolangma Formation experienced some sort of metamorphic event which may have been protracted by pulses of hot metasomatic fluid or by shear heating from episodic movement on the Qomolangma detachment, resulting in partial argon loss. Because the dated mica was extracted from sample EV6a, these data should be used with caution when correlated with results from sample EV6b.

Temporal Relationship Between Metasomatism and Fabric Development

Metasomatic phases consistently occur within fractures of the large quartz vein in sample EV6b (Figure 21a and 21b), referred to here as generation-one fractures. These fractures do not continue through the matrix flow fabric, meaning that ductile flow in the matrix continued after the formation of generation-one fractures. Evidence for post-kinematic-metasomatic brittle deformation is offered by calcite-filled fractures in the large quartz vein that continue into the matrix, crosscutting fabric and aggregates of metasomatic phases (Figure 20a), and are referred to as generation-two fractures. The large quartz vein in EV6b is interpreted to have formed prior to the main phase of fabric

development, such that once ductile flow in the matrix commenced the vein created a perturbation in the flow fabric that caused flow to be deflected around the vein as seen in Figure 28a.

Reference made here to “micas” refers to grains or aggregates of white mica, chlorite and biotite that are a part of the secondary mineral assemblage. Figure 28a is a thin section scan that shows the matrix flow fabric wrapping around the large quartz vein in EV6b, as well as boudinage of the vein (black arrow) indicating a subhorizontal extension direction relative to the image. The vein and large fragments of quartz in the matrix have developed an augen shape in response to shearing and ductile flow in the matrix. Figure 28b was taken within the deforming matrix and the blue-purple and orange aggregate of mica and all individual mica grains in the matrix (also blue or orange) are parallel with foliation, which runs from lower right to upper left. Importantly, all the mica grains in Figure 28b have the same extinction angle, suggesting that these grains crystallized at the same time; this phenomenon also occurs for micas in Figure 22d. A significant amount of metasomatic phases have crystallized in a large stress-shadow to the right of the vein (white arrow), and Figure 28c shows a higher-magnification image of this zone. In contrast to Figure 28b, all of the mica grains shown in 28c have a random orientation because they precipitated where shear stresses were minimized. Together, these images illustrate the close temporal relationship between the crystallization of metasomatic phases and fabric development, and they provide evidence that metasomatism occurred synchronous to fabric development. Also, because the micas are not significantly deformed, it is presumed that these phases and conceivably all metasomatic phases observed, precipitated in the final stages of deformation. Assuming

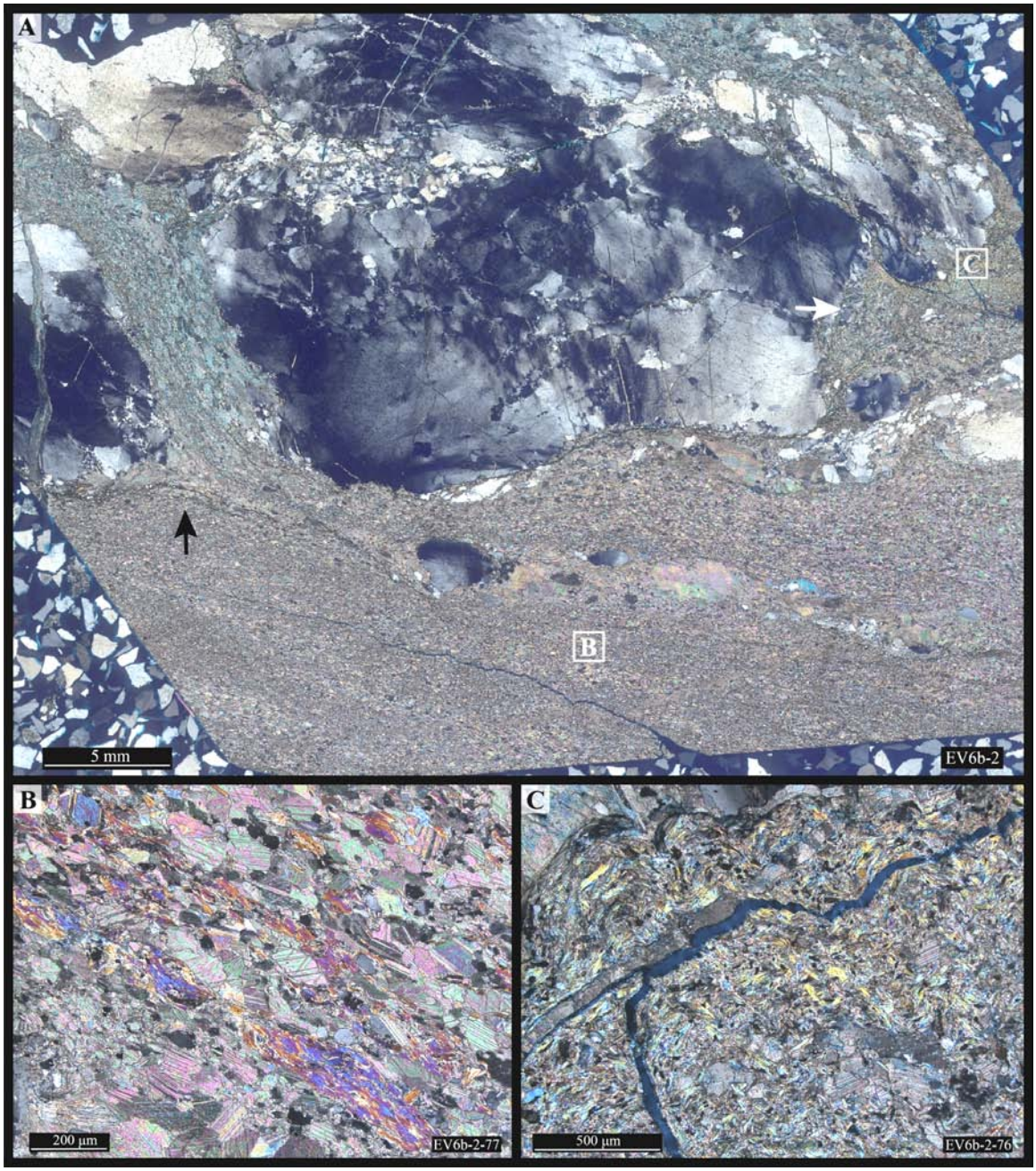


Figure 28. Photomicrographs of South Summit sample EV6b; white squares in A indicate where images B and C were taken. A) Thin section scan showing the large, deformed quartz vein creating a perturbation in the matrix flow fabric. Black arrow points to a portion of the vein undergoing boudinage. The quartz vein creates a stress-shadow on its right side, indicated by the white arrow. B) Photo taken of the matrix showing copious white mica (blue-purple and orange grains), which are parallel to foliation. C) Image taken of the stress shadow on the right side of the large vein. The random orientation of micas here indicates these grains crystallized in the absence of stress.

that the fabric had been developing in response to faulting on the Qomolangma detachment, this implies that metasomatism took place shortly before movement on the detachment ceased. The apparent overlap of these processes is not considered to be a coincidence. Rather, we interpret that metasomatic fluids facilitated faulting by weakening rocks and increasing fluid pressure within and around the fault zone.

Fluid pressures large enough to promote faulting need to approach or exceed lithostatic pressure, known as overpressured fluid, and this commonly results in hydraulic fracturing within the rock body (Gudmundsson, 2011). There are well-defined fractures in the large quartz vein in EV6b that are filled exclusively with metasomatic phases (Figure 21a and 21b) suggesting that fracture propagation or widening of existing fractures may have been facilitated by overpressured fluid. Also, fluids have a major effect on the mechanical properties of minerals, such that minerals are generally weaker in the presence of a fluid (Nakashima et al., 1995; Post and Tullis, 1998; Schenk et al., 2005). Quartz, for example, is ten-times weaker in the presence of water due to the substitution of OH for O in the silicate crystal lattice (called hydrolytic weakening), which strains and weakens the Si-O bonds (Van der Pluijm and Marshak, 2004). Therefore, the presence of fluid in and around the Qomolangma detachment fault zone could have further promoted faulting by weakening rocks. Following a slip event, heat from shearing and any residual heat from metasomatic fluids may have promoted the widespread static recrystallization of calcite and detrital quartz seen throughout the matrix (Figures 21d - 21f, 22a and 22b). This may have also resulted in the intergranular crystallization of micas spread throughout the matrix that are all parallel with foliation (Figure 22d and 28b).

Significance

The data presented in this section shows that metamorphism at the base of the Qomolangma Formation took place at temperatures of 500-600°C and was caused by hot metasomatic fluids. The degree of metamorphism throughout the base of the formation is probably not homogenous because metamorphism would have been localized where metasomatic fluids migrated, thus confining metamorphism to a narrow envelope proximal to the hot fluids. Geochemical analysis of tourmaline provides evidence that metasomatic fluids were derived from Miocene leucogranites injected into rocks subjacent to the Qomolangma Formation (Figure 26). Based on the coarse grains size of calcite and the matrix flow fabric, seen wrapping around the large quartz vein in Figure 28a, sample EV6b is considered a marble mylonite. In contrast, sample EV6c is considered a calc-silicate due to the abundance of quartz throughout the sample, relative to calcite which is present in much lower volume compared to other Qomolangma Formation samples. In fact, this sample could even be interpreted as schist, due to the alignment of mica throughout the sample (Figure 20e). Results discussed thus far may suggest that the Qomolangma detachment on Mount Everest operated under ductile conditions, based on ductile fabrics seen in South Summit samples and the lack of evidence for cataclasis observed in these samples. Also, microstructural observations show that the mineral phases which precipitated from metasomatic fluids are syn-kinematic to fault fabrics, suggesting that metasomatic fluids may have influenced movement on the Qomolangma detachment by (1) increasing fluid pressure, thus reducing effective normal stress on the fault, and (2) weakening rocks proximal to the fault zone, thus reducing effective viscosity and promoting ductile failure.

CHAPTER 7

ENVIRONMENT OF DEPOSITION

The environment of deposition for the Qomolangma Formation is difficult to interpret due to significant deformation and recrystallization that has overprinted the primary fabric. The available evidence is limited to primary constituents preserved in Summit samples that were not destroyed during deformation and metamorphism. These relict constituents include detrital quartz grains averaging ~50 μm in size, crinoid ossicles, relict calcite porphyroclasts up to ~1500 μm in size, and primary saddle dolomite grains. Detrital quartz grains are generally sub-angular to sub-rounded and qualify as very fine sand on average. CL imaging of detrital quartz from Summit and Hillary Step samples shows various shades of blue, indicating elevated concentrations of titanium. Because Ti concentration and the degree of luminescence both increase as a function of temperature (Wark and Watson, 2006), the blue luminescence indicates these grains were sourced from either a plutonic, volcanic, or high-grade metamorphic terrane that was of moderate distance away, based on the degree of rounding in the quartz grains.

The crinoid ossicles found in Summit samples (Figure 29a) are parts of a segmented stalk that supported the crinoid's mouth and crown in the water column for filter feeding (Figure 29b). Crinoids are either benthic or pelagic, or they may have a two-phased life cycle involving both forms; however, the majority of fossil crinoids, especially all Paleozoic crinoids, were stalked forms attached to the seabed (Benton and Harper, 2009). Some fixed crinoids occupy deep-water environments of the continental slope, but the majority of fossils from the Ordovician occupied the shallow water sessile

benthos (Benton and Harper, 2009). As such, crinoid ossicles in Summit samples are interpreted as evidence for a shallow water depositional environment in a zone of good water circulation for filter feeding.

As discussed earlier in this chapter and in Chapter 4, past publications have referred to the Qomolangma Formation as a micritic limestone. There is a vast amount of fine-grained calcite within Summit samples, which could have been mistaken for micrite. However, automated grain size measurements using EBSD analysis, coupled with detailed petrographic observations, have shown these small calcite grains are not micrite, but are dynamically recrystallized grains. Given the absence of micrite and the presence of fossil fragments, as well as what appears to have been coarse grains of calcite cement (spar), the pre-deformed limestone was probably a crinoidal grainstone or boundstone (Dunham, 1962), or a biosparite (Folk, 1962).

Myrow et al. (2009) used stratigraphic correlation with the lower Chiatsun Group in Nyalam, to show that white-weathering beds seen in the Qomolangma Formation are thrombolite beds (Figure 1), clotted organosedimentary structures analogous to stromatolites (Aitken, 1967). Though these structures are not observed in samples used in this investigation, their reported existence within the Qomolangma Formation is very useful for determining the environment of deposition. Thrombolites, like most cryptalgal structures, are restricted to the photic zone, typically intertidal, or subtidal and commonly protected from significant storm reworking by barrier shoals (Flüegel, 2004). In the Early Ordovician carbonate platforms rimmed by barrier reefs were not yet common, and it is inferred that deposition occurred in an environment analogous to the carbonate ramp model described by Ahr (1973). In this model the “ramp” is an inclined (generally < 1°

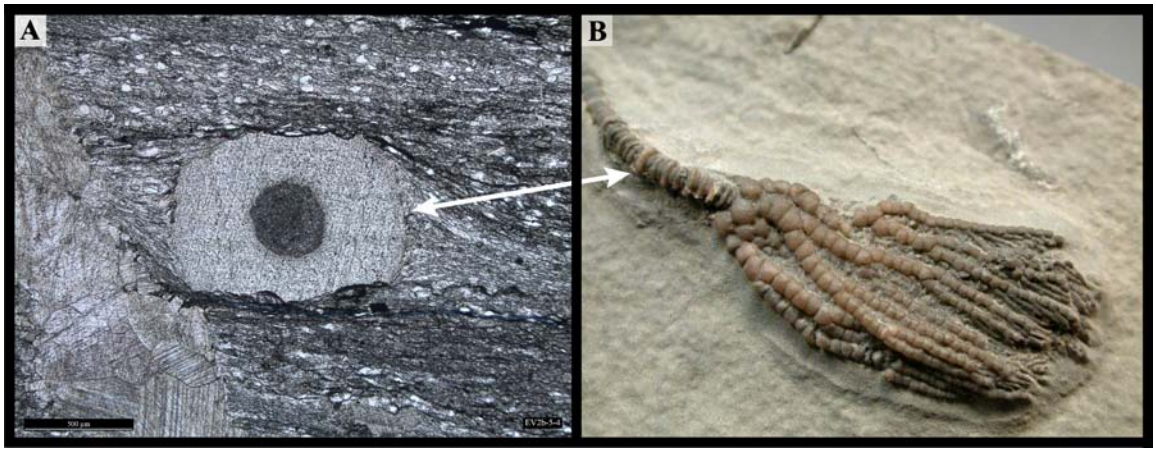


Figure 29. A) Typical crinoid ossicle found in Summit samples. B) Fully preserved crinoid showing how the stalk is comprised of stacked columnals (ossicles).

slope angle) surface, extending basinward without a pronounced break in slope. On a carbonate ramp, grainstones and boundstones typically occur in the shallow, inner portion of the ramp while mudstones and wackestones occur on the seaward reaches of the ramp (Ahr, 1973); therefore, the Qomolangma Formation would have been deposited on the inner-ramp. The repeating thrombolite beds in the Qomolangma Formation as seen in Figure 1, alternate with the darker gray-green sequences of limestone possibly representing a cyclic stratigraphic succession formed from sea level fluctuations. The samples used in this study corresponds to the dark gray-green rock on either side of the thrombolite beds and based on the presence of fossil fragments and the lack of micrite observed, these samples should represent a down-slope shift on the ramp. It is concluded that deposition of the Qomolangma Formation at Everest, occurred on a carbonate ramp that, during small sea level changes, shifted from shallow to slightly deeper water settings on a ramp or wide platform. Primary dolomite grains observed in Summit samples would

have formed penecontemporaneously in a seepage-reflux type dolomitization model, or mesogenetically as cement. Also, this environment could have had a proximal source of terrigenous sediment as indicated by the abundant detrital quartz grains.

CHAPTER 8

DISCUSSION

Interpretation

The fabrics, microstructures and temperature estimates presented for South Summit samples are interpreted to be associated with emplacement of leucogranites and faulting on the Qomolangma detachment, each of which occurred in the Early to Middle Miocene and resulted in deformation and metamorphism at the base of the Qomolangma Formation at temperatures of 500-600ºC. The results presented from Summit samples show that temperatures reached ≥ 250°C during deformation and development of mylonitic foliation; however, these findings have not yet been temporally linked with any tectonic process or metamorphic event. Because paleostress calculations yield higher values for Summit samples than for South Summit samples (126 MPa vs. 54 MPa), it is interpreted that the mylonitic foliation in Summit samples is not a result of faulting on the Qomolangma detachment.

As noted in Chapter 4, fission track data presented by Streule et al. (2012) from a single Summit sample suggests that the top of the Qomolangma Formation had cooled below the apatite fission track closure-temperature (130 ± 30ºC) by the Early Oligocene, at 30.5 ± 5.1 Ma. These data imply that the microstructures and mylonitic fabric seen in Summit samples, presented in this study, were ingrained during a deformational-metamorphic event prior to *c.* 30.5 Ma. As discussed in Chapter 2, the STDS is believed to have reactivated along preexisting thrust faults that formed shortly after collision and

resulted in significant crustal thickening of the Tethyan Sequence by *c.* 30 Ma (Vannay and Hodges, 1996; Searle et al., 2007). In light of this, the well-developed mylonitic foliation and low-grade metamorphism (≥ 250°C) preserved in Summit samples is interpreted to be associated with initial thrust faulting and crustal thickening that occurred shortly after India's collision with Asia.

It is apparent that deformation and metamorphism is not homogeneously distributed throughout the Qomolangma Formation. Certainly, the metamorphic grade observed in South Summit samples is much higher than that observed at the summit, but deformation fabrics related to faulting appear to be dispersed at all structural levels, though they are manifested differently throughout. If the data point of Streule et al. (2012) is accurate, as well as ours, then the geologic scenario presented by these data is defined by the following parameters: temperatures reached 500-600°C at the South Summit during metasomatism in the Early Miocene; the South Summit samples used in our study were collected ~100 meters below the sample dated by Streule et al. (2012); for fission tracks in apatite to be preserved, temperatures must remain below the fission track closure temperature of apatite ~130°C. These parameters imply a temperature difference of ~370°C between the summit and South Summit at the time of metasomatism, or a vertical geothermal gradient of ~3,700 °C km^{-1}. Although the metasomatic fluids that infiltrated the base of the Qomolangma Formation were relatively hot, they likely would not have had the heat capacity to thermally alter rocks at distances over a few meters (Winter, 2001), especially since metasomatic fluids would have cooled rapidly upon reaching the summit limestone. Consequently, such a steep geothermal gradient is feasible and, therefore, the fabrics observed in Summit samples may not be genetically

related to those seen in South Summit samples. Rather, the well-developed mylonitic foliation of Summit samples is a result of faulting during initial crustal thickening sometime between the Middle Eocene and Early Oligocene, prior to *c*. 30.5 Ma, whereas the fabrics and microstructures preserved in South Summit samples are a result of leucogranite injection and faulting on the Qomolangma detachment in the Early Miocene.

Relationship Between Normal Faulting and Leucogranite Emplacement

Crustal anatexis and leucogranite generation has been temporally linked to decompression associated with tectonic unroofing along the STDS (e.g., Harris and Massey, 1994); however, geochronology shows that early melt migration in the Everest region predates the earliest known movement on the STD. Furthermore, leucogranite bodies are always restricted to the footwall and are truncated or sheared by normal faulting, indicating that faulting outlasted leucogranite injection. Melting and leucogranite emplacement has been episodic throughout the Himalayan orogen and timing of movement on the STDS also varies, occurring on different strands of the fault system at different times. Data presented herein demonstrates that metasomatic fluids reached the South Summit at ~25 meters above the Qomolangma detachment on Mount Everest (Figure 1 and 13). Thus, these fluids could have also been present within the detachment fault zone, possibly using the fault plane as a conduit for fluid migration. Metasomatic phases in South Summit samples are syn-kinematic, indicating a close temporal relationship between faulting and the injection of leucogranite. These data suggest that hydrothermal fluids discharged from footwall-restricted leucogranites may

have been a catalyst for faulting. It is well established that for slip to occur on low-angle detachments there must be a mechanism which decreases the shear stress necessary to initiate faulting (i.e., reduces the effective stress; Gudmundsson, 2011). This concept can be explained by Coulomb's shear-failure criterion and the equation:

$$\tau = C + \mu(\sigma_n - P_f)$$

Where τ is shear stress necessary to initiate faulting; C is the cohesion of the rock; μ is the coefficient of internal friction; σ_n is the normal stress across the fault plane; and P_f is the fluid pressure in pores of the rock. This equation shows how the shear stress needed to cause faulting decreases as a function of increasing pore fluid pressure, and how hydrothermal fluids released from leucogranites could have facilitated slip on the Qomolangma detachment. Also, the presence of water in a fault zone can cause hydrolytic weakening of silicate minerals (Nakashima et al., 1995), as well as produce alteration minerals which tend to have lower shear strength than unaltered minerals, allowing deformation to occur at lower stresses (Van der Pluijm and Marshak, 2004). Thus, hydrothermal fluids released from leucogranites could have had a significant influence on fault activation across the STDS.

Four key points that support this hypothesis are revealed by a review of leucogranite geochronology and timing of slip on the South Tibetan Detachment in the central Himalaya. (1) Leucogranite generation and emplacement consistently precedes the onset of detachment faulting; (2) leucogranite bodies are always restricted to the footwall; (3) even the youngest dikes which crosscut metamorphic fabric in the footwall are in turn truncated by faulting on the detachment above; (4) leucogranite crystallization

ages generally young to the north. Because granites get younger to the north, the locus of leucogranite emplacement must have continually migrated to higher structural levels within the Greater Himalayan Sequence. While dikes that are truncated by faulting provide a minimum upper age constraint of faulting, there are however, very few lower age constraints. The only geochronologic data that gives an absolute lower limit on fault timing is the generation of north-south trending normal faults in southern Tibet that crosscut the detachment system at *c*. 8 Ma in the Nyainqentanghla Shan, 100 km northwest of Lhasa (Harrison et al., 1995), and *c*. 11 Ma in Dinggye, 90 km northeast of Everest (Leloup et al., 2010).

For example, in the Everest region early melting occurred in the Namche orthogneiss between *c*. 26-23 Ma (Viskupic and Hodges, 2001; Viskupic et al., 2005) and subsequent crystallization of the Nuptse and Everest granites took place at 23.6 Ma (Jessup et al., 2008) and 20.5-21.3 Ma (Simpson et al., 2000), respectively, and crystallization of early leucogranites in the Kangshung valley occurred at 20.8 Ma (Cottle et al., 2009). Following emplacement of these bodies the Lhotse Shear Zone was active possibly as early as 23.6 Ma (i.e., immediately following the final crystallization of the Nuptse granite), but was certainly active between 18.3 Ma to 16.9 Ma (Searle et al., 2003). Later dikes which crosscut metamorphic fabric in the footwall of the STD near Everest span a range of dates including 17.6 Ma to 18.3 Ma near Gokyo Ri 20 km west of Everest (Viskupic et al., 2005), 16.7 Ma in the Kangshung valley east of Everest (Cottle et al., 2009), 16.5 Ma on Lingtren (Searle et al., 2003), and from 16.2 Ma to 16.8 Ma immediately north of Everest in the Rongbuk valley (Murphy and Harrison, 1999). The youngest of these bodies are the late-stage dikes dated by Murphy and Harrison, which

are sheared and mylonitized by movement on the detachment directly above, indicating that movement on this structure outlasted the emplacement of leucogranites in the Everest region.

Similarly, at Shisha Pangma 120 km west of Everest, the STD has placed unmetamorphosed sediments directly over 20.2 Ma to 17.3 Ma leucogranites in the immediate footwall, and the youngest granite bodies are all cut by movement on the detachment above (Searle et al., 1997). In Dinggye 90 km northeast of Everest, leucogranites proximal to and within the STD shear zone are deformed by faulting and are all restricted to the footwall. Here, the age of leucogranites range from *c*. 12 Ma to *c*. 20 Ma, while motion on the detachment ceased between 13.6 Ma and *c*. 11 Ma (Leloup et al., 2010). In the Manaslu region 220 km west of Everest, leucogranite bodies again are restricted to the footwall and melt emplacement occurred between *c*. 24-19 Ma while normal faulting took place at *c*. 19-18 Ma and younger (Searle and Godin, 2003). These data show that initiation of the STD in the Everest area, and the Central Himalaya in general, followed initial anatexis and that movement on the STD outlasted subsequent phases of leucogranite injection.

Based on this information, perhaps the initial generation of anatectic leucogranite is not a result of decompression related to tectonic unroofing along the STD. Instead, it is proposed here that early leucogranite emplacement facilitated slip on the STDS by elevating fluid pressure and weakening rocks in the fault zone. In this scenario extensional stresses necessary to drive normal faulting would need to be present, and they probably already were; generated by lateral pressure gradients created by the extreme topographic contrast between the Tibetan Plateau-Himalayan orogen and the Indian plate

to the south (conditions for gravitational spreading; Johnson and Harley, 2012). With subhorizontal stresses present in the crust, any localized thermal or hydrolytic weakening of the crust coupled with elevated fluid pressure, could have resulted in normal faulting. Subsequent episodes of leucogranite generation and emplacement may have been a result of decompression related anatexis that occurred after detachment faulting had been long-lived enough to result in significant tectonic denudation. But, even the youngest leucogranite bodies are truncated by faulting, suggesting that normal faulting may have been once again provoked in the same way that it originally initiated. This implies that slip on the STDS and leucogranite generation-emplacement formed a positive feedback relationship, such that removal of overburden and concomitant decompression led to local anatexis, which then promoted renewed motion on the detachment by weakening rocks and increasing fluid pressure in the fault zone. This relationship resulted in the episodic nature of both systems, spanning a fairly wide range in the Miocene and overlapping in time throughout their existence, as the geochronologic data suggests.

CHAPTER 9

CONCLUSIONS

Microstructural data shows that samples from the summit of Mount Everest are pervasively sheared and have undergone deformation at temperatures of ≥ 250°C; at this structural level the Qomolangma Formation is a calc-mesomylonite. A mylonitic foliation is not present at the Hillary Step due to extensive recrystallization that completely consumed original grains of calcite and dolomite, resulting in a rheologically homogenous material. At the base of the formation (South Summit) samples have undergone metamorphism at temperatures of 500-600ºC, as indicated by Ti-in-biotite and Titanium-in-quartz (TitaniQ) geothermometry. Here, a mylonitic foliation is again present due to the rheologic contrast created by a quartz vein that has fractured into large clasts, creating perturbations in the matrix flow fabric. The increased temperature at the base of the summit limestone has resulted in widespread growth of calcite and quartz in the matrix, overprinting the matrix texture seen in Summit and Hillary Step samples; here, the Qomolangma Formation is a marble mylonite and calc-silicate. Geochemical analysis of tourmaline suggests that metamorphism of South Summit samples was the result of metasomatism associated with the injection of Himalayan leucogranites into structurally subjacent formations in the Early Miocene. Mica phases in South Summit samples that precipitated from metasomatic fluids show a close temporal relationship between timing of crystallization and the development of fabrics associated with faulting on the Qomolangma detachment; suggesting that metasomatic fluids may have promoted

movement on the Qomolangma detachment by increasing fluid pressure and weakening rocks proximal to the fault plane.

The change in fabric and metamorphic temperature observed between the different structural horizons is interpreted to be a result of distinct deformational and metamorphic events that influenced the Qomolangma Formation at different times throughout Himalayan orogenesis. The well-developed mylonitic foliation seen in Summit samples is interpreted to have been ingrained during initial thrust faulting and crustal thickening of the Tethyan Himalayan Sequence, from the Middle Eocene to the Early Oligocene. In contrast, the fabric and elevated metamorphic temperature preserved by South Summit samples is thought to be a result of events that occurred in the Early Miocene, including leucogranite emplacement with concomitant metasomatism, and faulting on the Qomolangma detachment. This implies that some of the most important tectonic events involved in Himalayan orogenesis are recorded in the Qomolangma Formation, a succession of deformed limestone that now comprises the uppermost ~125 meters of Mount Everest.

REFERENCES CITED

Ahr, W.M., 1973, The carbonate ramp; an alternative to the shelf model: Gulf Coast Association of Geological Societies - Transactions v. 23, p. 221-225.

Aitken, J.D., 1967, Classification and environmental significance of cryptalgal limestones and dolomites, with illustrations from the Cambrian and Ordovician of southwestern Alberta: Journal of Sedimentary Petrology, v. 37, p. 1163-1178.

Aldrich, L.T., and Nier, A.O., 1948, Argon 40 in potassium minerals: Physical Review, v. 74, p. 876-877.

Algeo, T.J., and Seslavinsky, K.B., 1995, The Paleozoic world: continental flooding, hypsometry, and sea-level: American Journal of Science, v. 295, p. 787-822.

Arita, K., Dallmeyer, R.D., and Takasu, A., 1997, Tectonothermal evolution of the Lesser Himalaya, Nepal: constraints from Ar/Ar ages from the Kathmandu Nappe: The Island Arc, v. 6, p. 372-385.

Armella, C., 1994, Thrombolitic-stromatolitic cycles of the Cambro-Ordovician boundary sequence, Precordillera Oriental Basin, western Argentina, *In* Bertrand-Sarfati, J., and Monty, C.L.V., (eds) Phanerozoic Stromatolites II: Dordrecht, Netherlands, Kluwer Academic, p. 421-441.

Armstrong, J. T., 1988, Quantitative analysis of silicates and oxide minerals: Comparison of Monte-Carlo, ZAF and Phi-Rho-Z procedures: Microbeam Analysis p. 239-246.

Barber, D.J., Wenk, H.-R., and Hugh, C.H., 1994, The plastic deformation of polycrystalline dolomite: comparison of experimental results with theoretical predictions: Materials Science and Engineering, v. 175, p. 83-104.

Barber, J.B., and Wenk, H.-R., 2001, Slip and dislocation behavior in dolomite: European Journal of Mineralogy, v. 13, p. 221-243.

Beaumont, C., Jamieson, R.A., Nguyen, M.H., and Lee, B., 2001, Himalayan tectonics explained by extrusion of a low-viscosity crustal channel coupled to focused surface denudation: Nature, v. 414, p. 738-742.

Beaumont, C., Jamieson, R.A., Nguyen, M.H., and Medvedev, S., 2004, Crustal channel flows: 1. Numerical models with applications to the tectonics of the Himalayan-Tibetan orogen: Journal of Geophysical Research, v. 109, DOI: 10.1029/2003JB002809.

Bell, T.H., and Etheridge, M.A., 1973, Microstructure of mylonites and their descriptive terminology: Lithosphere, v. 6, p. 337-348.

Bell, T.H., and Etheridge, M.A., 1976, The deformation and recrystallization of quartz in a mylonite zone, Central Australia: Tectonophysics, v. 32, p. 235-267.

Benton, M.J., and Harper, D.A.T., 2009, Introduction to paleobiology and the fossil record: Wiley-Blackwell, v. 1.

Bestmann, M., Prior, D.J., 2003, Intragranular dynamic recrystallization in naturally deformed calcite marble: diffusion accommodated grain boundary sliding as a result of subgrain rotation recrystallization: Journal of Structural Geology, v. 25, p. 1597-1613.

Boggs, S., Jr, 2003, Petrology of Sedimentary Rocks: The Blackburn Press, v. 2, 707 p.

Brookfield, M.E., 1993, The Himalayan passive margin from Precambrian to Cretaceous time: Sedimentary Geology, v. 84, p. 1-35.

Burchfiel, B.C., and Royden, L.H., 1985, North-south extension within the convergent Himalayan region: Geology, v. 13, p. 679-682.

Burchfiel, B.C., Zhiliang, C., Hodges, K.V., Yuping, L., Royden, L., Changrong, D., and Jiene, X., 1992, The South Tibetan Detachment System, Himalayan Orogen: extension contemporaneous with and parallel to shortening in a collisional mountain belt: Geological Society of America Special Papers, v. 269.

Burg, J.P., Proust, F., Tapponnier, P., and Ming, C.G., 1983, Deformation of leucogranites of the crystalline Main Central sheet in southern Tibet (China): Journal of Structural Geology, v. 76, p. 535-542.

Burg, J.P., and Chen, G.M., 1984, Tectonics and structural zonation of southern Tibet, China: Nature, v. 311, p. 219-223, doi: 1038/311219a0.

Burg, J.P., Nievergelt, P., Oberli, F., Seward, D., Davy, P., Maurin, J.C., Diao, Z., and Meier, M., 1998, The Namche Barwa syntaxis: Evidence for exhumation related to compressional crustal folding: Journal of Asian Earth Sciences, v. 16, p. 239-252.

Burkhard, M., 1993, Calcite twins, their geometry, appearance and significance as stress-strain markers and indicators of tectonic regime, a review: Journal of Structural Geology, v. 15, p. 351-368.

Caby, R., Pêcher, A., and Le Fort, P., 1983, Le grande chevauchement central himalayen: Nouvelles données sur le métamorphisme inverse à la base de la Dalle du Tibet: Revue de Géographie Physiqueau et Géologie Dynamique, v. 24, p. 89-100.

Carosi, R., Lambardo, B., Molli, G., Musumeci, G., and Pertusati, P.C., 1998, The south Tibetan detachment system in the Rongbuk valley, Everest region. Deformation

features and geological implication: Journal of Asian Earth Sciences, v. 16, p. 299-311.

Carosi, R., Lombardo, B., Musumeci, G., and Pertusati, P.C., 1999, Geology of the Higher Himalayan Crystallines in Khumbu Himal (Eastern Nepal): Journal of Asian Earth Sciences, v. 17, p. 785-803.

Catlos, E. J., Harrison, T. M., Manning, C. E., et al., 2002, Records of the evolution of the Himalayan orogen from in situ Th-Pb ion microprobe dating of monazite: eastern Nepal and western Garhwal: Journal of Asian Earth Sciences, v. 20, p. 459–479.

Cavaretta, G., and Puxedda, M., 1990, Schorl-dravite-ferridravite tourmalines deposited by hydrothermal magmatic fluids during early evolution of the Larderello geothermal field, Italy: Economic Geology, v. 85, p. l236-1251.

Coleman, M.E., and Hodges, K.V., 1998, Contrasting Oligocene and Miocene thermal histories from the hanging wall and footwall of the South Tibetan detachment in the central Himalaya from $^{40}Ar/^{39}Ar$ thermochronology Marsyandi valley, central Nepal: Tectonics, v. 17, p. 726-740.

Cottle, J.M., Jessup, M.J., Newell, D.L., Searle, M.P., Law, R.D., and Horstwood, M.S.A., 2007, Structural insights into the early stages of exhumation along an orogen-scale detachment: The South Tibetan Detachment System, Dzakaa Chu section, Eastern Himalaya: Journal of Structural Geology, v. 29, p. 1781-1797.

Cottle, J.M., Searle, M.P., Horstwood, M.S.A., and Waters, D., 2009, Timing of midcrustal metamorphism, melting, and deformation in the Mount Everest region of south Tibet revealed by U(-Th)-Pb geochronology: The Journal of Geology, v. 117, p. 643-664.

Cottle, J.M., Waters, D.J., Riley, D., Beyssac, O., and Jessup, M.J., 2011, Metamorphic history of the South Tibetan Detachment System, Mt. Everest region, revealed by RSCM thermometry and phase equilibria modeling: Journal of metamorphic Geology, v. 29, p. 561-582.

Couch, E.L., and Grim, R.E., 1968, Boron fixation by illites: Clays and Clay Minerals, v. 16, p. 249-256.

Crowley, J.L., Bowring, S.A., and Searle, M.P., 2005, U-Th-Pb systematics of monazite, xenotime, and zircon from Pleistocene leucogranites at Nanga Parbat: Geochimica et Cosmochimica Acta, v. 69, p. 8.

Crowley, J.L., Waters D.J., Searle, M.P., and Bowring, S.A., 2009, Pleistocene melting and rapid exhumation of the Nanga Parbat massif, Pakistan: Age and P-T

conditions of accessory mineral growth in migmatite and leucogranite, Earth and Planetary Science Letters, v. 288(3–4), p. 408-420.

Davis, N.E., Kronenberg, A.K., and Newman, J., 2008, Plasticity and diffusion creep of dolomite: Tectonophysics, v. 456, p. 127-146.

Deniel, C., Vidal, P., Fernandez, A., Le Fort, P., and Peucat, J., 1987, Isotopic study of the Manaslu granite (Himalaya, Nepal): inferences in the age and source of the Himalayan leucogranites: Contributions to Mineralogy and Petrology, v. 96, p. 78-92.

De Bresser, J.H.P., Ter Heege, J.H., and Spiers, C.J., 2001, Grain size reduction by dynamic recrystallization: can it result in major rheological weakening?: International Journal of Earth Sciences, v. 90, p. 28-45.

de Hoff R.T., and Rhines F.N., 1968, Quantitative microscopy: McGraw Hill, New York.

den Brok, S.W.J., and Spiers, C.J., 1991, Experimental evidence for water weakening of quartzite by microcracking plus solution-precipitation creep: Journal of the Geological Society of London, v. 147, p. 541-548.

Dewey, J.F., Cande, S., and Pitman, W.C., 1989, Tectonic evolution of the India–Eurasia collision zone: Eclogae Geologicae Helvetiae, v. 82, p. 717-734.

Dietrich, R.V., 1985, The tourmaline group; a resume: The Mineralogical Record, v. 16, p. 339-351.

DiPietro, J.A., and Pogue, K.R., 2004, Tectonostratigraphic subdivisions of the Himalaya: A view from the west: Tectonics, v. 23, p. 1-20.

Dunham, R.J., 1962, Classification of carbonate rocks according to depositional texture, *In* Ham, W.E., (eds) Classification of carbonate rocks: American Association of Petroleum Geologists - Memoir 1, p. 108-121.

Dutrow, B.L., and Henry, D. J., 2014, Tourmaline: The Perfect Accessory: Goldschmidt Abstracts, 2014, p. 610.

Dutrow, B.L., Norton, D., and Henry, D.J., 1989, Tourmaline-bearing pseudomorphs after staurolite: Boron metasomatism in high grade metapelites: Geological Society of America Abstract Program v. 21, A328.

Dutrow, B.L., and Henry, D.J., 2011, Tourmaline: a geologic DVD: Elements, v. 7, p. 301–306.

Edwards, M. A., Kidd, W. S. F., Li, J., Yue, Y., and Clark, M., 1996, Multi-stage development of the southern Tibet detachment system near Khula Kangri: New data from Gonto La: Tectonophysics, v. 260, p. 1-19.

Evans, M.A., and Dunne, W.M., 1991, Strain factorization and partitioning in the North Mountain thrust sheet, central Appalachians, USA: Journal of Structural Geology, v. 13, p. 21-35.

Faure, G., and Mensing, T.M., 2005, Isotopes: principles and applications: John Wiley and Sons, Inc., New Jersey, v. 3, 897 p.

Ferrill, D.A., and Groshong, R.H. Jr, 1993, Deformation conditions in the northern Subalpine Chain, France, estimated from deformation modes in coarse-grained limestone: Journal of Structural Geology, v. 15, p. 995-1006.

Ferrill, D.A., 1991, Calcite twin widths and intensities as metamorphic indicators in natural low-temperature deformation of limestone: Journal of Structural Geology, v. 13, p. 667-675.

Ferrill, D.A., Morris, P.A., Evans, M.A., Burkhard, M., Groshong Jr, R.H., and Onasch, C.M., 2004, Calcite morphology: a low-temperature deformation geothermometer, Journal of Structural Geology, v. 26, p. 1521-29.

Flüegel, E., 2004, Microfacies of carbonate rocks; analysis, interpretation and application: Springer, Berlin, 976 p.

Folk, R.L., 1962, Spectral subdivision of limestone types, *In* Ham, W.E., (eds) Classification of carbonate rocks: American Association of Petroleum Geologists - Memoir, v. 1, p. 62-84.

Gansser, A., 1964, Geology of the Himalayas: Interscience Publishers, London, United Kingdom, J. Wiley and Sons, 289 p.

Gansser, A., 1977, The great suture zone between Himalaya and Tibet, a preliminary account: Science de la Terre, Himalaya: Centre National de la Recherche Scientifique, v. 268, p. 147-166.

Garzanti, E., 1999, Stratigraphy and sedimentary history of the Nepal Tethys Himalaya passive margin: Journal of Asian Earth Sciences, v. 17, p. 805-827.

Garzanti, E., and Pagni Frette, M., 1991, Stratigraphic succession of the Thakkhola region (Central Nepal): Comparison with the Northwestern Tethys Himalaya: Rivista Italiana di Paleontologia e Stratigrafia, v. 97, p. 3-26.

Godin, L., Parrish, R.R., Brown, R.L., and Hodges, K.V., 2001, Crustal thickening leading to exhumation of the Himalayan Metamorphic core of central Nepal: Insight from U-Pb geochronology and $^{40}Ar/^{39}Ar$ thermochronology: Tectonics, v. 20, p. 729-747.

Godin, L., Grujic, D., Law, R.D., and Searle, M.P., 2006*a*, Channel flow, ductile extrusion and exhumation in continental collision zones: an introduction, *In* Law, R.D., Searle, M.P., and Godin, L., (eds) Channel Flow, Ductile Extrusion and Exhumation in Continental Collision Zones: Geological Society, London, Special Publication, v. 268, p. 1-23.

Godin, L., Gleeson, T.P., Searle, M.P., Ullrich, T.D., and Parrish, R.R., 2006*b*, Locking of southward extrusion in favour of rapid crustal-scale buckling of the Greater Himalayan Sequence, Nar Valley, Central Nepal, *In* Law, R.D., Searle, M.P., and Godin, L., (eds) Channel Flow, Ductile Extrusion and Exhumation in Continental Collision Zones: Geological Society, London, Special Publication, v. 268, p. 269-296.

Goscombe, B., Gray, D., and Hand, M., 2006, Crustal architecture of the Himalayan metamorphic front in eastern Nepal: Gondwana Research, v. 10, p. 232–255.

Gregg, J.M., and Sibley, D.F., 1984, Epigenetic dolomitization and the origin of Xenotopic dolomite texture: Journal of Sedimentary Petrology, v. 54, p. 908-931.

Grew, E.S., 1996, Borosilicates (exclusive of tourmaline) and boron in rock-forming minerals in metamorphic environments, *In* Grew, E.S., and Anovitz, L.M., (eds) Boron: Mineralogy, Petrology and Geochemistry: Reviews in Mineralogy, v. 33, p. 388-502.

Groshong Jr, R.H., 1988, Low-temperature deformation mechanisms and their interpretation; Geological Society of America Bulletin, v. 100, p. 1329-60.

Grujic, D., Casey, M., Davidson, C., et al., 1996, Ductile extrusion of the Higher Himalayan Crystalline in Bhutan: evidence from quartz microfrabics: Tectonophysics, v. 260, p. 21-43.

Grujic, D., Hollister, L.S. and Parrish, R.R., 2002, Himalayan metamorphic sequence as an orogenic channel: insight from Bhutan: Earth and Planetary Science Letters, v. 198, p. 177-191.

Gudmundsson, A., 2011, Rock fractures in geologic processes: Cambridge University Press, Cambridge, UK, 578 p.

Guillopé, M., Poirier, J.P., 1979, Dynamic recrystallization during creep of single-crystalline halite: an experimental study: Journal of Geophysical Research, v. 84, p. 5557–5567.

Guillot, S., and Le Fort, P., 1995, Geochemical constraints on the bimodal origin of High Himalayan leucogranites: Lithos, v. 35, p. 221-234.

Guo, Z., and Wilson, M., 2012, The Himalayan leucogranites: Constraints on the nature of their crustal source region and geodynamic setting: Gondwana Research, v. 22, p. 360-376.

Gysin, M., and Lombard, A., 1959, Note sur la composition des roches me´tamorphiques et se´dimentaires des sommets du Mont Everest-Lhotse (Himalaya): Archives des Sciences, Gene`ve, v. 12, p. 98-101.

Gysin, M., and Lombard, A., 1960, Observations comple´mentaires de pe´trographie et de ge´ologie dans le Massif du Mont Everest Lhotse: Eclogae Geologicae Helvetiae, v. 53, p. 189-204.

Haertel, M., Herwegh, M., and Pettke, T., 2013, Titanium-in-quartz thermometry on synkinematic quartz veins in a retrograde crustal-scale normal fault zone: Tectonophysics, v. 608, p. 468-481.

Harder, H., 1970, Boron content in sediments as a tool in facies analysis: Sedimentary Geology, v. 4.2, p. 153-157.

Harper, D.A.T., 2006, The Ordovician biodiversification: setting an agenda for marine life: Palaeogeography, Palaeoclimatology, Palaeoecology, v. 232, p. 148-166.

Harper, D.A.T., Zhan, R., Stemmerik, L., Liu, J., Donovan, S.K., and Stouge, S., 2011, Ordovician on the roof of the world: macro- and microfaunas from tropical carbonates in Tibet, *In* Marco, J.C.G., Rabano, I., and Bellido, D.G., (eds) Ordovician of the World: Instituto Geologico y Minero de Espana, Madrid, p. 215-220.

Harris, N., and Massey, J., 1994, Decompression and anatexis of Himalayan metapelites: Tectonics, p. 13, v. 1537-1546.

Harris, N., Ayres, M., and Massey, J., 1995, Geochemistry of granitic melts produced during the incongruent melting of muscovite: Implications for the extraction of Himalayan leucogranite magmas: Journal of Geophysical Research, 100.B8, 15,767-15,591, doi:10.1029/94JB02623.

Harrison, T. M., Copeland, P., Kidd, W. S. F., and Lovera, O. M., 1995, Activation of the Nyainqentanghla shear zone: Implications for uplift of the southern Tibetan Plateau: Tectonics, v. 14, p. 658-676.

Harrison, T.M., Grove, M., McKeegan, K.D., Coath, C.D., Lovera, O.M., and Le Fort, P., 1999*a*, Origin and episodic emplacement of the Manaslu intrusive complex, central Himalaya: Journal of Petrology, v. 40, p. 3-19.

Harrison, T. M., Grove, M., Lovera, O. M., Catlos, E. J., and D'Andrea, J., 1999*b*, The origin of Himalayan anatexis and inverted metamorphism: Models and constraints: Journal of Asian Earth Sciences, v. 17, p. 755-772.

Hauck, M.L., Nelson, K.D., Brown, L.D., Zhao, W.J., and Ross, A.R., 1998, Crustal structure of the deep Himalayan Orogen from Project INDEPTH deep seismic reflection profiles at *c*. 90° E: Tectonics, v. 17, p. 481-500.

Hawthorne, F.C., and Dirlam, D.M., 2011, Tourmaline the indicator mineral: from atomic arrangement to Viking navigation: Elements, v. 7, p. 307-312.

Heim, A., and Gansser, A., 1939, Central Himalaya: Geological Observations of the Swiss Expedition, 1936: Memoires de la Socie´te´ helvetique des Sciences Naturelles, v. 73.

Henry, D.J., Lu, G., and McCabe, C., 1994, Epigenetic tourmaline in sedimentary red-beds: An example from the Silurian Rose Hill Formation, Virginia: Canadian Mineralogist v. 32, p. 599-605.

Henry, D.J., and Dutrow, B.L., 1996, Metamorphic tourmaline and its petrologic applications, *In* Grew, E.S., and Anovitz, L.M., (eds) Boron: Mineralogy, Petrology and Geochemistry: Reviews in Mineralogy, v. 33, p. 503-557.

Henry, D.J., and Guidotti, C.V., 2002, Titanium in biotite from metapelitic rocks: temperature effects, crystal-chemical controls, and petrologic applications: American Mineralogist, v. 87, p. 375-382.

Henry, D.J., Guidotti, C.V., and Thomson, J.A., 2005, The Ti-saturation surface for low-to-medium pressure metapelitic biotites: Implications for geothermometry and Ti-substitution mechanisms: American Mineralogist, v. 90, p. 316-328.

Henry, D.J., and Dutrow, B.L., 2012, Tourmaline at diagenetic to low-grade metamorphic conditions: Its petrologic applicability: Lithos, v. 154, p. 16-32.

Hirth, G., and Tullis, J., 1992, Dislocation creep regimes in quartz aggregates: Journal of Structural Geology, v. 14, p. 145-159.

Hodges, K.V., Hubbard, M.S., and Silverberg, D.S., 1988, Metamorphic constrains on the thermal evolution of the central Himalayan orogen: Philosophical Transactions of the Royal Society of London, v. 326, p. 257-280.

Hodges, K.V., Parrish, R.R., Housh, T.B., Lux, D.R., Burchfiel, B.C., Royden, L.H., and Chen, Z., 1992, Simultaneous Miocene extension and shortening in the Himalayan orogen: Science, v. 258, p. 1466-1470.

Hodges, K.V., Burchfiel, B.C., Royden, L.H., Chen, Z. and Liu, Y., 1993, The metamorphic signature of contemporaneous extension and shortening in the central Himalayan orogen: data from the Nyalam transect, southern Tibet: Journal of Metamorphic Geology, v. 11, p. 721-737.

Hodges, K.V., Bowring, S., Davidek, K., Hawkins, D., and Krol, M., 1998, Evidence for rapid displacement on Himalayan normal faults and the importance of tectonic denudation in the evolution of mountain ranges: Geology, v. 26, p. 483-486.

Hodges, K.V., 2000, Tectonics of the Himalaya and southern Tibet from two perspectives: Geological Society of America Bulletin, v. 112, p. 324-350.

Hodges, K.V., Hurtado, J.M., and Whipple, K.X., 2001, Southward extrusion of Tibetan crust and its effect on Himalayan tectonics: Tectonics, v. 20, p. 799-809.

Holyoke, C.W., and Kronenberg, K., 2010, Accurate differential stress measurement using the molten salt cell and solid salt assemblies in the Griggs apparatus with applications to strength, piezometers and rheology: Tectonophysics, v. 494, p. 17-31.

Hubbard, M.S., and Harrison, T.M., 1989, 40Ar/39Ar age constraints on deformation and metamorphism in the Main Central Thrust zone and Tibetan slab, eastern Nepal Himalaya: Tectonics, v. 8, p. 865-880.

Hubbard, M.S., 1989, Thermobarometric constraints on the thermal history of the Main Central Thrust Zone and Tibetan Slab, eastern Nepal Himalaya: Journal of Metamorphic Geology, v. 7, p. 19-30.

Hubbard, M.S., 1996, Ductile shear as a cause of inverted metamorphism: Example from the Nepal Himalaya: Journal of Geology, v. 194, p. 493-499.

Hubbert, M.K., and Rubey, W.W., 1959, Role of fluid pressure in the mechanics of overthrust faulting: Geological Society of America Bulletin, v. 70, p. 115-166.

Hull, D., 1975, Introduction to dislocations: Pergamon Press, Oxford, 271 p.

Humphreys, F.J., 1999, Quantitative metallography by electron backscatter diffraction: Journal of Microscopy, v. 195, p. 170-185.

Humphreys, F.J., 2001, Review: Grain and subgrain characterization by electron backscatter diffraction: Journal of Materials Science, v. 36, p. 3833-54.

Jamison, W.R., and Spang, J.H., 1976, Use of calcite twin lamellae to infer differential stress: Geological Society of America Bulletin, v. 87, p. 868-872.

Jamison, R.A., Beaumont, C., Nguyen, M.H., and Grujic, D., 2006, Provenance of the Greater Himalayan Sequence and associated rocks: predictions of channel flow models, *In* Law, R.D., Searle, M.P., and Godin, L., (eds) Channel Flow, Ductile Extrusion and Exhumation in Continental Collision Zones: Geological Society, London, Special Publication, v. 268, p. 165-182.

Jessup, M.J., Law, R.D., Searle, M.P., and Hubbard, M.S., 2006, Structural evolution and vorticity of flow during extrusion and exhumation of the Greater Himalayan Slab, Mount Everest massif, Tibet/Nepal: implications for orogen-scale flow partitioning, *In* Law, R.D., Searle, M.P., and Godin, L., (eds) Channel Flow, Ductile Extrusion and Exhumation in Continental Collision Zones: Geological Society, London, Special Publication, v. 268, p. 379-414.

Jessup, M.J., Cottle, J.M., Searle, M.P., Law, R.D., Newell, D.L., Tracy, R.J., and Waters, D.J., 2008, P-T-t-D paths of Everest Series schist, Nepal: Journal of Metamorphic Geology, v. 26, p. 717-739.

Jessup, M.J., and Cottle, J.M., 2010, Progression from South-Directed Extrusion to Orogen-Parallel Extension in the Southern Margin of the Tibetan Plateau, Mount Everest Region, Tibet: Journal of Geology, v. 118, p. 467-486.

Johnson, M.R.W., and Rogers, G., 1997, Rb–Sr ages of micas from the Kathmandu complex, Central Nepalese Himalaya: implications for the evolution of the Main Central Thrust: Journal of the Geological Society, v. 154, p. 863-869.

Johnson, M.R.W., Oliver, G.J.H., Parrish, R.R., and Johnson, S.P., 2001, Synthrusting metamorphism, cooling, and erosion of the Himalayan Kathmandu Complex, Nepal: Tectonics, v. 20, p. 394-415.

Johnson, M.R.W., and Harley, S.L., 2012, Orogenesis, the making of mountains: Cambridge University Press, v. 1, p. 388.

Kennard, J.M., and James, N.P., 1986, Thrombolites and stromatolites: two distinct types of microbial structures: Palaios, v. 1, p. 492-503.

Kennedy, L.A., and White, J.C., 2002, Low temperature recrystallization of calcite: mechanisms and consequences: Geology, v. 29, p. 1027-1030.

Knipe, R.J., 1989, Deformation mechanisms – recognition from natural tectonites: Journal of Structural Geology, v. 11, p. 127-146.

Law, R.D., Searle, M.P., and Simpson, R.L., 2004, Strain, deformation temperatures and vorticity of flow at the top of the Greater Himalayan Slab, Everest Massif, Tibet: Journal of the Geological Society, London, v. 161, p. 305-320.

Law, R.D., Searle, M.P., and Godin L., 2006, Channel Flow, Ductile Extrusion and Exhumation in Continental Collision Zones: Geological Society of London Hardcover, Special Publications, v. 268, 620 p.

Le Fort, P., 1975, Himalayas: the collided range. Present knowledge of the continental arc: American Journal of Science, v. 275-a, p. 1–44.

Le Fort, P., Cuney, M., Deniel, C., France-Lanord, C., Sheppard, S. M. F., Upreti, B. N., and Vidal, P., 1987, Crustal generation of the Himalayan leucogranites: Tectonophysics, v. 134, p. 39–57.

Leeman, W.P., and Sisson, V.B., 1996, Geochemistry of boron and its implications for crustal and mantle processes, *In* Grew, E.S., and Anovitz, L.M., (eds) Boron: Mineralogy, Petrology and Geochemistry: Reviews in Mineralogy, v. 33, p. 645-707.

Leloup, P.H., Mahéo, G., Arnaud, N., Kali, E., Boutonnet, et al., 2010, The South Tibetan detachment shear zone in the Dinggye area time constraints on extrusion models of the Himalayas: Earth and Planetary Science Letters, v. 292, p. 1-16.

Lerman, A., 1966, Boron in clays and estimation of palaeosalinities: Sedimentology v. 6, p. 267-286.

Liu D., 1976, Ordovician brachiopods from the Mount Jolmo Lungma region, 139–158, *In*: Report of the Scientific Expedition to the Mount Jolmo Lungma Region (1966-1968), Palaeontology, II: Beijing, Science Press (in Chinese).

Lombardo, B., Pertusati, P., and Borgi, S., 1993, Geology and tectonomagmatic evolution of the eastern Himalaya along the Chomolungma-Makalu transect, *In* Treloar, P.J., and Searle, M.P., (eds) Himalayan Tectonics: Geological Society, London, Special Publications, v. 74, p. 485-509.

London, D., Morgan, G.B. VI, and Wolf, M.B., 1996, Boron in granitic rocks and their contact aureoles, *In* Grew, E.S., and Anovitz, L.M., eds Boron: Mineralogy, Petrology and Geochemistry: Reviews in Mineralogy, v. 33, p. 299-330.

London, D., 1999, Stability of Tourmaline in peraluminous granite systems: the boron cycle from anatexis to hydrothermal aureoles: European Journal of Mineralogy, v. 11, p. 253-262.

Lloyd, G.E., and Freeman, B., 1994, Dynamic recrystallisation of quartz and quartzites: Journal of Structural Geology, v. 16, p. 867-881.

McDougall, I., and Harrison, M.T., 1999, Geochronology and thermochronology by the $^{40}Ar/^{39}Ar$ method: Oxford University Press, New York, v. 2, 269 p.

Meigs, A.J., Burbank, D.W., Beck, R.A., 1995, Middle-Late Miocene (greater-than-10 Ma) formation of the Main Boundary Thrust in the western Himalaya. Geology, v. 23, p. 423-426.

Mercier, J.C., Anderson, D.A., and Carter N.L., 1977, Stress in the lithosphere: inferences from steady-state flow of rocks: Pure Appl Geophysics, v. 115, p. 119-226.

Merrihue, C., and Turner, G., 1966, Potassium-argon dating by activation with fast neutrons: Journal of Geophysical Research, v. 71, p. 2852-2857.

Molnar, P., 1988 Structure and Tectonics of the Himalaya: constraints and implications of geologic data: Annual Review of the Earth and Planetary Sciences, v. 12, p. 489-518.

Morgan, G.B.VI, and London, D., 1987, Behavior of boron and tourmaline stability in granitic systems: Geologic Society of America Abstract Program v. 19 p. 777-778.

Mosar, J., 1989, Deformation interne dans les Prealpes medianes (Suisse): Eclogae geologicae Helvetiae, v. 82, p. 765-793.

Mu, A.T., Wen, S.H. Wang, Y.K., Chang, P.K., and Yin, C.H., 1973, Stratigraphy on Mount Jolmo Lungma region of Southern Tibet: Scientia Sinica, v. 16, p. 96-111.

Mu, E., and Wu, Y., 1975, Palaeozoic crinoids from the Mount Jolmo Lungma region, 309–313, *In* Report of the Scientific Expedition to the Mount Jolmo Lungma Region (1966-1968), Palaeontology, I: Beijing, Science Press (in Chinese).

Murphy, M.A., and Harrison, T.M., 1999, Relationship between leucogranites and the Qomolangma detachment in the Rongbuk Valley, south Tibet: Geology, v. 27, p. 831-834.

Myrow, P.M., Hughes, N.C., Searle, M.P., Fanning, C.M., Peng, S.C., and Parcha, S.K., 2009., Stratigraphic correlation of Cambrian-Ordovician deposits along the Himalaya: Implications for the age and nature of rocks in the Mount Everest region: Geological Society of America Bulletin, v. 120, p. 323-332.

Nakashima, S., Matayoshi, H., Yuko, T., Michibayashi, K., Masuda, T., Kuroki, N., Yamagishi, H., Ito, Y., and Nakamura, A., 1995, Infrared microspectroscopy analysis of water distribution in deformed and metamorphosed rocks: Tectonophysics, v. 245, p. 263–276.

Nelson, K.D., Zhao, W., Brown, L.D., Kuo, J., and Che, J., 1996, Partially molten middle crust beneath southern Tibet: synthesis of project INDEPTH results: Science, v, 274, p. 1684-1688.

Nesse, W.D., 2011, Introduction to Mineralogy: Oxford University Press, v. 2, 442 p.

Newman, J., The influence of grain size and grain size distribution on methods for estimating paleostresses from twinning in carbonates: Journal of Structural Geology, v. 16.12, p. 1589-1601.

Nicolas, A., and Poirier, J.P., 1976, Crystalline plasticity and solid state flow in metamorphic rocks: Wiley, New York, p. 444.

Odell, N.E., 1967, Highest Fossils in the World: Geological Magazine, v. 104, p. 73-76.

Odell, N.E., 1925, Observations on the rocks and glaciers of Mount Everest: The Geographical Journal, p. 66, v. 289-313.

Ord, A., and Christie, J.M., 1984, Flow stresses from microstructures in mylonitic quartzites of the Moine thrust zone, assynt area, Scottland: Journal of Structural Geology, v. 6, p. 639-655.

Owen, L.A., 2010, Landscape development of the Himalayan-Tibetan orogen: a review: Geological Society, London, Special Publications, v. 338.1, p. 389-407, doi: 10.1144/SP338.18.

Passchier, C.W., and Trouw, R.A.J., 2005, Microtectonics: Springer-Verlag Berlin Heidelberg, 366 p.

Pêcher, A., 1989, The metamorphism in the central Himalaya: Journal of Metamorphic Geology, v. 7, p. 31-41.

Pognante, U., and Benna, P., 1993, Metamorphic zonation, migmatization and leucogranites along the Everest transect of eastern Nepal and Tibet: record of an

exhumation history, *In* Treloar, P.J., and Searle, M.P., (eds) Himalayan Tectonics: Geological Society, London, Special Publication, v. 74, p. 323-340.

Poirier, J.P., and Guillope, M., 1979, Deformation induced recrystallisation of minerals: Bulletin de Mineralogie, v. 102, p. 67-74.

Poirier, J. P., 1985, Creep of crystals: high-temperature deformation processes in metals, ceramics and minerals: Cambridge University Press, Cambridge, 260 p.

Post, A., and Tullis, J., 1998, The rate of water penetration in experimentally deformed quartzite: implications for hydrolytic weakening: Tectonophysics, v. 295 (1/2), p. 117-137.

Post, A., and Tullis, J., 1999, A recrystallized grain size paleopiezometer for experimentally deformed feldspar aggregates: Tectonophysics, v. 303, p. 159-173.

Povondra, P., and Novak, M., 1986, Tourmalines in metamorphosed carbonate rocks from western Moravia, Czechoslovakia: Neues Jahrbuch fuer Mineralogie Monatshefte, v. 1986.6, p. 273-282.

Prior, D.J., Boyle, A.P., Brenker, F., Cheadle, M.C., Day, A., Lopez, G., Peruzzo, L., Potts, G.J., Reddy, S., Spiess, R., Timms, N.E., Trimby, P., Wheeler, J., and Zetterstrom, L., 1999, The application of electron backscatter diffraction and orientation contrast imaging in the SEM to textural problems in rocks: American Mineralogist, V. 84, p. 1741-59.

Radke, B.M., and Mathis, R.L., 1980, On the formation and occurrence of saddle dolomite: Journal of Sedimentary Petrology, v. 50, p. 1149-1168.

Randle, V., 1992, Microtexture determination and its applications: The Institute of Materials, London, 174 p.

Randle, V., and Caul, M., 1996, Representation of electron backscatter diffraction data: Materials Science and Technology, v. 12, p. 844-850.

Raymo, M.E., 1994, The initiation of Northern Hemisphere glaciations: Annual Review of Earth and Planetary Sciences, v. 22, p. 353-383, doi:10.1146/annurev.ea.22.050194.002033.

Reynolds, R.C. Jr, 1965, Geochemical behavior of boron during the metamorphism of carbonate rocks: Geochimica et Cosmochimica Acta, v. 29, p. 1101-1104.

Rosenberg, P.E., and Foit, F.F. Jr, 2006, Magnesiofoitite from the uranium deposits of the Athabasca Basin, Saskatchewan, Canada: Canadian Mineralogist, v. 44, p. 959-965.

Rowe, K.J., and Rutter, E.H., 1990, Paleostress estimation using calcite twinning: experimental calibration and application to nature: Journal of Structural Geology, v. 12, p. 1-17.

Rowley, D.B., 1996, Age of initiation of collision between India and Asia: A review of stratigraphic data: Earth and Planetary Science Letters, v. 109, p. 11-23.

Rowley, D.B., 1998, Minimum age of initiation of collision between India and Asia north of Everest based on the subsidence history of the Zhepure mountain section: Journal of Geology, v. 106, p. 229-235.

Rusk, B.G., Reed, M.H., Dilles, J.H., and Kent, A.J.R., 2006, Intensity of quartz cathodoluminescence and trace-element content in quartz from the porphyry copper deposit at Butte, Montana: American Mineralogist, v. 91, p. 1300-1312.

Rutter, E.H., and Brodie, K.H., 1988, The role of tectonic grain size reduction in the rheologic stratification of the lithosphere: Geologische Rundschau, v. 77, p. 295-308.

Rutter, E.H., Casey, M., and Burlini, L., 1994, Preferred crystallographic orientation development during the plastic and superplastic flow of calcite rocks: Journal of Structural Geology, v. 16, p. 1431-1446.

Rutter, E.H., 1995, Experimental study of the influence of stress, temperature, and strain on the dynamic recrystallization of Carrara marble: Journal of Geophysical Research v. 100, p. 24651-24663.

Sakai, H., 1997, Detachment fault below the summit of Mt. Everest and its tectonic significance in the Himalayan orogeny: Journal of the Geological Society of Japan, v. 103.3, p. 240-252.

Sakai, H., Sawada, M., Takigami, Y., Orihashi, Y., Danhara, T., Iwano, H., Kuwahara, Y., Dong, Q., Cai, H., and Li, J., 2005, Geology of the summit limestone of Mount Qomolangma (Everest) and cooling of the Yellow Band under the Qomolangma detachment: The Island Arc, v. 14, p. 297-310.

Sander, B., 1950, Einführung in die Gefügekunde der geologischen Körper, Band II: Die Korngefüge: Springer-Verlag, Wien Berlin Heidelberg.

Sander, B., 1970, An introduction to the study of fabrics of geological bodies: Pergamon Press, Oxford, 641 p.

Schärer, U., 1984, The effect of initial ^{230}Th disequilibrium on young U-Pb ages: the Makalu case, Himalaya: Earth and Planetary Science Letters, v. 67, p. 191-204.

Schärer, U., Xu, R.H., and Allegre, C.J., 1986, U-Th-Pb systematics and ages of Himalayan leucogranites, south Tibet: Earth and Planetary Science Letters, v. 77 p. 35-48.

Schelling, D., and Arita, K., 1991, Thrust tectonics, crustal shortening, and the structure of the far-eastern Nepal, Himalaya: Tectonics, v. 10, p. 851-862.

Schenk, O., Urai, J.L., Evens, B., 2005, The effect of water on recrystallization behavior and grain boundary morphology in calcite – observations of natural marble mylonites: Journal of Structural Geology, v. 27, p. 1856-1872.

Schmid, S.M., 1994, Textures of geological materials: computer model predictions versus empirical interpretations based on rock deformation experiments and field studies, *In* Bunge, H.J., Siegesmund, S., Skrotzki, W., and Weber, K., (eds) Textures of geological materials: DGM Informationsges, Oberursel, p. 279-301.

Schmid, S.M., Paterson, M.S., and Boland, J.N., 1980, High temperature flow and dynamic recrystallization in Carrara marble: Tectonophysics v. 65, p. 245-280.

Schmid, S.M., 1976, Rheological evidence for changes in the deformation mechanism of Solnhofen limestone toward low stresses: Tectonophysics, v. 31, p. 21-28.

Scoffin, T.P., 1987, Carbonate sediments and rocks: Blackie, Glasgow and London, 274 p.

Searle, M.P.,1986, Structural evolution and sequence of thrusting in the High Himalayan, Tibetan-Tethys and Indus suture zones of Zanskar and Ladakh, western Himalaya: Journal of Structural Geology, v. 8, p. 923-936.

Searle, M.P., Windley, B.F., Coward, M.P., Cooper, D.J.W., Rex, A.J., Rex, D.C., Li Tingdong, Xiao Xuchang, Jan, M.Q., Thakur, V.C., and Kumar, S., 1987, The closing of the Tethys and tectonics of the Himalaya. Geological Society of America Bulletin, v. 98, p. 678-701.

Searle, M.P., Cooper, D.J.W., and Rex, A.J., 1988, Collision tectonics of the Ladakh-Zanskar Himalaya: Royal Society of London Philosophical Transactions, v. A326, p. 117-150.

Searle, M.P., Parrish, R.R., Hodges, K.V., Hurford, A., Ayres, M.W., and Whitehouse, M.J., 1997, Shisha Pangma leucogranite, south Tibetan Himalaya: Field relations, geochemistry, age, origin, and emplacement: Journal of Geology, v. 105, p. 295-317.

Searle, M.P., 1999*a*, Extensional and compressional faults in the Everest-Lhotse massif, Khumbu Himalaya, Nepal: Journal of the Geological Society, London, v. 156, p. 227-240.

Searle, M.P., 1999*b*, Emplacement of Himalayan leucogranites by magma injection along giant sill complexes: Examples from the Cho Oyu, Gyachung Kang and Everest leucogranites (Nepal Himalaya): Journal of Asian Earth Science, v. 17, p. 773-83.

Searle, M.P., Simpson, R.L., Law, R.D., Waters, D.J., and Parrish, R.R., 2002, Quantifying displacement on the South Tibetan detachment normal fault, Everest massif, and the timing of crustal thickening and uplift in the Himalaya and South Tibet: Journal of the Nepal Geological Society, London, v. 160, p. 1-6.

Searle, M.P., Simpson, R.L., Law, R.D., Parrish, R.R., and Waters, D.J., 2003, The structural geometry, metamorphic and magmatic evolution of the Everest massif, High Himalaya of Nepal - South Tibet: Journal of the Geological Society, London, v. 160, p. 345-366.

Searle, M.P., and Godin, L., 2003, The South Tibetan Detachment and the Manaslu leucogranite: A structural reinterpretation and restoration of the Annapurna-Manaslu Himalaya, Nepal: Journal of Geology, v. 111, p. 505-523.

Searle, M.P., Law, R.D., and Jessup, M.J., 2006, Crustal structure, restoration and evolution of the Greater Himalaya in Nepal-South Tibet: implications for channel flow and ductile extrusion of the middle crust, *In* Law, R.D., Searle, M.P., and Godin, L., (eds) Channel Flow, Ductile Extrusion and Exhumation in Continental Collision Zones: Geological Society, London, Special Publication, v. 268, p. 355-378.

Searle, M.P., Stephenson, B., Walker, J., and Walker, C., 2007, Restoration of the western Himalaya: implications for metamorphic protoliths, thrust and normal faulting, and channel flow models: Episodes, v. 30.4, p. 242-257.

Searle, M.P., Law, R.D., Godin, L., Larson, K.P., Streule, M.J., Cottle, J.M., and Jessup, M.J., 2008, Defining the Himalayan Main Central Thrust in Nepal: Journal of the Geological Society of London, v. 165, p. 523-534.

Searle, M.P., Cottle, J.M., Streule, M.J., and Waters, D.J., 2009, Crustal melt granites and migmatites along the Himalaya: melt source, segregation, transport and granite emplacement mechanisms: Earth and Environmental Science Transactions of the Royal Society of Edinburgh, v. 100, p. 219-233. doi:10.1017/S175569100901617X.

Servais, T., Owen, A.W., Harper, D.A.T., Kröger, B., and Munnecke, A., 2010, The Great Ordovician Biodiversification Event (GOBE): the paleoecological dimension.

Shimizu, I., 2008, Theories and applicability of grain size piezometers: the role of dynamic recrystallization mechanisms: Journal of Structural Geology, v. 30, p. 899-917.

Sibley, D.F., and Gregg, J.M., 1987, Classification of dolomite rock textures: Journal of Sedimentary Petrology, v. 57, p. 967-975.

Simpson, R.L., Parrish, R.R., Searle, M.P., and Waters, D.J., 2000, Two episodes of monazite crystallization during metamorphism and crustal melting in the Everest region of the Nepalese Himalaya: Geology, v. 28, p. 403-406.

Slack, J.F., 2002, Tourmaline associations with hydrothermal ore deposits, *In* Grew, E.S., and Anovitz, L.M., (eds) Boron: Mineralogy, Petrology and Geochemistry: Reviews in Mineralogy, v. 33, p. 559-644.

Smith C.S., and Guttman, L., 1953, Measurement of internal boundaries in three-dimensional structures by random sectioning: Trans Am Inst Min Eng J Metals v. 197, p. 81-87.

Spear, F.S., and Wark, D.A., 2009, Cathodoluminescence imaging and titanium thermometry in metamorphic quartz: Journal of Metamorphic Geology, v. 27, p. 187-205, doi:10.1111/j.1525-1314.2009.00813.x.

Stephenson, B.J., Waters, D.J., and Searle, M.P., 2000, Inverted metamorphism and the Main Central Thrust: field relations and thermobarometric constraints from the Kishtwar Window, NW Indian Himalaya: Journal of Metamorphic Geology, v. 18, p. 571-590.

Stephenson, B.J., Searle, M.P., and Waters D.J., 2001, Structure of the Main Central Thrust zone and extrusion of the High Himalayan crustal wedge, Kishtwar–Zanskar Himalaya: Journal of Geological Society, London, v. 158, p. 637-652.

Stipp, M., Stünitz, H., Heilbronner, R., and Schmid, S.M., 2002*a*, The eastern Tonale fault zone: a “natural laboratory” for crystal plastic deformation of quartz over a temperature range from 250 to 700 °C: Journal of Structural Geology, v. 24, p. 1861-1884.

Stipp, M., Stunitz, H., Heilbronner, R., and Schmid, S., 2002*b*, Dynamic recrystallization of quartz: correlation between natural and experimental conditions, *In* De Meer, S., Drury, M.R., De Bresser, J.H.P., and Pennock, G.M., (eds) Deformation

Mechanisms, Rheology and Tectonics: Current Status and Future Perspectives: Geological Society London Special Publications, v. 200, p. 171-190.

Stipp, M., and Tullis, J., 2003, The recrystallized grain size piezometer for quartz: Geophysical Research Letters, v. 30.21, p. 5.

Streule, M.J., Searle, M.P., Waters, D.J., and Horstwood, M.S.A., 2010, Metamorphism, melting, and channel flow in the Greater Himalayan Sequence and Makalu leucogranite: constraints from thermobarometry, metamorphic modeling, and U-Pb geochronology: Tectonics, v. 29, TC5011, doi:10.1029/2009TC002533.

Streule, M.J., Carter, A., Searle, M.P., and Cottle, J.M., 2012, Constraints on brittle field exhumation of the Everest-Makalu section of the Greater Himalayan Sequence: implications for models of crustal flow: Tectonics, v. 31, TC3010, doi:10.1029/2011TC003062.

Thomas, J.B., Watson, E.B., Spear, F.S., Shemella, F.S., Nayak, S.K., and Lanzirotti, A., 2010, TitaniQ under pressure: the effect of pressure and temperature on the solubility of Ti in quartz: Contributions to Mineralogy and Petrology, v. 160, p. 743–759. DOI 10.1007/s00410-010-0505-3.

Torsvik, T.H., Paulson, T.S., Hughes, N.C., Myrow, P.M., and Ganerød, M., 2009, The Tethyan Himalaya: palaeogeographical and tectonic constraints from Ordovician palaeomagnetic data: Journal of the Geological Society, London, v. 166, p. 679-687.

Tullis, J.T., Snoke, A.W., and Todd, V.R., 1982, Significance of petrogenesis of mylonitic rocks: Geology, v. 10, p. 227-230.

Turner, F.J., Griggs, D.T., and Heard, H.C., 1954, Experimental deformation of calcite crystals: Geologic Society of America Bulletin, v. 65, p. 883-934.

Twiss, R.J., 1977, Theory and applicability of a recrystallized grain size piezometer: Pure and Applied Geophysics, v. 115, p. 227-244.

Urai, J., Means, W.D., and Lister, G.S., 1986, Dynamic recrystallization of minerals, *In* Heard, H.C., and Hobbs, B.E., (eds) Mineral and rock deformation: laboratory studies (the Paterson volume): American Geophysical Union Geophysical Monograph, v. 36, p. 161-199.

Urai, J.L., and Jessell, M., 2001, Recrystallization and grain growth in minerals: recent developments, *In* Gottstein, G., and Molodov, D., (eds) Recrystallization and Grain Growth, Proceedings of the First Joint International Conference: Springer Verlag, p. 87- 96.

Valentine, J.W., and Moores, E.M., 1972, Global tectonics and the fossil record: Journal of Geology, v. 80, p. 167-184.

van der Pluijm, B.A., and Marshak, S., 2004, Earth Structure: an introduction to structural geology and tectonics: W.W. Norton and Company inc., v. 2.

van Hinsberg, V.J., Henry, D.J., and Dutrow, B.L., 2011*a*, Tourmaline as a petrologic forensic mineral: A unique recorder of its geologic past: Elements, v. 7, p. 327-332.

van Hinsberg, V.J., Henry, D.J., and Marschall, H.R., 2011*b*, Tourmaline: an ideal indicator of its host environment: Canadian Mineralogist, v. 49, p. 1-16.

Vannay, J .C., and Hodges, K . V., 1996, Tectonomorphic evolution of the Himalayan metamorphic core between the Annapurna and Dhaulagiri, central Nepal: Journal of Metamorphic Geology, v. 14, p. 635-656.

Vernon, R.H., 2004, A practical guide to rock microstrucure: Cambridge University Press, p. 594.

Viskupic, K.., and Hodges, K.V., 2001, Monazite-xenotime thermochronometry: methodology and an example from the Nepalese Himalaya: Contributions to Mineralogy and Petrology, v. 141, p. 233-247.

Viskupic, K., Hodges, K.V. and Bowring, S.A., 2005, Timescales of melt generation and the thermal evolution of the Himalayan metamorphic core, Everest region, eastern Nepal: Contributions to Mineralogy and Petrology, v. 149, p. 1-21.

Visonà, D., and Lombardo B., 2002, Two-mica and tourmaline leucogranites from the Everest–Makalu region (Nepal–Tibet). Himalayan leucogranite genesis by isobaric heating?: Lithos, v. 62, p. 125-150.

Visonà, D., Carosi, R., Montomoli, C., Tiepolo, M., and Peruzzo, L., 2012, Miocene andalusite leucogranite in central-east Himalaya (Everest-Masang Kang area): low-pressure melting during heating: Lithos, v. 144-145, p. 194-208.

Wager, L.R., 1934, A review of the geology and some new observations, *In* Ruttledge, H., (eds) Everest 1933: Hodder & Stoughton, London, p. 312-336.

Wager, L.R., 1939, The Lachi series of northern Sikkim and the age of the rocks forming Mount Everest: Rec. Geologic Survey of India, v. 74.2, p. 171-188.

Wager, L.R., 1965, Injected granite sheets of the Rongbuk valley and the north face of Mt. Everest, *In* Wadia, D.N., commemorative volume: India Mining, Geology and Metallurgy Institute, p. 358-379.

Wang, Z., and Zhen, X., 1975, Imbricate structure in the northern slope of Jolmo Lungma and discussion on the uplift of the Himalaya, *In* Scientific exploration of Jolmo Lungma: Science Publishing House, Beijing, p. 199-221.

Wänke, H., and König, H., 1959, Eine neue Method zur Kalium-Argon-Altersbestimmung and ihre Anwendung auf Steinmeteorite: Z. Naturforsch, v. 14a, p. 860-866.

Wark, D.A., and Watson, E.B., 2006, The TitaniQ: a Titanium-in-Quartz Geothermometer: Contributions to Mineralogy and Petrology, v. 152, p. 743-754, DOI 10.1007/s00410-006-0132-1.

Weaver, C. E., 1959, The clay petrology of sediments, Clays and Clay Minerals, Proceedings of the Sixth National Conference: Pergamon Press, London, p. 154.

Webby, B.D., Droser, M.L., Paris, F., and Percival, I.G., 2004, The Great Ordovician Biodiversification Event: Columbia University Press, New York, p. 484.

Wheeler, J., 1992, Importance of pressure solution and Cobble creep in the deformation of polymineralic rocks: Journal of Geophysical Research, v. 97, p. 4579-86.

Weinberg, R.F., and Searle, M.P., 1999, Volatile-assisted intrusion and autometasomatism of leucogranites in the Khumbu Himalaya, Nepal: Journal of Geology, v. 107, p. 27-48.

Wenk, H.R., Takeshita, T., van Houtte, P., and Wagner, F., 1986, Plastic anisotropy and texture development in calcite polycrystals: Journal of Geophysical Research, v. 91, p. 3861-3869.

White, S.H., Burrows, S.E., Carreras, J., Shaw, N.D., and Humphreys, F.J., 1980, On mylonites in ductile shear zones: Journal of Structural Geology, v. 2, p. 175-187.

Wilkinson, A.J., and Hirsch, P.B., 1997, Electron diffraction based techniques in scanning electron microscopy of bulk materials: Micron, v. 28, p. 279-308.

Winter, J.D., 2001, An introduction to igneous and metamorphic petrology: Prentice-Hall Inc, 697 p.

Wu, C., Nelson, K.D., Wortman, G., Samson, S.D., Yue, Y., Li, J., Kidd, W.S.F., and Edwards, M.A., 1998,Yadong cross structure and the South Tibet detachment in the east central Himalaya: Tectonics, v. 17, p. 28-45.

Yin, A., 2006, Cenezoic tectonic evolution of the Himalayan orogen as constrained by along-strike variation of structural geometry, exhumation history, and foreland sedimentation: Earth Science Reviews, v. 76, p. 1-131.

Yin, C.H., and Kuo, S.T., 1978, Stratigraphy of the Mount Jolmo Lungma and its North slope: Scientia Sinica, v. 21, p. 629-644.

Yin, J.X., 1987, Cambro-Ordovician System, *In* Su, Z.W., (eds) Stratigraphy of the Mount Qomolangma Region: Beijing, Sciences Press, p. 5-26.

Zhao, W., Nelson, K. D., and Team Project INDEPTH, 1993, Deep seismic reflection evidence for continental underthrusting beneath southern Tibet: Nature, v. 366, p. 557–559.

APPENDICES

APPENDIX A

ANALYTICAL CONDITIONS AND INSTRAMENTATION FOR METHODS

Cathodoluminescence: Analytical Conditions

Each of the structural horizons where samples were collected from the Qomolangma Formation has been analyzed using microprobe or ultra-polished thin sections without carbon coating. CL was done using the RELIOTRON 'cold cathode' electron gun and vacuum chamber with a Duniway Stockroom Corp. Terranova 924A thermocouple vacuum gauge controller attached to a Nikon Eclipse 50*i* polarizing microscope. Standard photomicrographs were taken at 10x magnification and under both plane polarized light and CL emission. Operating conditions were typically between 100-120 mTorr and 7-10 kV.

Electron Backscattered Diffraction Analysis (EBSD)

Analytical Conditions

Crystallographic orientation maps were generated using automatically indexed EBSD patterns collected on a Zeiss SUPRA 55VP field emission scanning electron microscope in the Imaging and Chemical Analysis Lab (ICAL) at Montana State University, equipped with HKL-Oxford Nordlys EBSD detector and *Channel 5* acquisition software. Automated maps were collected at 20 kV and 25 kV accelerating voltage for calcite and quartz, respectively, with a beam aperture of 120 µm. The angle between the electron beam and the normal to the sample was 70° at a working distance of 14 mm to 15 mm. Rather than applying a carbon coat, analyses were done in variable pressure mode to avoid charging of the specimen surface. Samples were mapped by moving the electron beam along rectangular rasters at a fixed step size between 2 µm and

5 μm and moving the stage to new positions along a predetermined mosaic grid in between each map; the step size was chosen based on grain and subgrain size and purpose of the analysis. Post processing and display of EBSD data was done using the *Channel 5* suite of programs made by HKL Technology (Oxford Instruments). This software was used to remove misindexed data points, create orientation maps, display orientation data on pole figures, and to create Excel data sheets for grain size analysis.

Sample Preparation

Microprobe polished thin sections were ultra-polished to .05μm at Montana State University. Mechanical polishing was done in three stages on an Allied vibratory polisher: 1) 3 μm diamond suspension polish for twenty minutes; 2) 1 μm diamond suspension polish for twenty minutes; 3) .05 μm colloidal silica suspension polish for eight hours. After each level of polishing, thin sections were put into an ultrasonic cleaner for five minutes to completely remove the polishing solution.

Electron Microprobe Analysis

Analytic Conditions

Electron microprobe analysis was done using a JEOL-JXA 8900 microprobe at Minnesota State University. Operating conditions were 40 degrees takeoff angle, a beam energy of 15 keV, a beam current of 20 nA, and a beam diameter of 5 microns. Elements were acquired using analyzing crystals LiFH for Cr kα, Fe kα, PETJ for Ca kα, K kα, Ti kα, Mn kα, Cl kα, Ba lα, TAP for Si kα, Al kα, Mg kα, Na kα, and LDE1 for F kα. The standards were apatite for F kα, benitoite for Ba lα, chromite for Cr kα, hornblende for Si

kα, Al kα, Ca kα, Mg kα, ilmenite for Ti kα, Fe kα, scapolite for Cl kα, albite for Na kα, Mn-olivine for Mn kα, and microcline for K kα. The peak and background counting time was 20 seconds for Ca kα, Cr kα, Fe kα, K kα, Mg kα, Si kα, Ti kα, Na kα, Mn kα, Al kα, Cl kα, Ba lα, and 40 seconds for F kα. The intensity data was corrected for Time Dependent Intensity (TDI) loss (or gain) using a self-calibrated correction for Na kα, F kα, Cl kα. Unknown and standard intensities were corrected for dead time. Standard intensities were corrected for standard drift over time. Oxygen was calculated by cation stoichiometry and included in the matrix correction. The matrix correction method was ZAF or Phi-Rho-Z Calculations and the mass absorption coefficients dataset was LINEMU Henke (LBL, 1985) < 10KeV / CITZMU > 10KeV. The ZAF or Phi-Rho-Z algorithm utilized was Armstrong-Love/Scott, (1988) (see Armstrong, 1988).

APPENDIX B

ELECTRON MICROPROBE DATA FOR SECONDARY PHASES

Sample EV6b

Electron Microprobe Data: Biotite

Analysis point #	195	196	197	198	199	200	201	202	203	211	212	213
SiO2	35.79	35.13	36.42	35.92	36.63	36.57	37.80	36.20	36.64	36.53	36.78	36.50
TiO2	1.65	1.45	1.70	1.50	1.67	1.82	1.77	1.75	1.74	1.71	1.61	1.49
Al2O3	18.12	18.47	17.99	18.14	17.94	17.95	17.96	17.70	18.08	17.01	17.72	18.14
FeO	17.03	17.63	17.12	16.90	16.95	17.03	16.75	16.51	16.81	17.01	17.14	16.74
MnO	0.00	-0.02	0.02	-0.01	0.05	0.00	0.06	-0.03	0.04	0.02	0.01	0.02
MgO	11.89	12.30	11.80	11.84	12.17	11.91	11.21	11.43	11.83	11.83	11.65	11.72
CaO	0.13	0.12	0.14	0.26	0.39	0.33	0.15	0.17	0.12	0.15	0.17	0.22
Na2O	0.13	0.09	0.06	0.11	0.12	0.15	0.08	0.11	0.13	0.10	0.11	0.05
K2O	8.92	8.14	9.50	9.11	9.05	9.24	9.19	9.20	9.57	9.31	9.52	9.44
Cr2O3	0.05	0.07	0.06	0.04	0.07	0.03	0.13	0.09	0.05	0.05	0.07	0.04
Cl	0.03	0.04	0.03	0.04	0.04	0.01	0.04	0.08	0.03	0.05	0.02	0.04
BaO	0.11	0.14	0.13	0.07	0.00	0.05	0.16	0.07	0.14	0.09	0.14	0.11
F	0.78	0.80	0.83	0.80	0.92	0.88	0.86	0.86	0.83	0.87	0.88	0.87

Analysis point #	214	215	216	217	218	219	220	221	222	223
SiO2	36.06	27.08	36.04	36.60	36.07	36.28	36.93	36.74	36.69	36.27
TiO2	2.12	1.22	1.47	1.71	1.48	1.64	0.61	1.36	1.80	1.79
Al2O3	17.88	13.76	18.69	17.81	18.20	18.01	18.35	18.01	17.95	17.99
FeO	16.92	14.41	17.09	17.41	17.87	17.01	16.43	16.56	16.82	16.66
MnO	0.03	0.03	0.00	-0.02	0.04	-0.02	0.03	-0.03	0.00	0.01
MgO	12.05	9.35	11.85	11.93	12.14	11.76	12.97	12.10	11.83	11.83
CaO	0.18	8.60	0.37	0.17	0.28	0.17	0.09	0.31	0.11	0.06
Na2O	0.09	0.12	0.14	0.16	0.12	0.12	0.09	0.11	0.14	0.11
K2O	8.43	7.17	8.18	9.20	8.39	9.23	9.48	9.53	9.44	9.48
Cr2O3	0.09	0.07	0.12	0.05	0.03	0.04	0.01	0.06	0.02	0.05
Cl	0.07	0.07	0.09	0.04	0.03	0.08	0.06	0.04	0.04	0.01
BaO	0.08	0.05	0.04	0.13	0.12	0.04	0.02	0.01	0.11	0.16
F	0.78	1.00	0.82	0.90	0.88	0.90	1.02	0.98	0.88	0.86

Sample EV6b

Electron Microprobe Data: chlorite

Analysis point #	244	245	246	247	248	249	250	251	252	253	254	255	256	257
SiO2	11.25	25.19	24.93	24.91	25.05	25.29	24.95	25.02	25.09	25.38	25.33	25.00	31.88	24.11
TiO2	0.06	0.06	0.04	0.05	0.08	0.07	0.07	0.01	0.06	0.04	0.06	0.02	0.38	5.49
Al2O3	8.47	21.67	21.79	21.94	21.64	21.93	21.54	21.63	21.41	21.65	22.12	22.37	28.91	20.97
FeO	10.25	21.59	21.77	21.80	21.86	21.68	21.88	21.93	22.16	21.79	22.11	22.07	12.83	20.43
MnO	0.02	0.03	0.02	0.00	0.01	0.01	0.00	0.03	0.01	0.05	0.02	-0.01	-0.01	0.00
MgO	5.90	16.09	16.38	16.39	16.58	16.36	16.55	16.72	16.37	16.53	16.68	16.43	10.28	14.94
CaO	0.00	0.01	0.00	0.02	0.00	0.01	0.02	0.02	0.02	-0.02	0.01	0.02	0.20	0.05
Na2O	0.00	0.02	0.02	0.03	0.03	0.03	-0.01	0.03	0.02	-0.02	0.02	0.06	1.31	0.03
K2O	0.04	0.07	0.07	0.02	0.01	0.20	0.03	0.03	0.03	0.03	0.00	0.02	0.13	0.53
Cr2O3	0.05	0.00	0.01	0.02	0.01	0.00	0.07	0.02	0.00	0.05	0.00	0.04	0.01	0.06
Cl	0.92	0.04	0.02	0.02	0.00	0.03	0.00	0.02	0.01	0.00	0.00	0.01	0.00	0.01
BaO	-0.02	0.02	0.02	0.01	-0.02	0.00	-0.05	0.06	-0.05	-0.01	0.01	-0.02	-0.01	0.04
F	0.30	0.27	0.25	0.30	0.28	0.29	0.29	0.23	0.29	0.28	0.26	0.24	0.29	0.29

Sample EV6b

Electron Microprobe Data: Tourmaline

Analysis point #	54	55	56	57	58	59	60	79	80	81	82	83	84	85
SiO2	31.71	37.09	38.02	36.69	38.14	39.25	38.21	37.62	38.31	38.06	38.57	37.39	38.72	38.78
TiO2	0.65	0.42	0.30	0.49	0.35	0.09	0.71	1.09	0.61	0.94	0.56	0.47	0.35	0.20
Al2O3	25.60	35.61	35.44	32.48	34.23	33.98	34.77	33.72	35.17	34.62	35.06	34.18	35.86	35.98
FeO	4.61	7.22	8.26	7.82	5.61	5.32	6.01	6.72	6.33	6.32	5.70	5.77	6.28	6.22
MnO	0.01	0.02	0.00	0.00	0.00	0.00	0.00	0.00	0.00	0.00	0.02	0.00	0.00	0.00
MgO	6.13	6.94	6.01	7.56	8.53	8.36	7.71	7.80	7.44	7.79	8.14	7.57	7.40	7.33
CaO	5.19	0.44	0.10	2.09	1.21	0.88	0.57	0.82	0.41	0.68	0.68	1.65	0.27	0.22
Na2O	1.64	2.22	2.22	1.47	1.83	2.15	2.27	2.14	2.18	2.22	2.20	2.16	2.16	2.24
K2O	0.15	0.04	0.03	0.03	0.05	0.02	0.06	0.06	0.05	0.04	0.06	0.06	0.06	0.06
Cr2O3	0.01	0.02	0.00	0.02	0.05	0.01	0.02	0.04	0.03	0.04	0.04	0.04	0.19	0.14
Cl	0.14	0.02	0.02	0.07	0.01	0.00	0.00	0.01	0.00	0.00	0.01	0.01	0.00	0.00
BaO	0.00	0.00	0.00	0.00	0.00	0.04	0.01	0.07	0.00	0.06	0.03	0.00	0.00	0.01
F	0.00	0.00	0.00	0.00	0.00	0.00	0.00	0.00	0.00	0.00	0.00	0.00	0.00	0.00

Sample EV6b	48	53
SiO2	36.78	37.01
TiO2	0.40	0.47
Al2O3	34.95	35.15
FeO	6.35	6.45
MnO	0.00	0.02
MgO	7.27	7.35
CaO	0.27	0.33
Na2O	2.21	2.20
K2O	0.05	0.06
Cr2O3	0.04	0.00
Cl	0.00	0.00
BaO	0.05	0.00
F	0.00	0.00

Colors represent data for different grains

Sample EV6b

Electron Microprobe Data: white mica

Analysis point #	236	237	238	239	240	241	242	243	258	259	260	261	262	263
SiO2	44.84	44.97	44.60	44.99	43.82	45.30	45.57	44.81	44.74	47.22	46.93	46.54	45.99	47.31
TiO2	0.56	0.52	0.50	0.42	0.47	0.56	0.61	0.44	0.79	0.33	0.55	0.41	0.63	0.29
Al2O3	31.80	31.77	31.64	32.62	32.02	33.19	32.97	32.72	34.48	32.00	35.35	34.62	34.09	32.79
FeO	2.99	3.42	3.45	3.51	2.96	3.48	3.36	3.49	2.63	2.21	1.59	1.45	2.12	1.79
MnO	0.04	-0.02	-0.01	-0.04	-0.02	-0.01	0.05	-0.01	-0.01	0.00	-0.03	0.01	0.00	0.03
MgO	2.24	2.25	2.18	2.24	2.36	2.41	2.70	2.24	1.96	2.51	1.67	1.61	1.94	2.10
CaO	0.02	0.00	0.01	0.03	0.01	0.00	-0.01	0.01	0.01	0.01	0.01	0.00	0.01	-0.02
Na2O	0.26	0.21	0.25	0.28	0.26	0.28	0.28	0.28	0.35	0.25	0.36	0.33	0.31	0.32
K2O	10.56	10.55	10.68	10.58	10.67	10.43	10.26	10.69	10.07	10.58	10.28	10.76	10.35	10.35
Cr2O3	0.12	0.07	0.03	0.05	0.02	0.01	0.05	0.06	0.06	0.03	0.05	0.06	0.04	0.01
Cl	0.01	0.00	0.00	0.01	0.01	-0.02	0.00	0.00	0.01	0.00	0.01	0.02	0.01	0.01
BaO	0.51	0.50	0.54	0.53	0.44	0.55	0.50	0.39	0.41	0.15	0.40	0.29	0.36	0.18
F	-0.30	-0.26	-0.27	-0.25	-0.23	-0.32	-0.24	-0.25	-0.32	-0.18	-0.29	-0.27	-0.23	-0.27

Analysis point #	264	265	266	267	268	269	270	271
SiO2	45.43	44.98	46.59	44.88	46.46	46.75	46.54	42.63
TiO2	0.51	0.60	0.37	0.45	0.50	0.65	0.41	7.22
Al2O3	30.70	33.32	32.79	33.34	32.91	34.55	33.55	30.32
FeO	3.90	1.84	2.09	2.64	1.89	1.94	1.69	3.80
MnO	0.00	-0.01	-0.01	-0.03	0.02	0.04	-0.03	0.00
MgO	3.43	1.70	2.27	2.79	1.97	2.04	1.88	2.70
CaO	0.00	0.02	-0.02	0.07	0.04	-0.01	0.03	0.10
Na2O	0.30	0.28	0.30	0.51	0.28	0.28	0.31	0.25
K2O	10.45	10.52	10.62	8.74	10.20	10.22	10.48	8.84
Cr2O3	0.06	0.09	0.01	0.07	0.09	0.06	0.09	0.02
Cl	0.01	0.02	-0.01	0.00	-0.01	0.02	0.03	0.04
BaO	0.31	0.36	0.33	0.33	0.36	0.32	0.31	0.31
F	-0.10	-0.30	-0.25	-0.26	-0.24	-0.25	-0.26	-0.21

APPENDIX C

ELECTRON MICROPROBE DATA FOR THE LARGE QUARTZ VEINS IN SAMPLES EV6a AND EV6b

Sample EV6a

Electron Microprobe Data: deformed quartz vein

	Beam curr (nA)	Peak cnt (cps)	Peak Time (s)	Peak (cts)	Ix (c/s/nA)	Pk-Bg (cps)	Pk/Bg	Bg cnt (cps)	Bg1 cnt (cps)	Bg2 cnt (cps)	Weight %	Norm Weight%	Atomic %	Det.Lim ppm	StdDev wt%
	1 / 1 . X = 11148. Y = -36425. Z = 124. BeamX = . BeamY = pre-standard check														
Ti SP4/1	100.421	37.1396	600	22281	0.0036	0.3601	1.0098	36.78	37.981	35.578	0.0001	0.1	0.0001	10	0.0008
Ti SP2/1	100.421	29.8196	600	17890	0.0008	0.0833	1.0028	29.736	30.31	29.163					
Ti SP3/1	100.421	7.2202	600	4332	-0.002	-0.185	0.975	7.4052	7.6335	7.1768					
										Si	46.7	46.7	33.337		
										O	53.2	53.2	66.663		
										Total	99.9002	100	100		
	3 / 1 . X = 6867. Y = -27492. Z = 107. BeamX = . BeamY = . Comment : B-1														
Ti SP4/1	100.726	101.279	600	60747	0.1757	17.699	1.2118	83.58	87.612	79.548	0.0219	0.1	0.0092	15	0.0013
Ti SP2/1	100.726	80.6415	600	48372	0.1385	13.955	1.2093	66.686	68.689	64.684					
Ti SP3/1	100.726	27.5242	600	16513	0.0752	7.5729	1.3796	19.951	20.308	19.595					
										Si	46.7	46.7	33.334		
										O	53.2	53.2	66.657		
										Total	99.9219	100	100	Temp. = 603.3°C	
	4 / 1 . X = 6863. Y = -27514. Z = 111. BeamX = . BeamY = . Comment : B-2														
Ti SP4/1	100.07	90.979	600	54571	0.089	8.9034	1.1085	82.076	85.974	78.177	0.01	0.1	0.0042	15	0.0013
Ti SP2/1	100.07	72.2789	600	43357	0.0548	5.4858	1.0821	66.793	68.792	64.794					
Ti SP3/1	100.07	23.1268	600	13875	0.0344	3.4455	1.1751	19.681	20.008	19.355					
										Si	46.7	46.7	33.336		
										O	53.2	53.2	66.66		
										Total	99.91	100	100	Temp. = 532.4°C	
	5 / 1 . X = 6876. Y = -27526. Z = 111. BeamX = . BeamY = . Comment : B-3														
Ti SP4/1	100.208	89.4998	600	53684	0.0688	6.8972	1.0835	82.603	86.792	78.414	0.0086	0.1	0.0036	15	0.0013
Ti SP2/1	100.208	71.075	600	42635	0.0527	5.2857	1.0803	65.789	68.335	63.243					
Ti SP3/1	100.208	22.4217	600	13452	0.0313	3.1354	1.1626	19.286	19.635	18.938					
										Si	46.7	46.7	33.336		
	Ti-in-quartz geothermometry:									O	53.2	53.2	66.661		
	average calculated temperature = 551.90°C									Total	99.9086	100	100	Temp. = 520°C	

Sample EV6b

Electron Microprobe Data: deformed quartz vein proximal to metasomatic phases

	Beam curr (nA)	Peak cnt (cps)	Peak Time (s)	Peak (cts)	Ix (c/s/nA)	Pk-Bg (cps)	Pk/Bg	Bg cnt (cps)	Bg1 cnt (cps)	Bg2 cnt (cps)	Weight %	Norm Weight	Atomi c%	Det.Li m ppm	StdDev wt%
	1 / 1 . X = -3729. Y = -35865. Z = 135. BeamX = . BeamY = . Comment : pre-check standard														
Ti SP4/1	29.9829	25.149	300	7544	0.0136	0.4067	1.016	24.742	25.629	23.855	0.001	0.1	5E-04	38	0.0032
Ti SP2/1	29.9829	20.125	600	12074	0.0044	0.1334	1.007	19.991	20.578	19.405					
Ti SP3/1	29.9829	6.0435	300	1813	0.0019	0.0567	1.01	5.9868	6.1601	5.8134					
										Si	46.7	46.7	33.34		
										O	53.2	53.2	66.66		
										Total	99.9	100	100		
	6 / 1 . X = -11949. Y = 29295. Z = 119. BeamX = . BeamY = . Comment : D-1														
Ti SP4/1	100.238	103.28	600	61944	0.1776	17.799	1.208	85.476	89.657	81.295	0.023	0.1	0.01	15	0.0014
Ti SP2/1	100.238	82.331	600	49385	0.1426	14.297	1.21	68.034	70.306	65.761					
Ti SP3/1	100.238	28.869	600	17320	0.0827	8.293	1.403	20.576	21.275	19.878					
										Si	46.7	46.7	33.33		
										O	53.2	53.2	66.66	Temp. = 606.8°C	
										Total	99.92	100	100		
	7 / 1 . X = -11875. Y = 29346. Z = 119. BeamX = . BeamY = . Comment : D-2														
Ti SP4/1	100.284	99.174	600	59485	0.1283	12.863	1.149	86.311	89.6	83.023	0.016	0.1	0.007	16	0.0013
Ti SP2/1	100.284	78.847	600	47296	0.0955	9.5747	1.138	69.273	71.897	66.648					
Ti SP3/1	100.284	26.756	600	16052	0.0593	5.9509	1.286	20.805	21.165	20.445					
										Si	46.7	46.7	33.33		
										O	53.2	53.2	66.66	Temp. = 579.2°C	
										Total	99.92	100	100		
	36 / 1 . X = -11979. Y = 29307. Z = 117. BeamX = . BeamY = . Comment : D9														
Ti SP4/1	99.9938	113.45	600	68045	0.2694	26.936	1.311	86.515	90.52	82.509	0.034	0.1	0.014	16	0.0014
Ti SP2/1	99.9938	89.665	600	53783	0.2163	21.633	1.318	68.032	70.29	65.774					
Ti SP3/1	99.9938	32.609	600	19563	0.1221	12.209	1.599	20.4	20.818	19.981					
										Si	46.7	46.7	33.33		
										O	53.2	53.2	66.65	Temp. = 649.5°C	
										Total	99.93	100	100		

Sample EV6b

Electron Microprobe Data: deformed quartz vein proximal to metasomatic phases

Continued

	Beam curr (nA)	Peak cnt (cps)	Peak Time	Peak (cts)	Ix (c/s/nA	Pk-Bg (cps)	Pk/Bg	Bg cnt (cps)	Bg1 cnt (cps)	Bg2 cnt (cps)	Weight %	Norm Weight	Atomi c%	Det.Lim ppm	StdDev wt%
37 / 1 . X = -11965. Y = 29303. Z = 117. BeamX = . BeamY = . Comment : D10															
Ti SP4/1	100.024	104.353	600	62590	0.1893	18.93	1.222	85.419	89.2	81.639	0.0239	0.1	0.01	15	0.0014
Ti SP2/1	100.024	83.2495	600	49936	0.148	14.81	1.216	68.442	70.336	66.548					
Ti SP3/1	100.024	28.8744	600	17323	0.0863	8.633	1.427	20.241	20.721	19.761					
										Si	46.7	46.7	33.33		
										O	53.2	53.2	66.66	Temp. = 612°C	
										Total	99.924	100	100		
38 / 1 . X = -11874. Y = 29334. Z = 122. BeamX = . BeamY = . Comment : D11															
Ti SP4/1	99.8718	109.156	600	65470	0.2286	22.83	1.265	86.323	90.691	81.956	0.0284	0.1	0.012	16	0.0014
Ti SP2/1	99.8718	86.4246	600	51840	0.1787	17.84	1.26	68.582	70.73	66.435					
Ti SP3/1	99.8718	30.1813	600	18107	0.0977	9.762	1.478	20.42	20.498	20.341					
										Si	46.7	46.7	33.33		
										O	53.2	53.2	66.66	Temp. = 629.1°C	
										Total	99.929	100	100		
39 / 1 . X = -11957. Y = 29351. Z = 122. BeamX = . BeamY = . Comment : D12															
Ti SP4/1	99.9938	92.3498	600	55393	0.0693	6.927	1.081	85.423	89.283	81.562	0.0095	0.1	0.004	15	0.0013
Ti SP2/1	99.9938	73.4478	600	44058	0.0631	6.311	1.094	67.137	69.012	65.261					
Ti SP3/1	99.9938	23.5868	600	14151	0.036	3.599	1.18	19.988	20.585	19.391					
										Si	46.7	46.7	33.34		
Ti-in-quartz geothermometry:										O	53.2	53.2	66.66	Temp. = 528.1°C	
average calculated temperature = 599.82°C										Total	99.91	100	100		

Sample EV6b

Electron Microprobe Data: deformed quartz vein distal to metasomatic phases

Analysis point #	Beam curr (nA)	Peak cnt (cps)	Peak Time (s)	Peak (cts)	Ix (c/s/nA)	Pk-Bg (cps)	Pk/Bg	Bg cnt (cps)	Bg1 cnt (cps)	Bg2 cnt (cps)	Weight %	Norm Weight%	Atomic %	Det.Lim ppm	StdDev wt%
1	8 / 1 .	X = -1040.	Y = 28215.	Z = 103.	BeamX = .	BeamY = .	Comment : E-1								
Ti SP4/1	100.253	87.042	600	52210	0.0119	1.1906	1.0139	85.851	89.9567	81.7454	0.0012	0.1	0.0005	15	0.0013
Ti SP2/1	100.253	69.659	600	41786	0.0064	0.6369	1.0092	69.022	70.6998	67.345					
Ti SP3/1	100.253	20.736	600	12441	0.0038	0.3834	1.0188	20.353	21.0548	19.6513					
										Si	46.7	46.7	33.337		
										O	53.2	53.2	66.663	Temp. = 387.7°C	
										Total	99.901	100	100		
10	18 / 1 .	X = 15767.	Y = 33858.	Z = 115.	BeamX = .	BeamY = .	Comment : F-6								
Ti SP4/1	99.6276	85.818	600	51476	0.0102	1.0172	1.012	84.8	88.3724	81.2284	0.0014	0.1	0.0006	15	0.0013
Ti SP2/1	99.6276	68.534	600	41111	0.0139	1.3823	1.0206	67.152	69.4826	64.8205					
Ti SP3/1	99.6276	20.221	600	12132	0.0012	0.1183	1.0059	20.103	20.2847	19.9213					
										Si	46.7	46.7	33.337		
										O	53.2	53.2	66.663	Temp. = 396.4°C	
										Total	99.901	100	100		
11	19 / 1 .	X = 15758.	Y = 33873.	Z = 115.	BeamX = .	BeamY = .	Comment : F-7								
Ti SP4/1	99.5056	84.969	600	50967	0.009	0.8971	1.0107	84.072	87.4286	80.7148	0.0017	0.1	0.0007	15	0.0013
Ti SP2/1	99.5056	68.174	600	40895	0.0137	1.3656	1.0204	66.808	69.4326	64.1836					
Ti SP3/1	99.5056	20.64	600	12383	0.0068	0.6718	1.0336	19.968	20.248	19.688					
										Si	46.7	46.7	33.337		
										O	53.2	53.2	66.663	Temp. = 407.8	
										Total	99.902	100	100		
14	23 / 1 .	X = 14597.	Y = 33346.	Z = 117.	BeamX = .	BeamY = .	Comment : G-1								
Ti SP4/1	99.8718	91.666	600	54983	0.0618	6.1735	1.0722	85.493	89.97	81.015	0.0078	0.1	0.0033	15	0.0013
Ti SP2/1	99.8718	72.739	600	43633	0.0492	4.9156	1.0725	67.824	70.5298	65.1173					
Ti SP3/1	99.8718	23.182	600	13908	0.0275	2.7487	1.1345	20.433	20.9148	19.9513					
										Si	46.7	46.7	33.336		
										O	53.2	53.2	66.661	Temp. = 512.2°C	
										Total	99.908	100	100		
15	24 / 1 .	X = 14572.	Y = 33353.	Z = 117.	BeamX = .	BeamY = .	Comment : G-2								
Ti SP4/1	99.7497	88.814	600	53273	0.0288	2.8699	1.0334	85.944	90.0768	81.8121	0.0033	0.1	0.0014	16	0.0013
Ti SP2/1	99.7497	70.653	600	42382	0.0184	1.8308	1.0266	68.822	70.8266	66.8181					
Ti SP3/1	99.7497	21.923	600	13153	0.0123	1.2252	1.0592	20.698	21.0515	20.3447					
										Si	46.7	46.7	33.337		
										O	53.2	53.2	66.662	Temp. = 449.63°C	
										Total	99.903	100	100		

Sample EV6b

Electron Microprobe Data: deformed quartz vein distal to metasomatic phases

Continued

Analysis point #	Beam curr (nA)	Peak cnt (cps)	Peak Time (s)	Peak (cts)	Ix (c/s/nA)	Pk-Bg (cps)	Pk/Bg	Bg cnt (cps)	Bg1 cnt (cps)	Bg2 cnt (cps)	Weight %	Norm Weight%	Atomic %	Det.Lim ppm	StdDev wt%
16	25 / 1 .	X = 14534.	Y = 33356.	Z = 117.	BeamX = .	BeamY = .	Comment : G-3								
Ti SP4/1	99.7497	85.771	600	51448	0.0176	1.7576	1.0209	84.013	87.6253	80.4013	0.0016	0.1	0.0007	15	0.0013
Ti SP2/1	99.7497	68.772	600	41254	0.0049	0.4919	1.0072	68.28	70.7565	65.8043					
Ti SP3/1	99.7497	20.76	600	12455	0.0057	0.5667	1.0281	20.193	20.9581	19.4279					
										Si	46.7	46.7	33.337		
										O	53.2	53.2	66.663	Temp. = 404.2°C	
										Total	99.902	100	100		
19	29 / 1 .	X = 14510.	Y = 33392.	Z = 117.	BeamX = .	BeamY = .	Comment : G-7								
Ti SP4/1	99.5971	86.842	600	52090	0.0188	1.876	1.0221	84.966	88.9494	80.9816	0.0024	0.1	0.001	16	0.0013
Ti SP2/1	99.5971	69.468	600	41671	0.0145	1.4423	1.0212	68.025	70.7332	65.3174					
Ti SP3/1	99.5971	21.202	600	12720	0.0084	0.8384	1.0412	20.363	20.9214	19.8046					
										Si	46.7	46.7	33.337		
										O	53.2	53.2	66.662	Temp. = 428.9°C	
										Total	99.902	100	100		
20	30 / 1 .	X = -12588.	Y = 28726.	Z = 116.	BeamX = .	BeamY = .	Comment : D3								
Ti SP4/1	99.5971	86.376	600	51811	0.0093	0.9271	1.0109	85.449	89.6065	81.2918	0.0013	0.1	0.0005	16	0.0013
Ti SP2/1	99.5971	69.314	600	41579	0.0083	0.8254	1.0121	68.489	70.7332	66.2445					
Ti SP3/1	99.5971	21.027	600	12615	0.0056	0.5534	1.027	20.473	20.7714	20.1747					
										Si	46.7	46.7	33.337		
										O	53.2	53.2	66.663	Temp. = 392.2°C	
										Total	99.901	100	100		
21	31 / 1 .	X = -12623.	Y = 28736.	Z = 116.	BeamX = .	BeamY = .	Comment : D4								
Ti SP4/1	99.5971	85.723	600	51419	0.0065	0.652	1.0077	85.071	89.4998	80.6415	0.0017	0.1	0.0007	15	0.0013
Ti SP2/1	99.5971	69.538	600	41713	0.0154	1.534	1.0226	68.004	69.8728	66.1344					
Ti SP3/1	99.5971	20.927	600	12555	0.0075	0.7518	1.0373	20.175	20.6314	19.718					
										Si	46.7	46.7	33.337		
										O	53.2	53.2	66.663	Temp. = 407.8°C	
										Total	99.902	100	100		
22	32 / 1 .	X = -12653.	Y = 28751.	Z = 116.	BeamX = .	BeamY = .	Comment : D5								
Ti SP4/1	99.9023	87.489	600	52478	0.0158	1.5758	1.0183	85.913	90.0734	81.7521	0.0018	0.1	0.0008	16	0.0013
Ti SP2/1	99.9023	69.518	600	41701	0.0084	0.837	1.0122	68.681	71.4268	65.9343					
Ti SP3/1	99.9023	21.16	600	12695	0.0081	0.8118	1.0399	20.348	20.7848	19.9113					
										Si	46.7	46.7	33.337		
										O	53.2	53.2	66.663	Temp. = 411.2°C	
										Total	99.902	100	100		

Sample EV6b

Electron Microprobe Data: deformed quartz vein distal to metasomatic phases

Continued

Analysis point #	Beam curr (nA)	Peak cnt (cps)	Peak Time (s)	Peak (cts)	Ix (c/s/nA)	Pk-Bg (cps)	Pk/Bg	Bg cnt (cps)	Bg1 cnt (cps)	Bg2 cnt (cps)	Weight %	Norm Weight%	Atomic %	Det.Lim ppm	StdDev wt%
23	33 / 1 .	X = -12707.	Y = 28731.	Z = 116.	BeamX = .	BeamY = .	Comment : D6								
Ti SP4/1	100.0244	87.612	600	52552	0.022	2.2012	1.0258	85.411	89.4064	81.4152	0.0021	0.1	0.0009	16	0.0013
Ti SP2/1	100.0244	69.9945	600	41987	0.0075	0.7487	1.0108	69.246	71.5336	66.9581					
Ti SP3/1	100.0244	21.4465	600	12867	0.0073	0.7301	1.0352	20.716	21.0315	20.4014					
										Si	46.7	46.7	33.3367		
		Ti-in-quartz geothermometry:								O	53.2	53.2	66.6624	Temp. = 420.6°C	
		average calculated temperature = 419.88°C								Total	99.9021	100	100		